ELECTROKINETIC AND BUOYANCY EFFECTS IN COLLOIDAL SUSPENSIONS

by

Brett Matthew Belongia

A Dissertation Submitted to the Faculty of the

DEPARTMENT OF CHEMICAL AND ENVIRONMENTAL ENGINEERING

In Partial Fulfillment of the Requirements
For the Degree of

DOCTOR OF PHILOSOPHY
WITH A MAJOR IN CHEMICAL ENGINEERING

In the Graduate College

THE UNIVERSITY OF ARIZONA

1999

INFORMATION TO USERS

ELECTROKINETIC AND BUOYANCY EFFECTS IN COLLOIDAL SUSPENSIONS

by

Brett Matthew Belongia

A Dissertation Submitted to the Faculty of the

DEPARTMENT OF CHEMICAL AND ENVIRONMENTAL ENGINEERING

In Partial Fulfillment of the Requirements
For the Degree of

DOCTOR OF PHILOSOPHY
WITH A MAJOR IN CHEMICAL ENGINEERING

In the Graduate College

THE UNIVERSITY OF ARIZONA

1 9 9 9

THE UNIVERSITY OF ARIZONA ®
GRADUATE COLLEGE

As members of the Final Examination Committee, we certify that we have

read the dissertation prepared by Brett Matthew Belongia

entitled Electrokinetic and Buoyancy Effects in Colloidal Suspensions

and recommend that it be accepted as fulfilling the dissertation

requirement for the Degree of Doctor of Philosophy

James C. Baygents   3 Dec 99
_____   _____
James C. Baygents   Date

Farhang Shadman   7/2/99
_____   _____
Farhang Shadman   Date

Srini Raghavan   7/2/99
_____   _____
Srini Raghavan   Date

_____   _____
                                      Date

_____   _____
                                      Date

Final approval and acceptance of this dissertation is contingent upon
the candidate's submission of the final copy of the dissertation to the
Graduate College.

I hereby certify that I have read this dissertation prepared under my
direction and recommend that it be accepted as fulfilling the dissertation
requirement.

James C. Baygents   3 Dec 99
_____   _____
Dissertation Director   Date

STATEMENT BY AUTHOR

This dissertation has been submitted in partial fulfillment of requirements for an advanced degree at The University of Arizona and is deposited in the University Library to be made available to borrowers under rules of the Library.

Brief quotations from this dissertation are allowable without special permission, provided that accurate acknowledgment of source is made. Requests for permission for extended quotation from or reproduction of this manuscript in whole or in part may be granted by the copyright holder.

SIGNED:

ACKNOWLEDGEMENTS

DEDICATION

This dissertation is dedicated to my loving wife whose support and patience has made it possible.

TABLE OF CONTENTS

TABLE OF CONTENTS (con't)

LIST OF FIGURES

LIST OF FIGURES–Continued

LIST OF TABLES

ABSTRACT

Dewatering of silica and alumina suspensions was accomplished using electrodecantation and electrocoagulation. Electrocoagulation was found to occur in high conductivity alumina suspensions (250-1300 μS/cm), while electrodecantation was found to be the separation mechanism in low conductivity suspensions of alumina and silica (< 20 μS/cm). With these low conductivity suspensions, a clear fluid layer developed on the surface of the suspension. A clear fluid layer did not develop in high conductivity silica suspensions, 250 μS/cm, even though electrodecantation was found to dominate the separation. Spatial variations in the pH and conductivity were measured at the completion of electrodecantation experiments.

A boundary-layer model was developed to quantitatively establish the principles of electrodecantation. This model provides an explanation for the formation of the clear fluid layer on the surface of colloidally stable suspensions and provides an understanding of how buoyancy driven motion redistributes ions produced/consumed at the electrodes, which results in the formation of pH and conductivity gradients. The growth rate of the clear layer at the top of the chamber is initially slower than that predicted by the model; at later stages the theory and experiments are in agreement.

Numerical simulations were performed to support the boundary-layer model and were used to incorporate important features such as electrode reactions, ion gradients, and cell geometry omitted from the model. Two-dimensional simulations were performed to study the effects of buoyancy driven motion in the absence of any ion gradients. Due to

limited computer resources, one-dimensional simulations were used to show that a clear fluid layer would not necessarily be expected in high conductivity suspensions and to study the effects of electrode reactions in the absence of any fluid motion.

To characterize properties important to electrodecantation, two techniques were developed to measure particle diffusion coefficients, size, and electrophoretic mobility. Taylor-Aris dispersion measurements are shown to provide accurate diffusion coefficient measurements for colloidal particles up to about 0.3 μm in diameter and capillary electrophoresis is used to establish a novel method for measuring electrophoretic mobilities of colloids that compares favorably with existing methods.

1.0 INTRODUCTION

1.1 Scope

Chemical mechanical planarization (CMP) has emerged as a preferred planarization technology in the manufacture of multilevel integrated circuits for both dielectric and metal films. Polishing of dielectric layers such as SiO_2 typically involves use of a highly alkaline (pH $\approx$ 11), silica-based slurry, whereas acidic (pH $\approx$ 4), alumina-based slurries are used for planarizing metal films such as W, Al, and Cu. The alumina or silica particles in the slurry are sub-micron in size and hence may be considered to be in the colloidal regime. Along with slurry, a large amount of ultra pure water (see below) is consumed during CMP. For each liter of slurry applied to the CMP tool, between 20 and 120 liters of water will be used in the CMP process. This accounts for more than 25% of the total water usage associated with wafer processing. As the implementation of CMP increases, it is predicted that slurry use will increase by 21% per year through the year 2010. Consequently, by the turn of the century, the amount of water used during CMP is expected to grow to between 30 and 40% of the total wafer processing water (Corlett, 1998).

High-purity water, known as ultra pure water (UPW), is used during CMP to minimize defects during wafer manufacturing. These imperfections may occur if impurities present in the rinse water deposit on the wafer surface or if the wafer surface is not thoroughly cleaned after polishing. To decrease the probability of defects, water is sent through a water purification loop. Ultra-purification systems vary by organization but all processes involve three crucial treatment strategies: filtration, ion exchange, and

the application of ultraviolet light (Tolliver, 1988). Throughout the purification process, reverse osmosis and ultrafiltration are used to achieve solids concentrations on the order of 1 ppb. The particle-depleted water is sent through an ion exchange column to remove ionic impurities, e.g. dissolved silica or metal ions, and is treated with UV light of varying wavelengths to break down organic and biological impurities. A more complete description of the UPW system, and each stage involved in the processing of UPW, is provided by Chen in his Ph.D. dissertation (1997).

The combination of ultra pure water and spent slurry constitute the major waste stream generated by CMP (see Figure 1.1). The solids discharged in this waste stream form a stable suspension containing between 0.03 and 1.0 wt% solids (Corlett, 1998, Mendicino & Brown, 1998). As the demand for CMP grows, the need to develop new and efficient recycle strategies is becoming increasingly important. The introduction of recycle strategies will reduce the cost associated with slurry use, waste disposal, and the production and consumption of ultra pure water. In addition, many industries are finding it harder to comply with local environmental regulations for discharging suspended solids. Typical limitations on the total suspended solids discharged range from 0.02 to 200 mg/L (Corlett, 1998). The introduction of effective treatment and recycle strategies can aid in achieving acceptable disposal limits.

To avoid excessive fouling of the filtration membranes of an UPW process, solids must be removed from recycled waste streams prior to their return to the UPW system. The research presented here aims to study alternative solid/liquid separation techniques that will allow for recycling of water while avoiding the disadvantages of current

NEW SLURRY

RINSE
WATER

WATER TO
PURIFICATION
LOOP

SLURRY

POLISHING
TOOL

WATER

USED
SLURRY

SEPARATION PROCESS

SOLIDS

WASTE
SOLIDS
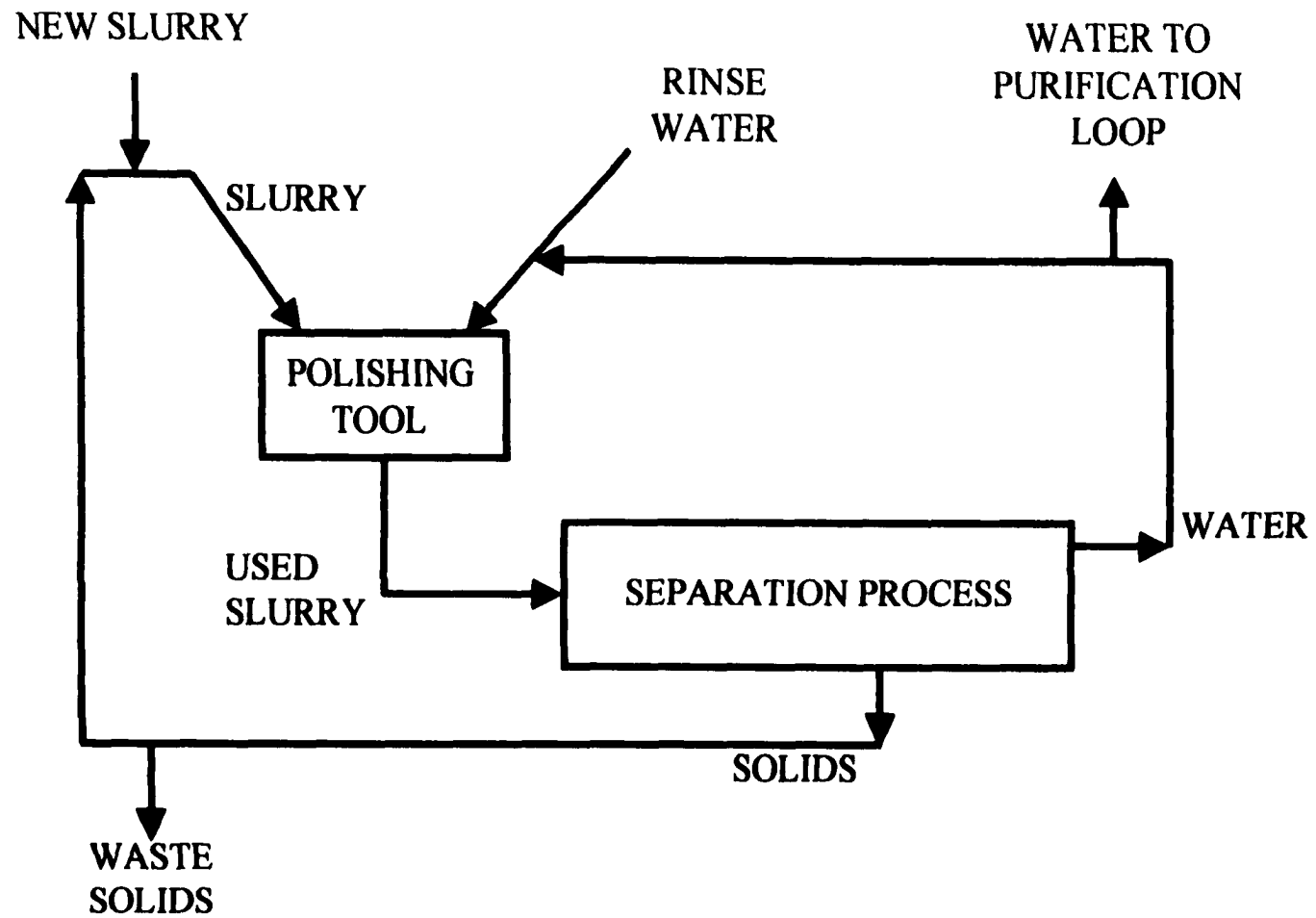
Figure 1.1: A Possible CMP Process

treatment strategies (see below). In addition to recycling of water, there is some interest in recovering the used solids. Concern over an inability to hold slurry makers accountable for variations and impurities in slurry composition has prevented the reuse of slurries by the semiconductor industry. However, applications beyond the semiconductor industry, such as in disk drive or optics manufacturing, which require less stringent controls on particle size, are growing (Corlett, 1998). Solids may be reused as fillers in asphalt or concrete, reclaimed silica particles may be used in foundries for forming molds, and in the case of some new slurries, titanium dioxide particles may be reused in paint pigments (Corlett, 1998).

Traditionally, waste streams containing larger colloidal particles have been sent to holding tanks and the particles allowed to sediment under the effects of gravity. However, for suspensions that contain sub-micron particles, such as CMP waste streams, sedimentation without chemical assistance requires a prohibitively long time. The Stokes settling velocity of a particle is given by

$$U_{\text{Stokes}} = \frac{2}{9}\frac{a_p^2}{v_f}\left(\frac{\rho_p}{\rho_f}-1\right)g\,,$$

(1.1)

where a_p is the particle radius, v_f is the kinematic viscosity of the fluid, g is the acceleration due to gravity, and ρ_p and ρ_f are the density of the particle and fluid, respectively. A silica particle of radius 100 nm and density $2.96\,\text{g/cm}^3$ has a Stokes settling velocity of 4.3×10^{-6} cm/s in water and would require approximately 65 hours to settle 1 cm. Consequently other methods are used to efficiently treat large volumes of waste containing sub-micron particulates.

Currently, two techniques, filtration and chemical flocculation, are predominantly employed to remove solids from suspension. Filtration is usually performed with a crossflow ultrafiltration apparatus. The crossflow filtration process will remove particles from CMP waste streams until the solids content in the retentate approaches 1 to 10 wt%. At this point, permeation rates diminish and further water recovery requires a different treatment strategy. For example, the retentate may be sent to a filter press where the remaining water is removed and a solid cake of particles is formed.

Chemical flocculation consists of continuously adding chemicals, i.e. coagulating agents or flocculants, to aid in the sedimentation of suspended solids. Coagulating agents are usually polyvalent electrolytes such as calcium, aluminum and iron salts, which reduce electrostatic interparticle repulsion and, so, allow van der Waals attractions to drive particles into agglomerates. Flocculants are typically high molecular weight polymers that adsorb onto particles and bind the solids together by the formation of interparticulate bridges. In both cases, aggregates result, which then settle under the action of gravity. The major drawback to this approach is that the addition of flocculants or coagulating agents can be costly when large amounts of waste are involved. Furthermore, these chemicals may cause environmental problems of their own.

The focus of the research described here is to investigate alternatives to chemical conditioning that rely on the effects of electric fields to de-water colloidal suspensions. Two electrical separation techniques were studied, viz. electrodecantation and electrocoagulation. Both of these separation processes have the advantage of not requiring flocculating or coagulating agents, and both methods can concentrate CMP

waste streams to higher solids content than those realized in crossflow filtration. Additionally, electrodecantation collects the solids without altering the size of the particles, which is desirable if the solids are to be recycled and reused. These electrochemical processes represent an alternative approach to chemical conditioning for solid-liquid separation in colloidal suspensions, and have been previously used for the separation and purification of organic and inorganic colloidal matter on both industrial and laboratory scales.

1.2 Disclaimer

The following literature review is not intended to be all-inclusive, rather it should provide the reader with an overview of the material central to my research.

1.3 Electrocoagulation

Electrocoagulation has been studied as a means of treating waste waters containing food and protein (Beck, et al., 1974), oil (Biswas & Lazarescu, 1991), dyes (Do & Chen, 1994), and various suspended particulates including clays and silica (Donnin, et al., 1994, Szynkarczuk, et al., 1994, Matteson, et al., 1995, Renk, 1988). The mechanism is believed to involve the *in-situ* generation of ions by the dissolution of the electrodes. Consumable metal electrodes, such as iron or aluminum, are used to continuously produce metal ions in the vicinity of the anode. Electrophoretic motion simultaneously concentrates negatively-charged particles in the region of the anode. The released ions neutralize the charge of the particles thereby facilitating coagulation (Vik,

et al., 1984, Dalrymple, 1994). Inert electrodes, such as titanium (Dalrymple, 1994), and the passage of an alternating current (Parekh, et al., 1990) have also been observed to remove metal ions from solution, and to initiate the coagulation of suspended solids.

During electrocoagulation, an electric field is applied to the suspension, which is subsequently transferred to a separation stage, where settling occurs. Investigators have observed that, once flocculation has begun, gravitational sedimentation adequately drives the separation process. Thus the electric field can be removed to reduce the amount of power consumed in an electrocoagulation process (Sauer & Davis, 1994, Shang, & Lo, 1997). The efficiency of electrocoagulation may also be improved by gentle agitation during the electrochemical treatment, e.g. by stirring or bubbling gas (Beck, et al., 1974, Do & Chen, 1994). In the latter case, a combination of electrocoagulation and flotation has been found to be an effective treatment of urban wastewater (Beck, et al., 1974, Pouet & Grasmick, 1995). When used in conjunction with filtration, electrocoagulation can extend the life of ultrafiltration membranes (Pouet, et al., 1992, Pouet & Grasmick, 1994).

1.4 Electrodecantation

Electrodecantation, by contrast, is a technique that has drawn limited interest in recent years. A complete historical perspective of the subject can be found in various review articles (Stamberger, 1946, Svensson, 1948, Bier, 1959). The phenomenon was first observed by Pauli (1924) who noted that the passage of a direct electrical current through a suspension of charged colloids resulted in the development of two distinct

strata, or layers, with the bottom layer containing most of the colloidal material. A mechanism for this stratification process was first proposed by Blank and Valko (1928), and then verified by Verwey and Kruyt (1933).

Blank and Valko postulated that electrodecantation results from the charged particles migrating electrophoretically towards the electrode of opposite charge. The accumulation of particles around that electrode increases the density locally and thus the particle-enriched suspension sinks to the bottom of the vessel. At the opposite electrode, a colloid-depleted region develops and rises. The stratification, or decantation, process is stabilized against mixing by the resultant vertical density gradients.

Electrodecantation has been applied to the separation of gold sols (Pauli, et al., 1939), proteins (Kirkwood, 1941, Gutfreund, 1943, Nielsen & Kirkwood, 1946, Cann, et al., 1949, Cann, et al., 1949, Bier, et al., 1953), and viruses (Largier, 1956 & 1957). Variations have been exploited to facilitate the separation of a variety of colloidal matter. For example, particles with a specific gravity less than the surrounding medium tend to accumulate at the top of the vessel, and rubber latex has been collected as a cream in this way (Murphy, 1942 & 1943). The passage of an electric current has no effect on uncharged material; this allows the separation of mobile particles from those at their isolectric point (Gutfreund, 1943). Multiple membrane devices (Largier, 1957, Polson, 1953) and semi-continuous/continuous flow designs (Murphy, 1943, Pauli, 1942) have also been developed. Many of these approaches have been adapted to industrial scale applications.

Despite the many variations and applications described above, a quantitative understanding of the principles of electrodecantation is all but non-existent. In 1946, Nielsen and Kirkwood published experimental data for the fractionation of protein mixtures by electrodecantation. These experiments were performed in an apparatus they termed an electrophoresis-convection channel. A relationship describing the influence of the electric field, column length, time, and protein mobilities was presented (Nielsen & Kirkwood, 1946). A few years later, Kirkwood, et al., (1950) presented a theory for the time dependent transport of species based on experiments performed in an electrophoresis-convection channel. This theory was developed for certain limiting and ideal conditions. These include the assumptions that Joule heating is negligible, the flow through the electrophoresis-convection channel is laminar, and that the electric field is uniform in the horizontal plane. The theory is also based on the limiting condition that

$$\mathbf{Pe}_\epsilon \equiv \frac{M_E E b}{D} \ll 1 \tag{1.2}$$

where: $\mathbf{Pe}_\epsilon$ is an electric Peclet number weighing the relative importance of electrophoresis and diffusion; M_E is the electrophoretic mobility of the suspended particles; E is the electric field strength; b is the separation channel width; and D is the diffusion coefficient of the particles. The requirement that the electrophoretic Peclet number be small is rarely satisfied under practical operating conditions. For instance, typical values of $M_E = 10^{-4}\,\mathrm{cm^2/V \cdot s}$, $D = 10^{-6}\,\mathrm{cm^2/s}$, and $b = 1\,\mathrm{cm}$ would necessitate that $E \ll 10^{-2}\,\mathrm{V/cm}$ to ensure $\mathbf{Pe}_\epsilon \ll 1$. Nevertheless, this theory provided an order of

magnitude approximation to the time of transport and separation factors observed in experiments performed in Kirkwood's electrophoresis-convection channel.

1.5 Clarification of Other Colloidal Suspensions

The work presented here is focused on treatment of CMP waste streams, but the techniques developed lend themselves to treating many colloidal suspensions. For example, coal-fired power plants produce colloidally-contaminated aqueous suspensions of coal and clay. These stable suspensions are usually treated with chemicals, i.e. chemical flocculation, to increase the sedimentation to an acceptable rate. Electrokinetic separation strategies can eliminate the need for chemical addition (see above). Other possible applications for electrokinetic separation processes include the removal of mill tailings from waste streams (Sprute & Kelsh, 1982), dewatering of phosphate clay (Shang & Lo, 1997), the concentration and purification of proteins, and the removal of impurities from non-aqueous suspensions. Previous studies on non-aqueous suspensions have included removing illite particles from toluene (Shih, et al. 1986), sedimentation of α-alumina particles from xylene (Lee, et al., 1979), and separating oxidized aluminum and iron particles from kerosene (Matsumoto, et al., 1981). Most of these studies have been focused on feasibility rather than the advancement of the understanding of the underlying fundamental phenomena (Sauer & Davis, 1994, Johnson & Davis, 1999). The dissertation to be presented illustrates fundamental processes important to effectively applying electrokinetic separations techniques and quantitatively describes phenomena relevant to electrically-driven solid/liquid separations processes.

1.6 Explanation of Dissertation Format

The majority of the research presented here is furnished in the form of published or publishable manuscripts that have been appended at the end of the dissertation (see Appendix A-D). *Except where noted*, the work (experiments and analysis) contained within these manuscripts was performed by myself. The intent of this section is to explain the relationship between the appendices and how they fit in the overall layout of this dissertation.

Appendix A has been accepted for publication in the *Journal of the Electrochemical Society* and was written primarily by myself under the guidance of my advisors (Assoc. Prof. James C. Baygents & Prof. Srini Raghavan). This manuscript contains the initial studies on the application of an electric field to stable colloidal suspensions. Two separation mechanisms, electrodecantation and electrocoagulation, were observed, and the conditions under which each mechanism dominates were studied. Dr. Phillip D. Haworth, carried out the initial screening studies on electrodecantation and generated the results presented in figures 3a, 3b, 5, 6, and 7 of this appendix.

A model describing the buoyancy-driven flow in electrodecantation is presented in Appendix B (primarily authored by Assoc. Prof. Baygents, Prof. Raghavan, Prof. Lee R. White, of Carnegie–Mellon University, and myself). This model is not limited to the low Peclet number regime, in contrast to the theory presented by Kirkwood (see above). After an initial lag time, the predictions of the model match the experimental results.

Appendix B has been submitted for publication to *Industrial & Engineering Chemistry Research*.

For completeness, Appendix C (published in the *Journal of Colloid and Interface Science*) and D (published in *Applied and Environmental Microbiology*) have been included to illustrate techniques for characterizing particle properties that are important to the electrokinetic separations processes described above. The third manuscript (Appendix C), co-authored by Assoc. Prof. Baygents and myself, presents a method for measuring the diffusion coefficients of colloidal particles. The diffusion coefficients determined using this technique are in good agreement with those measured by photon correlation spectroscopy and results calculated from a model set forth by Silebi and DosRamos (1989).

The primary authors of Appendix D, Dr. John R. Glynn, Jr., Prof. Robert G. Arnold, and Assoc. Prof. Baygents, describe a novel method for measuring electrophoretic mobility of colloidal particulates, which compares favorably to existing methods. Working in parallel, Dr. Glynn and I developed the capillary electrophoresis protocol for measuring the electrophoretic mobility of colloidal-sized particles. Dr. Glynn provided the data published in this manuscript, but I performed much of the initial work on the protocol.

The remaining chapters contain a survey of the entire dissertation. A summary of the important results and conclusions of the appended manuscripts are presented in chapter 2.0 PRESENT STUDY. In addition, chapter 2.0 contains a numerical approach to solving the equations put forth in Appendix B. Under the direction of Assoc. Prof.

Baygents, Mr. Thomas L. Sounart and I developed one and two-dimensional time dependent numerical simulations to elucidate the principles of electrodecantation. One-dimensional simulations were performed to investigate the effects of ion gradients on the distribution of suspended solids when fluid motion is not present. In addition, two-dimensional simulations were developed to account for fluid motion and a two-dimensional electric field in the absence of ion gradients. The simulation results are used to further explore the differences observed between experimental results and results predicted by the boundary-layer model of electrodecantation (Appendix B). Finally, chapter 3.0 FUTURE STUDIES will describe possible implications of the research for future studies.

2.0 PRESENT STUDY

2.1 Overview

The material in chapter 2 is intended to summarize the important methods, results, and conclusions presented in the papers appended to this dissertation. In addition, numerical simulations of electrodecantation are included in this chapter; these studies are in support of the analytical boundary-layer model described in Appendix B. The chapter is organized such that experiments on electrodecantation and electrocoagulation are summarized first (i.e. the material from Appendices A and B). Next, a model for electrodecantation describing the balance laws, boundary-layer scaling, and the primary implications of the analysis is presented. Two-dimensional simulations are then provided to verify the boundary-layer scaling and to study the effects of chamber geometry on electrodecantation. Subsequently, one-dimensional simulations are developed to study the effects of electrode reactions, pH gradients, and conductivity gradients in the absence of fluid motion. Finally, experiments on particle characterization (cf. Appendices C and D) are summarized. A nomenclature section is included at the end of this chapter to assist the reader.

2.2 Experiments on Electrodecantation and Electrocoagulation

2.2.1 Methods

Stable suspensions of colloidal silica and alumina were prepared as described in Appendix A and B and placed into a Plexiglas chamber (Figure 2.1). Two vertically oriented electrodes were submerged into the suspension and an electric field between 0.4
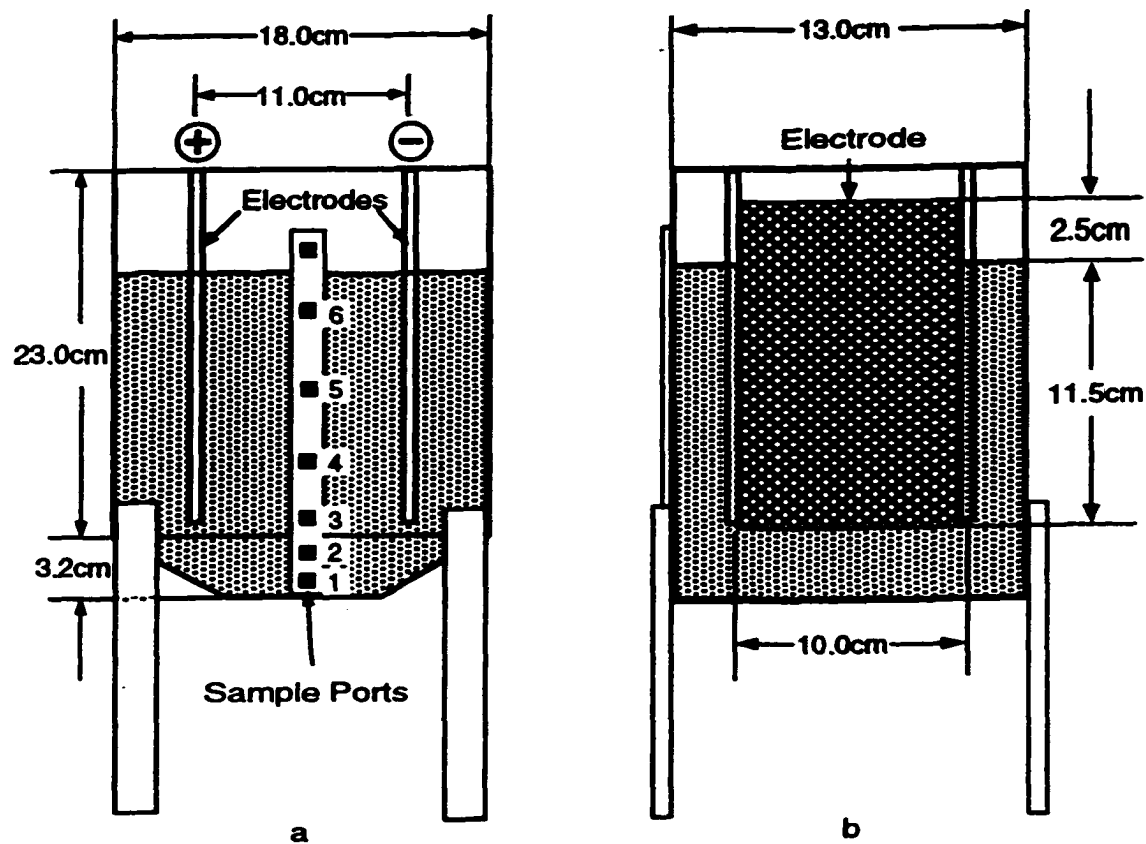
Figure 2.I Electrodecantation chamber. a. front view. b. righthand side view.

and 10.0 V/cm applied. To suppress accumulation of particles on the electrodes, a manual switching device was used to periodically reverse the polarity of the electric field with a frequency between 0 and 0.5 min^{-1}. During the experiments, suspensions were visually monitored for the formation of a clear fluid layer and, when such a layer developed, the height of this clear layer recorded as a function of time (see Figure 2.8, page 45). At the completion of the experiments, the conductivity, pH, and turbidity were measured from samples taken at six different depths, and on the bottom of the container. To determine if the particles concentrated on the bottom of the chamber were altered during the experiments, particle size and electrophoretic mobility measurements were performed before and after treatment.

2.2.2 Results

Large aggregates were visually observed to form and settle when an electric field was applied to high-conductivity (100 to $1350 \mu S/cm$) alumina suspensions. This electrically-assisted separation technique has been known historically as electrocoagulation and was found to be the dominant separation mechanism in high ionic strength alumina suspensions. These observations indicate that the applied electric field either induced or accelerated coagulation processes within the suspension, since the native suspensions were stable for at least 24 hours. Particle size measurements, performed before and after application of the field, confirmed that coagulation had occurred. Figures 2.2 and 2.3 show the removal of alumina particles as a function of time; samples were taken during the experiments, which were done for two different
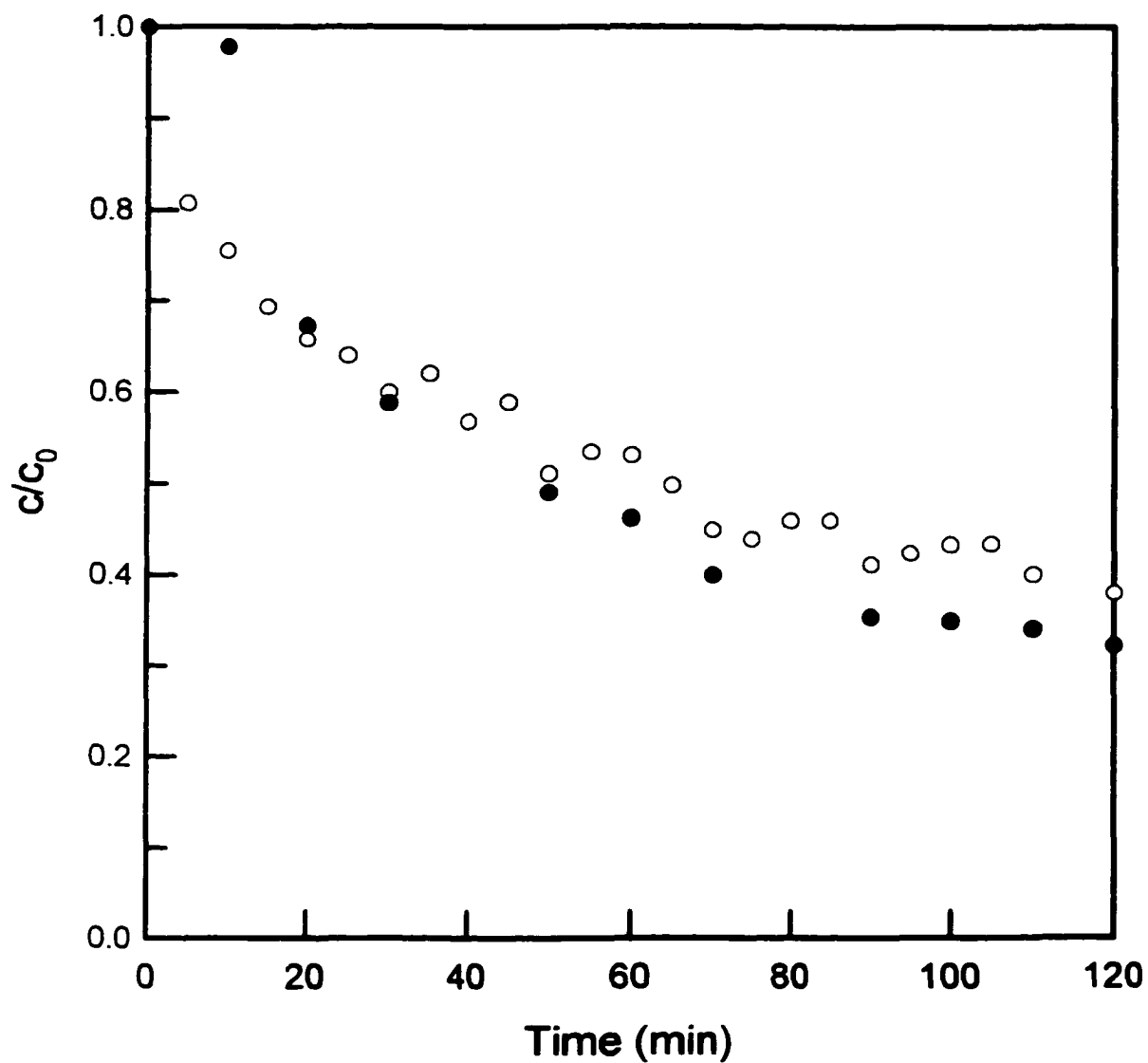
Figure 2.2: Normalized concentration of alumina 2.5 cm below the surface for high-conductivity suspensions. (Legend: o, 203 nm alumina and 1mM KNO_3, $c_0 \approx 0.40$ w/v%, $\sigma \approx 150$ $\mu S/cm$, pH ≈ 5.2, E = 7.3 V/cm, polarity switched every 2 minutes; $\bullet$, 203 nm alumina and 10 mM KNO_3, $c_0 \approx 0.40$ w/v%, $\sigma \approx 1350$ $\mu S/cm$, pH ≈ 5.7, E = 3.6 V/cm, polarity switched every 2 minutes.)
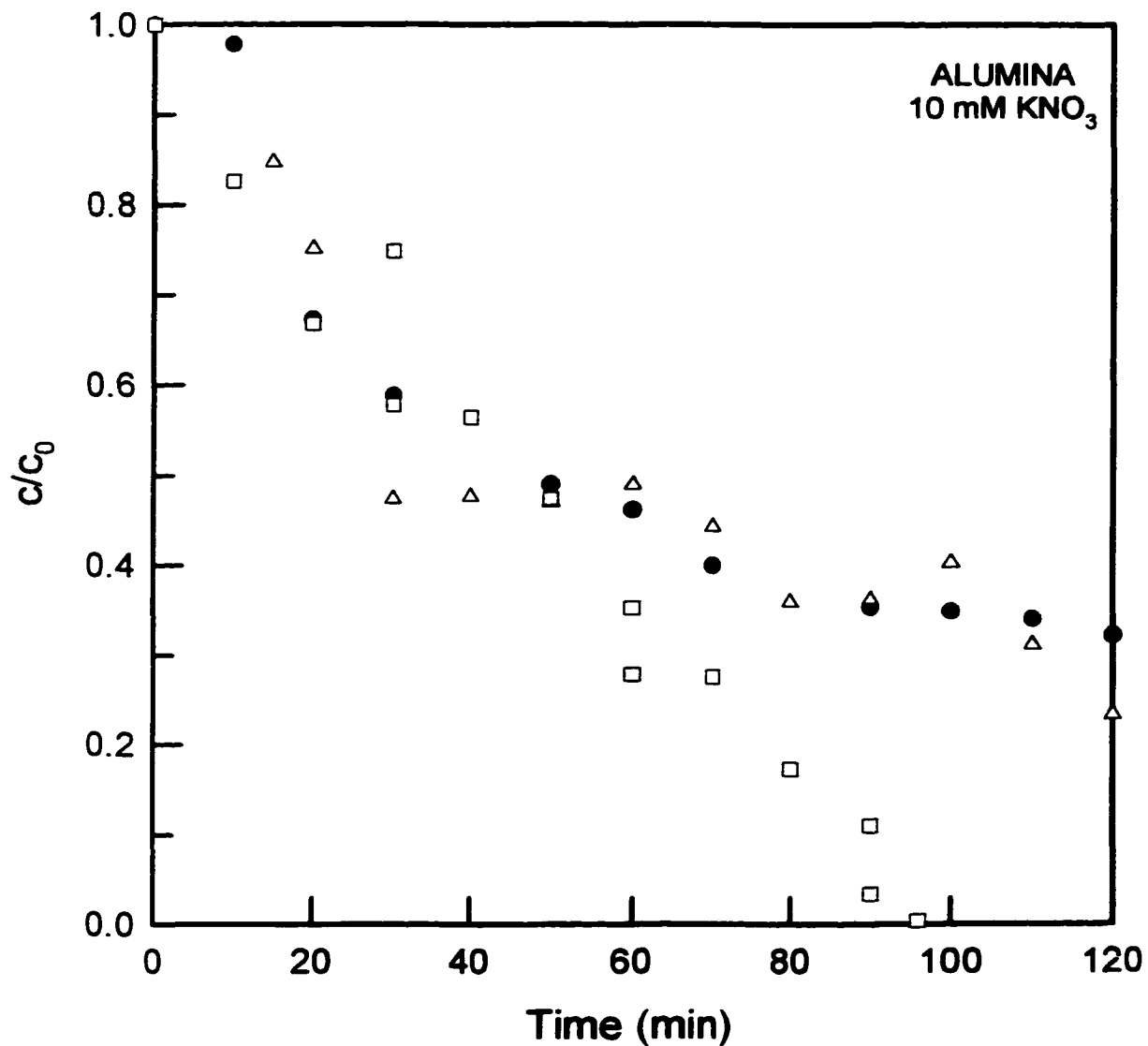
Figure 2.3: Influence of electric field on alumina particle removal by electrocoagulation. (Concentrations measured 2.5 cm below the surface. $c_0 \approx 0.40$ w/v%; $\sigma \approx 1350$ μS/cm; pH $\approx$ 5.7; E = 3.6 V/cm, with polarity switched every 2 minutes. Legend: ●, field applied for entire experiment; △, field applied for first 15 minutes of experiment; □, field applied for 5 minutes, off for 10 minutes, on for 5 minutes, and so on.)

ionic strengths and for different electric field application schemes. Electrocoagulation was found to be most effective when the electric field was applied intermittently.

In low-conductivity ($< 20\,\mu S/cm$) alumina and silica suspensions, aggregation was not observed. Electrophoretic mobility and size measurements indicated that the collected solids were unaltered by the separations process. Figures 2.4a & b show the buildup of particles on the bottom of the separation chamber and the depletion of suspended solids from the top of the suspension. During these experiments on low conductivity suspensions, a clear fluid layer developed on the surface of the suspension, as depicted in Figure 2.5. The precipitous drop in concentration, shown at 2 hours in Figure 2.4b, occurred when the clear layer thickness had increased to include the sampling position. The particles collected on the bottom of the chamber showed no detectable change in size or electrophoretic mobility. The absence of any aggregation or changes in the electrophoretic mobility indicates that the active mechanism causing stratification of the solids was natural convection, which developed as a result of the suspended particles electrophoretically migrating away from the electrode of similar charge. This stratification process has been traditionally known as electrodecantation and is explained by the boundary-layer model summarized in section 2.3.

In contrast to the high-conductivity alumina suspensions described above, tests performed on silica suspensions at high conductivities ($\approx 250\,\mu S/cm$) exhibited no change in particle size or electrophoretic mobility. This results in part because silica suspensions at pH ≈ 9 are stabilized by a large electrical repulsive force between the particles. Experiments performed on silica suspensions of approximately $250\,\mu S/cm$ did
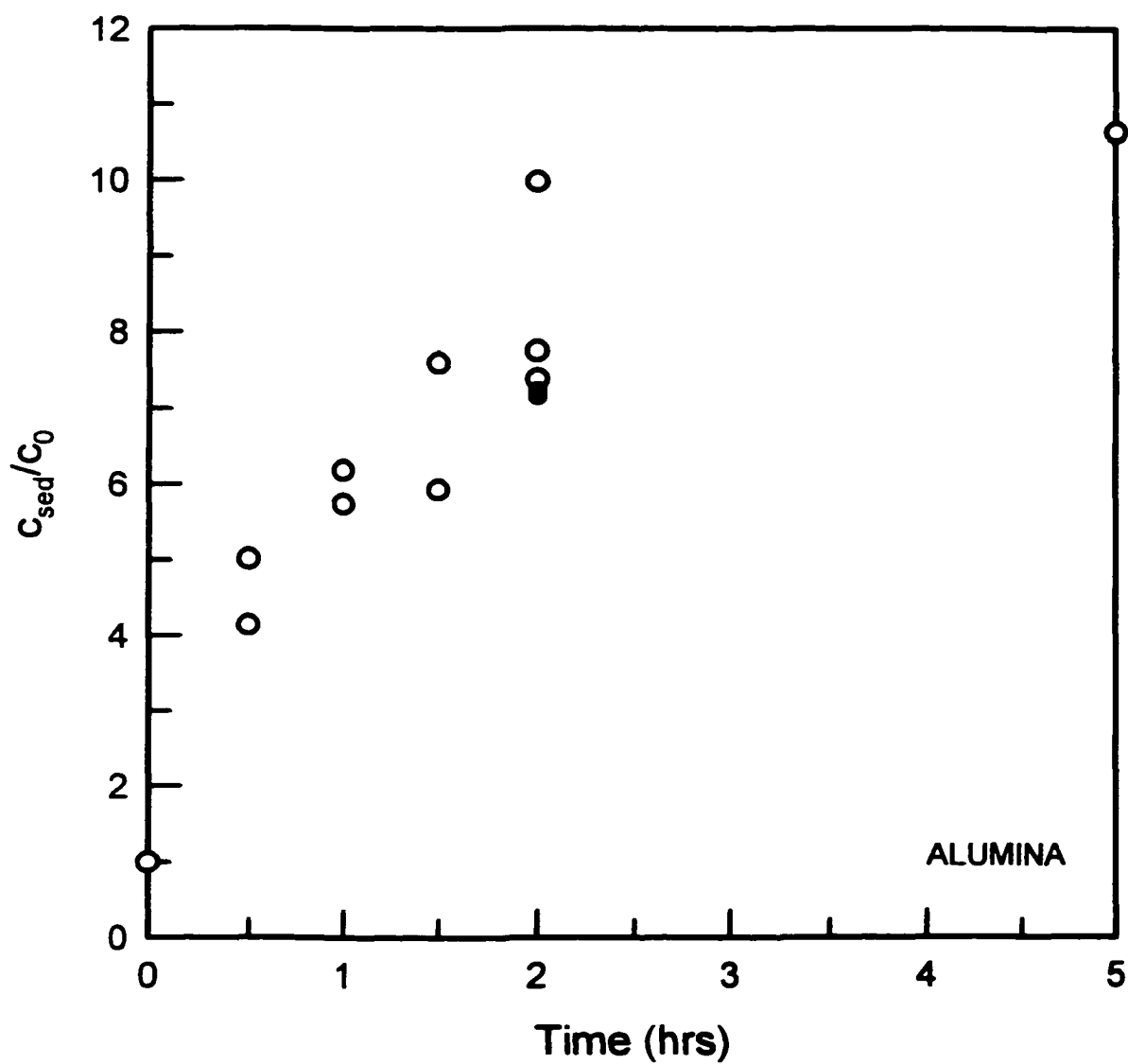
Figure 2.4a: Normalized concentration of solids measured on the bottom of the container. (203 nm alumina, $c_0 = 0.32{-}0.63$ w/v%, $\sigma \approx 20$ μS/cm, pH ≈ 4.2, E = 7.3 V/cm, polarity switched every 2 minutes. Legend: o, Stainless steel electrodes; ●, Inert platinum electrodes.)
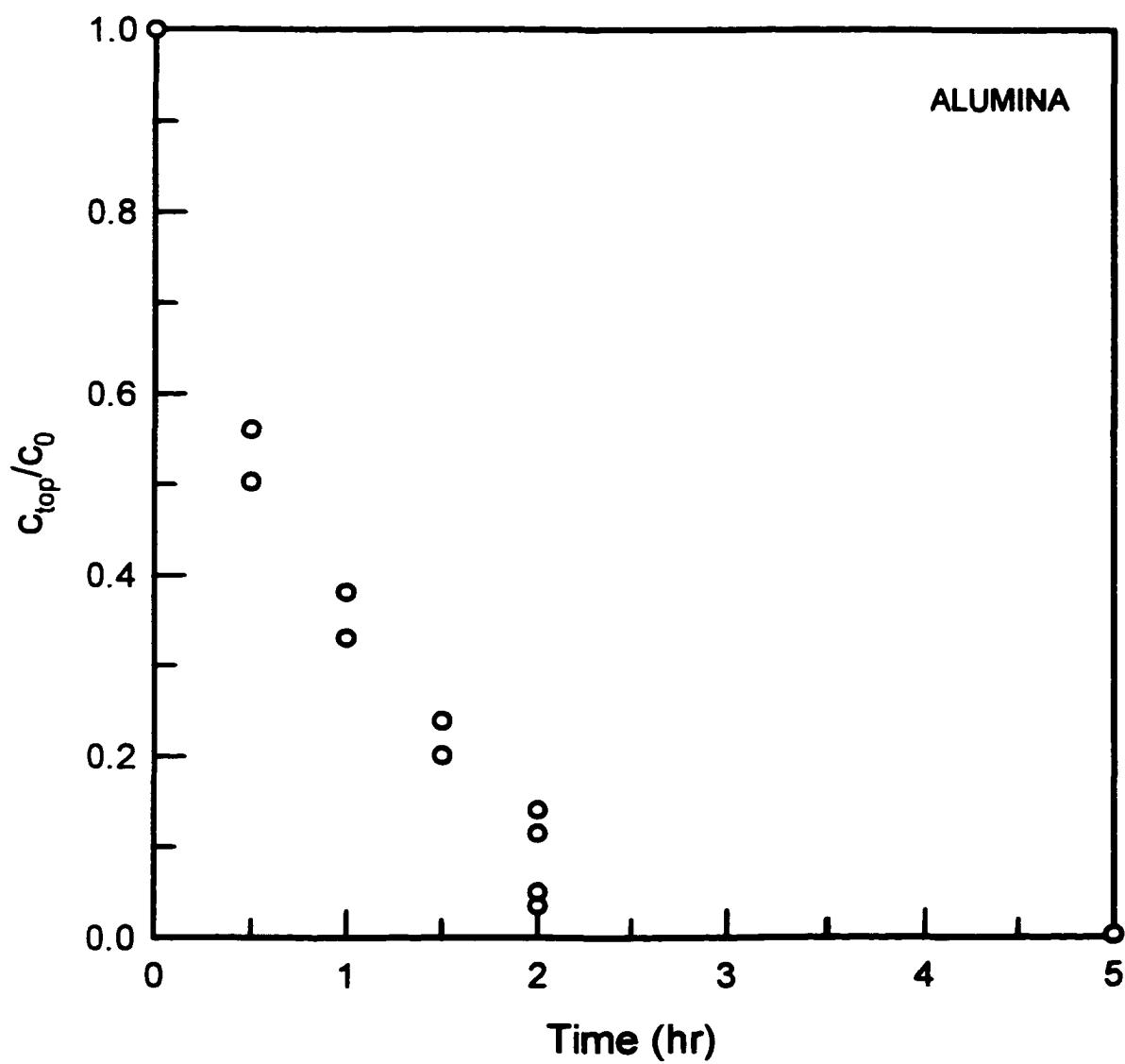
Figure 2.4b: Normalized concentration of solids measured 2.5 cm below the surface. (203 nm alumina, $c_0 = 0.32$–0.63 w/v%, $\sigma \approx 20$ μS/cm, pH ≈ 4.2, E = 7.3 V/cm, polarity switched every 2 minutes, with stainless steel electrodes.)
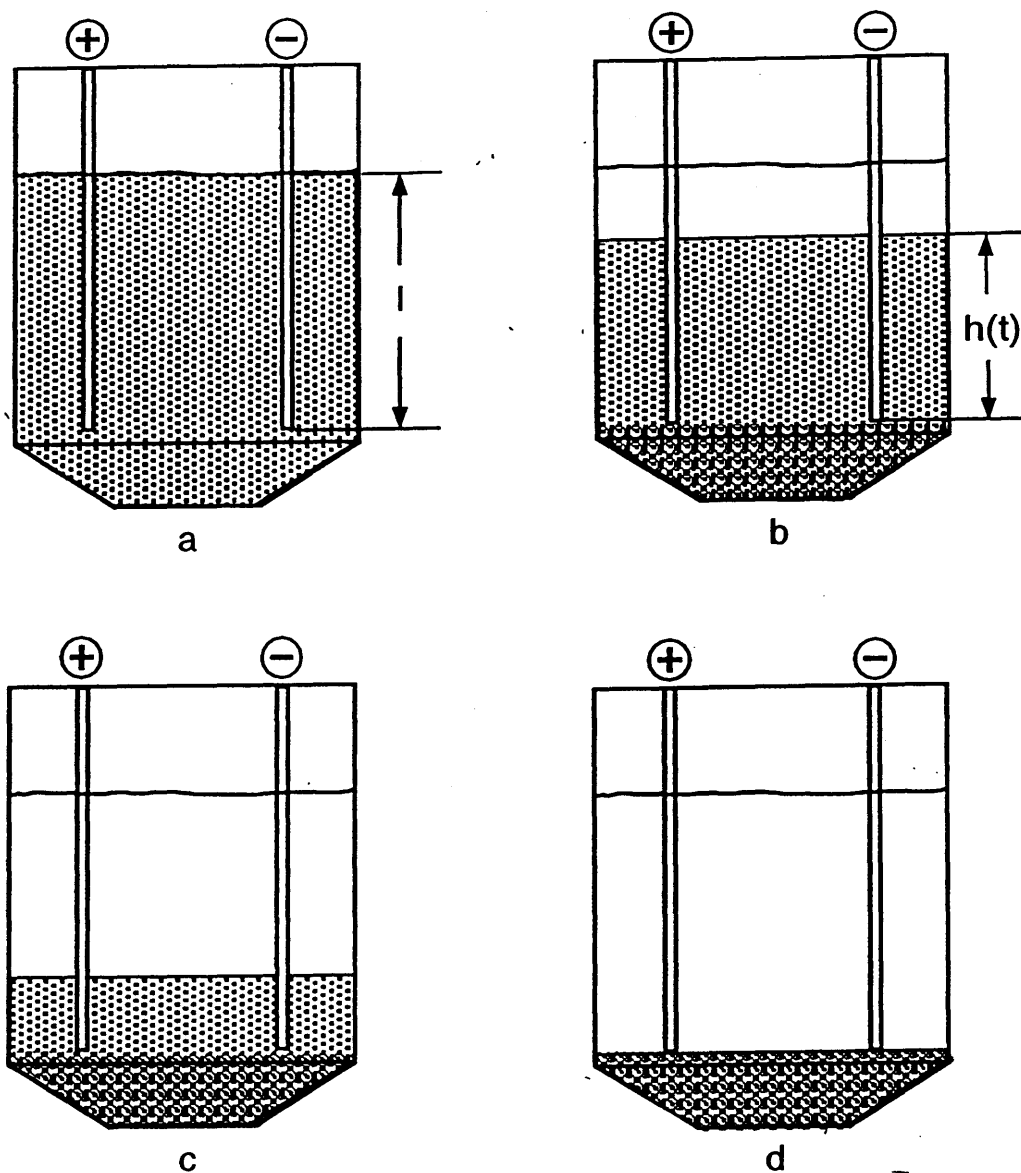
Figure 2.5 The qualitative features of batch electrodecantation of stable colloidal dispersions. a. a uniform dispersion at the inception of the experiment. b. a clear layer forms atop a particle-laden region, particle concentration increases beneath the electrodes. c. the clear layer grows with time. d. the end of the experiment: the clear layer reaches the bottom of the electrodes and continued application of the field produces little subsequent change. The initial height of the suspension above the bottom of the electrodes is denoted l (panel a); $h(t)$ indicates the suspension height at subsequent times t (panel b).

not develop a clear fluid layer (see Figure 2.6) on the surface of the suspension, though electrodecantation was determined to be the separation mechanism. One-dimensional simulations, summarized in section 2.5, show that in high-conductivity suspensions, a clear fluid boundary layer fails to develop at the electrodes. This results in particle-laden fluid being reentrained onto the top of the suspension, preventing the formation of a clear fluid layer on the surface.

At the completion of the electrodecantation experiments, conductivity and pH measurements were recorded for seven different sample positions. These measurements showed that vertical stratification of both the pH and conductivity had developed. The reason for the stratification was explained by the boundary-layer model (section 2.3.2) and then confirmed by numerical simulations presented in section 2.5.

To summarize, the experimental results demonstrated that two distinct solid-liquid separation mechanisms could be employed to remove particles from dilute suspensions, viz. electrocoagulation and electrodecantation. Electrocoagulation was operative in high-conductivity alumina suspensions; large aggregates were observed to form when an electric field was applied. In low-conductivity alumina and silica suspensions, electrodecantation occurred; electrophoretic mobility and size measurements indicated that the collected solids were unaltered by the applied electric field. During electrodecantation of these low-conductivity suspensions, a clear fluid layer developed on the surface. High-conductivity silica suspensions did not manifest this clear fluid layer, though electrodecantation was determined to be the controlling separation mechanism.
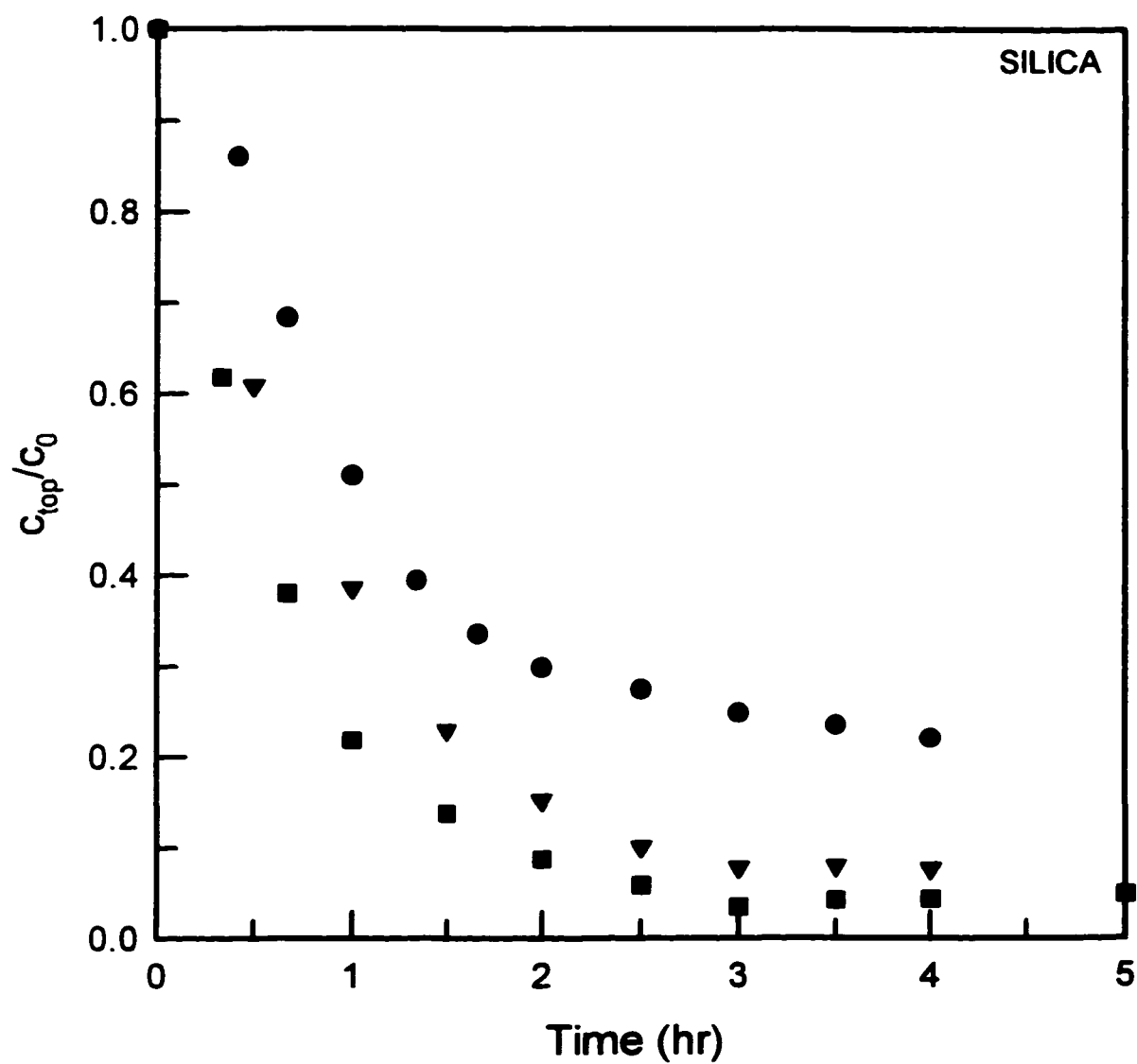
Figure 2.6: Normalized concentration of solids measured 2.5 cm below the surface. (208 nm silica, $c_0 = 0.66$ w/v%, $\sigma \approx 250$ μS/cm, pH ≈ 9.3, no polarity switching. Legend: ●, E = 2.5 V/cm; ▼, E = 5.0 V/cm; ■, E = 10.0 V/cm.)

At the conclusion of the electrodecantation experiments, measurements indicated that conductivity and pH strata had developed in the separation chamber.

2.3 Boundary-Layer Model of Electrodecantation

A boundary-layer model was developed to quantitatively establish the principles of electrodecantation and, thus, explain the development and growth of a clear fluid layer on the surface of colloidally-stable low-conductivity suspensions. In addition, the boundary-layer model was used to understand the formation of pH and conductivity gradients during electrodecantation experiments. The following sub-sections (2.3.1 and 2.3.2) summarize the development and implications of the model, which are given in greater detail in Appendix B.

2.3.1 Balance Laws and Scaling

As noted in chapter 1, Blank and Valko (1928) were first to explain that electrodecantation resulted from natural convection. To describe the natural convection associated with electrodecantation in stable colloidal dispersions, a simple model was developed (Appendix B). This model predicts that a clear fluid boundary layer will form next to one of the electrodes when an electric field is applied to a stable suspension. Provided the particles are more dense than the surrounding fluid, this clear fluid will experience a large buoyancy force causing it to rise upwards, along the electrode, and be layered onto the surface of the suspension (Figure 2.7). The thickness of the clear layer on top of the suspension will grow with time as more clear fluid is convected upward.
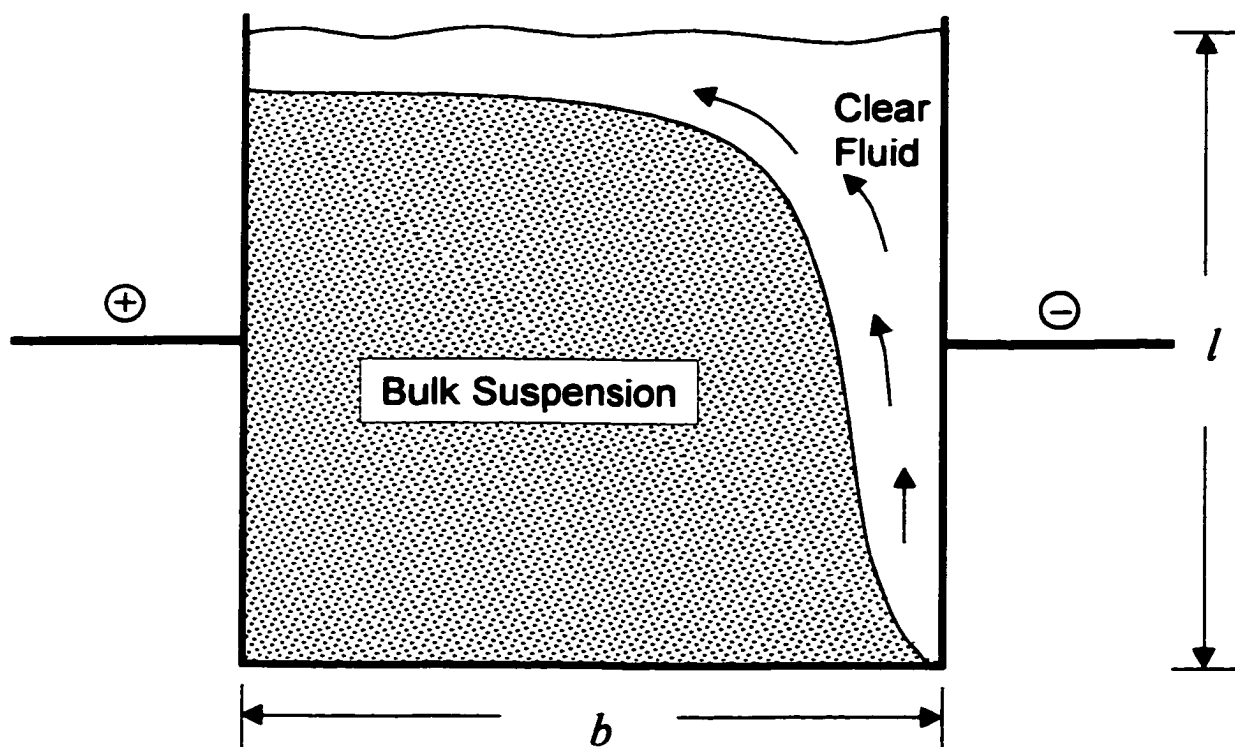
Figure 2.7: Sketch of the phenomenon that occurs during electrodecantation. In this figure, negatively charged particles are shown to electrophoretically migrate away from the cathode, forming a clear fluid layer which rises to the surface. Note, for illustrative purposes, the thickness of the fluid layer rising at the cathode has been exaggerated, and the electrodes extend to the bottom of the chamber.

Assuming that the system is isothermal and free of ion gradients, the balance laws that apply are the conservation of momentum and mass. The momentum balance is written in differential form, but is expressed in terms of an ensemble average, or bulk average, suspension velocity. This velocity is denoted $\mathbf{u}$ and, formally at least, is the local velocity at position $\mathbf{x}$ obtained by averaging over a representative volume element in the neighborhood of $\mathbf{x}$. Note that the representative volume element encompasses both fluid and particles, so $\mathbf{u}$ is not the locally averaged fluid velocity. Formulated in this manner, the (dimensionless) momentum balance reads

$$\mathrm{Re}\,\rho(\Phi)\left\{\frac{\partial \mathbf{u}}{\partial \tau} + \mathbf{u} \cdot \nabla \mathbf{u}\right\} = -\nabla P + \mu(\Phi)\nabla^2 \mathbf{u} - \Lambda(1 - \Phi)\hat{\mathbf{e}} \qquad (2.1)$$

with

$$\nabla \cdot \mathbf{u} = 0, \qquad (2.2)$$

where: Φ is the local particle volume fraction; P is the dimensionless dynamic pressure; τ is the scaled time; $\rho(\Phi)$ and $\mu(\Phi)$ are, respectively, the suspension density and viscosity normalized to their pure fluid values ρ_f and μ_f; and $\hat{\mathbf{e}}$ is a unit vector in the direction of gravity. The scale factors used in (2.1) are given in Table 2.1, along with related parameters and dimensionless groups (e.g. Re, Λ). A list of nomenclature is given in section 2.8.

Equation (2.1) is completely analogous to the suspension momentum balance used by Acrivos and Herbolzheimer (1979) to substantiate PNK theory for particle settling in inclined vessels; (2.1) applies as long as the particle Reynolds number Re_p is small. Here $\mathrm{Re}_p \equiv \rho_f v_0 a_p / \mu_f$, where a_p is the particle radius and v_0 is the characteristic

Table 2.1: Representative values for parameters, scale factors, and dimensionless groups. The magnitudes are consistent with the experimental conditions described in section 2.2.

	Magnitude
Parameter	
a_p, particle radius	1 to 2×10^{-7} m
ρ_p, particle density	2 to 4×10^3 kg/m^3
D, particle diffusion coefficient	2×10^{-12} m^2/s
M_E, particle electrophoretic mobility	2 to 4×10^{-8} m^2/ V·s
E, electric field strength	100 to 1000 V/m
σ, electrical conductivity	1 to 2×10^{-3} S/m
Scale factor	
c_0, concentration	initial volume fraction of particles, 10^{-3}
v_0, velocity	electrophoretic velocity $v_e(c_0)$, 10^{-5} m/s
l, length	electrode height, 10^{-1} m
l/v_0, time	10^4 s
$\mu_f v_0/l$, stress	10^{-8} to 10^{-7} N/m^2
Dimensionless group	
Re, Reynolds number	$\rho_f v_0 l / \mu_f$, $O(1)$
Λ, Grashof over Reynolds number	$l^2 g(\rho_p - \rho_f)c_0 / \mu_f v_0$, $O(10^7)$
Pe$_e$, electrical Peclet number	$v_0 l / D$, $O(10^6)$
Re$_p$, particle Reynolds number	$\rho_f v_0 a_p / \mu_f$, $O(10^{-6})$
Pe$_p$, particle Peclet number	$v_0 a_p / D$, $O(1)$

velocity of the particles, which is their electrophoretic velocity v_e at a representative volume fraction in the suspension (e.g. the initial volume fraction c_0). Using typical values for the relevant quantities, one can show that Re_p is $O(10^{-6})$.

The term $-\Lambda(1-\hat{\Phi})\hat{e}$ on the right hand side of (2.1) represents a gravitational body force; this body force is nil when the volume fraction of the suspension is equal to c_0 (i.e. when the scaled volume fraction $\Phi = 1$). However, the parameter Λ is $O(10^7)$, so where the local volume fraction deviates from c_0, a strong buoyancy force results. It is this buoyancy force, which couples with the particle electrophoresis, to drive electrodecantation.

Because the buoyancy force depends on the local volume fraction of particles, it is necessary to account for local variations in Φ. This is done through a particle conservation relation, viz.

$$\frac{\partial \Phi}{\partial \tau} + \mathbf{u}_p \cdot \nabla \Phi = -\Phi \nabla \cdot \mathbf{u}_s , \tag{2.3}$$

with

$$\mathbf{u}_s \equiv \mathbf{u}_p - \mathbf{u} = F(\Phi)\hat{\mathbf{E}} = \text{electrophoretic slip velocity of particles.}$$

Here $F(\Phi)$ is the volume fraction dependence of the scaled electrophoretic velocity and $\hat{\mathbf{E}}$ is the electric field. In writing equation (2.3), two approximations have been made. The first is that particle diffusion has been omitted. This requires that the electric Peclet number Pe_e, defined in Equation (1.2), be large. For typical values, Pe_e is $O(10^6)$. The second is that particle sedimentation has been ignored. For silica or alumina particles in the 100 nm size range, the electrophoretic velocity exceeds the Stokes sedimentation

velocity by a factor of roughly 500, assuming electrophoretic mobilities on the order of 10^{-8} $m^2/V \cdot s$ at field strengths of 10^3 V/m.

An important implication of equation (2.3) is that, unless there are significant volume fraction gradients in the suspension at the outset, volume fraction gradients can only develop as a result of events at the boundaries of the suspension. This can be seen by recognizing that, when there are no spatial gradients in Φ, the time derivative $\partial\Phi/\partial\tau$ vanishes.

2.3.2 Boundary Layer Scaling & Primary Implication of the Analysis

Because particle diffusion is negligible, the volume fraction variation propagates outward from the boundaries. In particular, the particles move away from the electrode at which they experience an electrostatic repulsion and establish a particle-depleted region in which $\Phi = 0$. In the bulk of the suspension, the particle volume fraction remains at $\Phi = 1$. One can estimate that the transition from the particle depleted region to the homogeneous bulk region is $O(l/Pe_e)$, which is about the size of a single particle. From a macroscopic viewpoint, the suspension segregates into a particle-depleted region and a homogeneous region with a sharp transition from one region to the other.

As noted previously, the particle-depleted region will experience a large buoyancy force, and this will drive the clear fluid layer upwards, causing it to flow along the electrode. To some extent, this rising clear fluid boundary layer is similar to a natural convection boundary layer that develops adjacent to a vertical, heated plate. The

buoyancy force on the fluid is balanced by viscous stresses, which resist the motion of the fluid upwards and continuity requires that the rising fluid be replaced.

The resultant of these three effects: buoyancy, viscous stresses, and the need to replace the rising fluid, is that the particle-depleted region does not grow indefinitely. In fact, on a time scale on the order of $\Lambda^{-1/3}l/v_0$, the depleted layer has ceased to grow and has established a steady arrangement. A detailed analysis of the particle depletion at the electrodes follows rather closely that of Acrivos and Herbolzheimer (1979) for sedimentation in tanks with inclined walls, and the features of the analysis that apply to electrodecantation are highlighted in Appendix B. From the analysis in Appendix B, it was found that for typical values of Λ, the electrophoretic velocity, and the electrode dimensions (cf. Table 2.1), the boundary layer develops in approximately $\Lambda^{-1/3}l/v_0 = 50$ sec and is of thickness $O(\Lambda^{-1/3}l) = 0.5$ mm.

The boundary layer analysis has several important implications for electrodecantation. First, the boundary layer is thin compared to the dimensions of a separation chamber, but still large compared to the particle size. Provided the rising boundary layer is stable and is folded onto the top of the suspension, one can decant clear fluid to the top of the chamber. The rise of the clear fluid sets the core of the suspension in motion, but to the level of approximation employed here, Acrivos and Herbolzheimer show that motion within the core of the suspension has little influence on the particle distribution. As a consequence, the suspension is forced downward and particles concentrated at the chamber bottom.

The analysis in Appendix B also shows that the thickness of the clear layer on the top of the suspension will grow as $l - h(t)$, where

$$h(t) = l \exp\left(-\frac{v_0}{b} t\right) \tag{2.4}$$

is the height of the suspension above the bottom of the electrode and t is time. When the thickness of the clear fluid surface layer becomes comparable to that of the electrode height, electrodecantation will cease.

The experimental data in Figure 2.8 illustrates the decrease in the suspension height, normalized to the electrode height, as a function of dimensionless time $v_0 t/b$. As can be seen from the figure, the data overlap within experimental uncertainties even though the conditions between experiments varied significantly. Periodically switching the polarity of the electric field, described below in this section, did not have a significant effect on the decantation as long as the period of reversal was long compared to the time required to form a clear fluid boundary layer adjacent to one of the electrodes.

Also shown in Figure 2.8 is that the rate of decantation measured in the experiments at long times is comparable to the decantation rate predicted by the boundary layer model. A line is fit to the data on Figure 2.8 for dimensionless times greater than 3.75, and the slope of this line is determined to be 0.42; a slope of 0.43 would be predicted from equation (2.4). This suggests that there is considerable agreement between the experimental data and the boundary-layer model. The overprediction of the decantation rate at short times, may be explained by myriad factors: e.g. electrode surfaces, electrochemical reactions at the electrodes, cell geometry, and pH and
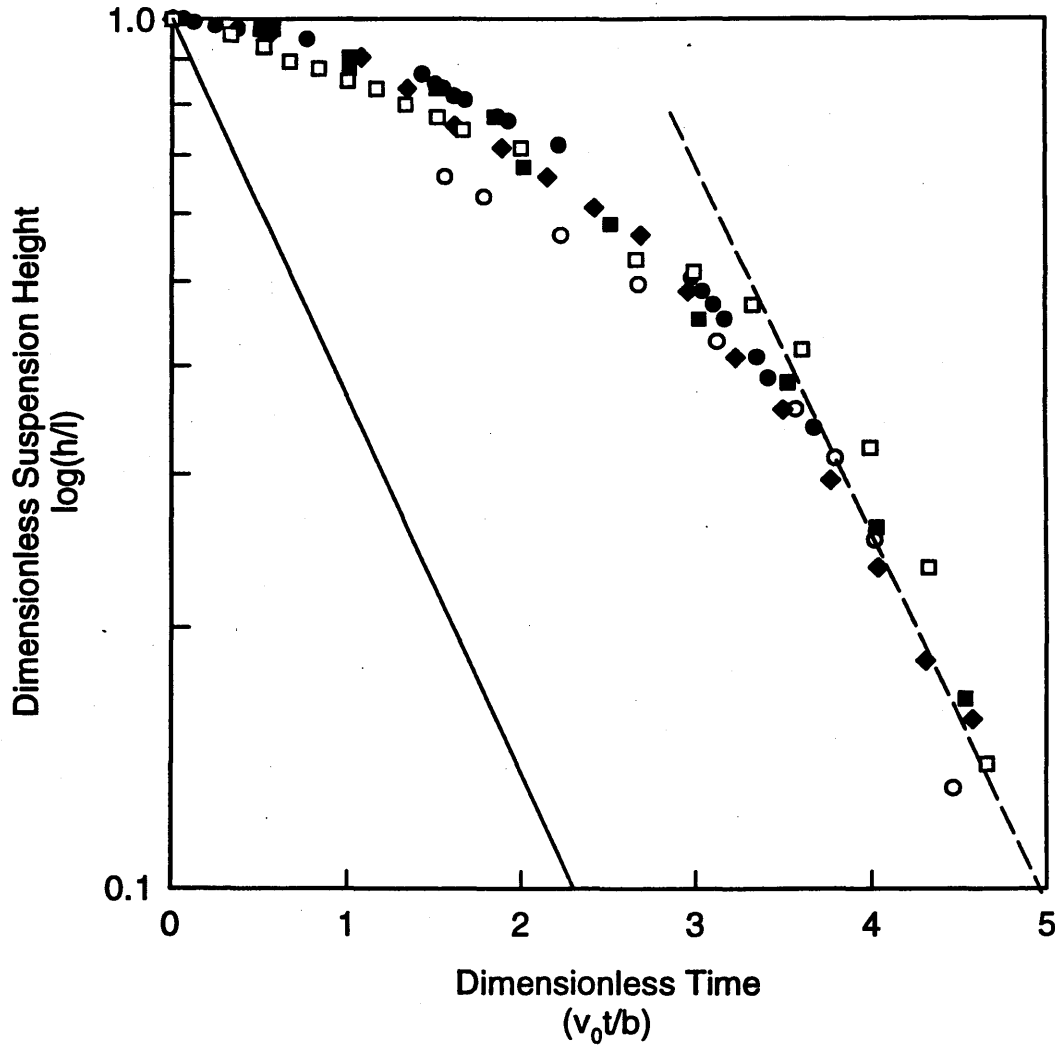
Figure 2.8: The normalized height of the suspension h/l versus dimensionless time $v_0 t/b$. Data are shown on a semi-$\log_{10}$ scale and the height of the suspension is reckoned from the bottom of the electrodes; $l = 11.5$ cm and $b = 11$ cm. Legend: $\square$, SiO_2, $c_0 = 2.3\times10^{-3}$, $\mu_e = -2.8\times10^{-4}\ cm^2/V\cdot s$, nominal $E = 7.3\ V/s$ with polarity switched every 30 min; o, SiO_2, $c_0 = 2.3\times10^{-3}$, $\mu_e = -2.8\times10^{-4}\ cm^2/V\cdot s$, nominal $E = 9.8\ V/s$ with polarity switched every 15 min; ■, Al_2O_3, $c_0 = 1.3\times10^{-3}$, $\mu_e = 4.2\times10^{-4}\ cm^2/V\cdot s$, nominal $E = 7.3\ V/s$ with polarity switched every 4 min; ◆, Al_2O_3, $c_0 = 1.3\times10^{-3}$, $\mu_e = 4.2\times10^{-4}\ cm^2/V\cdot s$, nominal $E = 3.9\ V/s$ with polarity switched every 30 min; •, Al_2O_3, $c_0 = 9.7\times10^{-4}$, $\mu_e = 4.2\times10^{-4}\ cm^2/V\cdot s$, nominal $E = 0.45\ V/s$ with no polarity switching. The solid line is Eqn (2.4). The dashed line is the best-fit to the data for $v_0 t/b > 3.75$.

conductivity gradients. In developing the boundary-layer model, electrodes were assumed to be electrochemically-inert, flat surfaces located at the sides of the container, providing a uniform electric field throughout the chamber. In actuality, the electrodes used in the experiments were stainless steel wire mesh and were displaced from the chamber walls (Figure 2.1). The stainless steel wire (0.24 mm) and mesh spacing (0.41 mm) are comparable to $\Lambda^{-1/3}l \approx 0.5$ mm, the thickness of the predicted particle-free boundary layer. These discrepancies give reason to believe that the electric field was neither entirely uniform nor perpendicular to the electrode surfaces. Furthermore, the simple model assumes that the electrodes extend down to the bottom of the separation chamber. As Figure 1 (Appendix A) illustrates, the experiments were performed with the electrodes submerged 11.5 cm into the suspension, leaving approximately four centimeters of dead space below the electrodes.

In addition to these geometric considerations, pH and conductivity gradients measured at the end of electrodecantation experiments provide further evidence that there are spatial variations in the electric field (see section 2.5). Over the course of an experiment, H^+ ions are consumed at the cathode, e.g.

$$2H^+ + 2e^- \leftrightarrow H_2(g) \tag{2.5}$$

while at the anode, H^+ ions are generated, e.g.

$$2H_2O \leftrightarrow 4H^+ + 4e^- + O_2(g) \tag{2.6}$$

Since SiO_2 particles are repelled from the cathode, a rising particle-free layer would convect higher pH and lower conductivity fluid to the top of silica suspensions. Conversely, Al_2O_3 particles are repelled from the anode, and this would cause lower pH

and higher conductivity fluid to rise to the top of alumina suspensions. The consequent pH and conductivity gradients are qualitatively consistent with those reported in sections 2.5.1 and 2.5.2 and because the measured changes are significant, it seems reasonable to conclude that the electric field varies with position in the chamber.

Finally, the boundary layer develops quickly compared to b/v_0, the time required for a particle to migrate electrophoretically across the electrode gap. Nevertheless, during this brief period, one can expect that some particles will deposit on the electrode toward which they are driven. Particle buildup on this 'other' electrode must be controlled or suppressed, if the desire is to effect a solid/liquid separation and concentrate particles on the chamber bottom. Particle deposition will also affect the applied electric field and, presumably, alter the process dynamics. As can be seen in Figure 2.8, periodic reversal of the electrode polarities can be used to control particle buildup at the electrodes without substantially altering the clearing rate of the suspension. This practical measure suffices so long as the period of reversal is long compared to the time scale for boundary layer development ($\Lambda^{-1/3}b/v_0$), but short compared to b/v_0.

2.4 Two-dimensional Model of Electrodecantation

As discussed in section 2.3.2, certain important features were omitted from the boundary-layer model. In this section, the results of two-dimensional numerical simulations, which where performed to examine the effect of cell geometry, are discussed and compared to the boundary-layer analysis.

2.4.1 Balance Laws and Scaling

The balance laws and scale factors are essentially the same as those described in section 2.3.1. The only significant differences are that particle diffusion has been included in the numerical simulations and, owing to the electrode geometry, the electric field may vary with position.

2.4.2 Numerical Method and Strategy

For modeling purposes, the electrodecantation chamber is represented by a two-dimensional box, with vertically-oriented electrodes on the left and right and electrically-insulated horizontal boundaries on the top and bottom (see Figure 2.7). In the model, the electrodes on the left and right boundaries do not necessarily extend to the bottom of the box.

To make comparisons to the boundary-layer model, two-dimensional simulations were performed under conditions where the ion concentrations remained uniform throughout the simulation. By removing the possibility of ion gradients, the effects of density gradients and the resulting buoyancy driven flow can be studied in isolation.

As noted in section 2.3, a coupled set of balance laws and boundary conditions must be solved to describe electrodecantation. Electrodecantation is governed by the formation of density gradients that develop as suspended particles electrophoretically migrate away from an electrode of similar charge. If the suspended solids are treated as macroions, the particle conservation relation is given by the following set of equations:

$$\frac{\partial \Phi}{\partial \tau} + \nabla \cdot f = 0 \qquad (2.7)$$

with

$$\nabla \cdot \mathbf{f} = \mathbf{u} \cdot \nabla \Phi - \mathrm{Pe}_e^{-1} \nabla^2 \Phi - \nabla \cdot \left(\Phi \hat{\mathbf{E}} \right);$$ (2.8)

where $\mathbf{f}$ is the flux of the suspended particles.

Table 2.2a and 2.2b provide the electrophoretic mobility data as a function of pH for silica and alumina particles. With the Debye-Huckel-Henry expression, the valence of the particles as a function of pH can be inferred from the electrophoretic mobility data, viz.

$$z = \frac{6\pi\mu_f a_p M_E}{e} \frac{(1 + \kappa a_p)}{f(\kappa a_p)}.$$ (2.9)

Here M_E is the particle electrophoretic mobility, μ_f is the fluid viscosity, a_p is the particle radius, and κ is the Debye screening parameter. The function $f(\kappa a_p)$ was defined by Henry and varies in a sigmoidal fashion from 1 to 1.5 (Mosher, 1992). The valence versus pH data, calculated from (2.9) are also given in Tables 2.2a and b and were used to establish electrophoretic mobility at other suspension ionic strengths.

Since ion gradients are omitted and constant voltage was applied to the suspension, a publicly-available elliptic equation solver (de Zeeuw, 1990) could be adapted to numerically solve Laplace's equation to determine the electrical potential on a two-dimensional grid. The elliptic equation solver takes the coefficients of a user provided linear system of 9-point difference equations on a rectangular grid and uses a multi-grid technique to determine the solution at each node. The number of nodes in each direction need not be the same. The following four boundary conditions were discretized and imposed: a potential is prescribed on the left and right electrodes to

Table 2.2a: Electrophoretic mobility and valence data as a function of pH for silica.

Silica, Low Conductivity					Silica, High Conductivity				
pH	Electrophoretic Mobility $\times 10^{-8}$ $(m^2/V \cdot s)$	Ionic Strength (M)	κa_p	Valence[*]	pH	Electrophoretic Mobility $\times 10^{-8}$ $(m^2/V \cdot s)$	Ionic Strength (M)	κa_p	Valence[*]
3.00	-0.11	9.98×10^{-4}	9.87	-98	2.73	-0.21	5.93×10^{-3}	24.1	-383
3.54	-0.44	2.86×10^{-4}	5.28	-235	3.58	-0.93	5.13×10^{-3}	22.4	-1637
4.08	-1.13	8.10×10^{-5}	2.81	-385	4.33	-1.45	5.02×10^{-3}	22.2	-2519
4.64	-2.05	2.07×10^{-5}	1.42	-463	5.01	-1.96	5.00×10^{-3}	22.1	-3398
5.36	-3.26	2.18×10^{-6}	0.46	-462	6.01	-2.74	5.00×10^{-3}	22.1	-4746
6.20	-3.93	3.30×10^{-7}	0.18	-456	7.39	-3.57	5.00×10^{-3}	22.1	-6193
6.49	-4.26	1.92×10^{-7}	0.14	-478	9.73	-3.12	5.03×10^{-3}	22.2	-5421
7.89	-4.93	7.82×10^{-7}	0.28	-616	10.62	-3.46	5.21×10^{-3}	22.6	-6117
9.20	-4.96	1.58×10^{-5}	1.24	-1044					

Diffusion Coefficient $= 2.58 \times 10^{-8} \ cm^2/s$

[*] Calculated from Equation (2.9)

Table 2.2b: Electrophoretic mobility and valence data as a function of pH for alumina particles.

<u>Alumina</u>

pH	Electrophoretic Mobility $\times 10^{-8}$ $(m^2/V \cdot s)$	Ionic Strength (M)	κa_p	Valence[*]
2.51	4.34	3.09×10^{-3}	18.5	6847
3.25	4.40	5.55×10^{-4}	7.85	3402
3.59	4.14	2.53×10^{-4}	5.29	2354
4.59	4.18	2.22×10^{-5}	1.56	1056
5.15	3.89	3.54×10^{-6}	0.63	646
5.99	3.87	5.19×10^{-7}	0.24	500
7.07	3.97	1.59×10^{-7}	0.13	472
8.01	2.67	1.03×10^{-6}	0.34	371
8.56	1.89	3.64×10^{-6}	0.63	316
9.07	0.22	1.18×10^{-5}	1.14	48
9.58	-1.93	3.80×10^{-5}	2.05	-570
10.01	-3.05	1.02×10^{-4}	3.36	-1250
10.51	-4.02	3.24×10^{-4}	5.98	-2509
10.91	-4.44	8.13×10^{-4}	9.47	-3993
11.91	-5.00	8.13×10^{-3}	30.0	-12093

Diffusion Coefficient = 2.43×10^{-8} cm^2/s

[*] Calculated from Equation (2.9)

provide the electric field; at the remaining surfaces, which are considered electrically insulating, the normal component of the local electrical field is required to vanish.

Because Re is less than or equal to $O(1)$, and motion within the boundary layer is essentially inertialess (cf. Appendix B), the suspension velocity is taken to be quasi-steady and thus not be integrated in time. At each time step in the numerical integration of equation (2.7), a quasi-steady suspension velocity, driven by the concentration field of suspended solids at that time step, is calculated. The suspension velocity is governed by (2.1), with the inertial and temporal acceleration terms omitted. To effect a numerical solution for the suspension velocity, the curl of (2.1) is taken, and the stream function Ψ is introduced. The momentum balance thereby becomes:

$$\nabla^4 \Psi = \Lambda \frac{\partial \Phi}{\partial X},$$ (2.10)

where Ψ is scaled on $v_c l$, and the velocity components follow as

$$u_x = \frac{\partial \Psi}{\partial Y} \text{ and } u_y = -\frac{1}{A}\frac{\partial \Psi}{\partial X}$$ (2.11)

with $A = b/l$. The velocity components are determined from the stream function using second order central differences on the interior nodes and are set to zero on the boundary nodes.

The stream function is prescribed as an arbitrary constant (taken to be zero) at each boundary, and the normal derivatives are assigned as zero at each boundary to satisfy the no-slip condition at the walls. On the top surface, a stress free condition is applied which requires that the second derivative of the stream function with respect to position in the normal direction (y-direction) equal zero. Equation (2.10) is discretized

on the interior nodes using second order central differences and on the boundary nodes using second order forward or backward differences where needed. The resultant discretized stream function equation is solved for Ψ at each node using the method of conjugate gradients; a publicly-available subroutine, written specifically to solve this problem (Bjorstad, 1980), was employed.

To advance the solids distributions forward in time, the following explicit time-step strategy was employed for the numerical integration of equation (2.7). The divergence of the particle flux f was determined using second order central differences on the interior nodes. Once $\nabla \cdot f$ was established for a given time, the component concentration is advanced explicitly in time using a second-order predictor-corrector time integration scheme called Phoenical Low Phase Error Flux-Corrected Transport (PLPE-FCT). The suspended solids are not allowed to pass through the boundaries.

PLPE-FCT is a monotonic flux-limiter algorithm developed by Boris and Book (1976) to solve general unsteady convection equations. An in-house code was written to apply this algorithm to the solution of electrodiffusional/hydrodynamic transport problems. A Strang-type operator splitting is used on the spatial derivatives (Book, 1981) to permit application of the one-dimensional PLPE-FCT flux limiter algorithm to two dimensions. The size of the time steps is determined by the stability limit of the PLPE-FCT scheme, viz.

$$\text{Co} = u_{max} \frac{\Delta t}{\Delta x} = \text{Pe}_c \frac{D\Delta t}{\Delta x^2} = 0.5 \qquad (2.12)$$

where Co is the Courant number and Δt is the size of the time step. The cell Peclet

number, Pe_c, is defined as $Pe_c \equiv u_{max}\Delta r/D$, where u_{max} is the maximum velocity (natural

convection and electrophoretic motion) of the particles, Δr is the distance between nodes

in the direction of u_{max}, and D is the species diffusion coefficient. To assure that stability

is maintained, a Courant number of 0.4 was used in the simulations. The previously

described steps are repeated for each time step and a summary of the simulation steps is

provided in Table 2.3.

Test calculations were performed to establish if each section of the code was

performing properly. Electromigration of proteins, treated as macroions, were simulated

using the PLPE-FCT modified code in one dimension and compared to figures (5-2, 6-6,

6-7, 6-9, 7-6, and 7-48) published by Mosher, et al. (1992). No significant differences

were seen between the published results and the results generated using the PLPE-FCT

modified code. To test the elliptic solver, a free convection problem with a known

analytical solution was solved, viz. natural convection induced by a linear temperature

profile in a high aspect ratio chamber (Bird, et al., 1960). The elliptic solver was also

used to solve Poisson's equation, with a constant forcing function, in one dimension and

the test results agreed with the analytic solution. Finally, to test the stream function

subroutine, two prototype problems with analytical solutions were solved; analytical

solutions for both buoyancy-driven flow in a high aspect ratio chamber and for lid-driven

flow in a long thin cavity agreed with the numerical results (Leal, 1992).

Table 2.3: Summary of numerical approaches.

Two-dimensional Simulations (Buoyancy-Driven Flow)

1. Calculate electric field by solving Laplace's equation for the electrical potential.

2. Calculate the stream function for current particle distribution from the momentum balance (2.10).

3. Calculate the suspension velocity from the stream function with (2.11).

4. Calculate the unsteady particle flux with (2.8).

5. Calculate the particle concentration at the new time, i.e. update the particle distribution, with (2.7).

6. Repeat steps 3 to 6.

One-dimensional Simulations (Ion Distribution)

1. Calculate pH, conductivity, and particle valence from initial conditions (2.9), (2.15)–(2.17).

2. Calculate the electric field for current ion and conductivity distribution with (2.18).

3. Calculate the unsteady fluxes for the particles and ions from (2.8) and (2.14).

4. Advance the particle and ion concentrations to the new time with (2.7) and (2.13).

5. Calculate new pH, conductivity, and particle valence from new particle and ion distributions, using (2.9), (2.15)–(2.17).

6. Repeat steps 2 to 6.

2.4.3 Results

To test the boundary-layer model scaling, clear layer growth, and effects of cell geometry, along with studying electrodecantation as a two-dimensional buoyancy-driven flow, simulations were performed for Λ of 10^3 and 10^4. It should be noted that the electrodecantation experiments, described in section 2.3.1, were performed at lambda $\approx 10^7$. Because a very thin hydrodynamic boundary layer develops at the electrodes for Λ $\approx 10^7$, a large number of nodes are required to resolve the boundary layer. This results in a prohibitively long time (ca. six months) to run a simulation, given the current algorithm and computational resources (see Chapter 3, Future Studies, for ways to address these limitations). Nevertheless, the boundary-layer formulation applies so long as $\Lambda^{-1/3} \ll 1$, with $Re \approx O(1)$, and two-dimensional simulations are manageable for $\Lambda < 10^5$.

For these simulations, the dimensions of the chamber were 10 cm × 10 cm and the electrodes were taken to cover the top $\frac{3}{4}$ of the side walls. An electrical potential drop of 40 V was applied between the electrodes. Figures 2.9 and 2.10 show the formation and evolution of a particle-depleted boundary layer at the cathode and the growth of a clear fluid layer on the surface for $\Lambda = 10^3$ and $\Lambda = 10^4$, respectively. It should be noted that the clear fluid layer extending well below the bottom of the electrode may be an artifact of the boundary conditions applied at the side walls. Figure 2.11 shows the streamlines for $\Lambda = 10^4$ at 555 minutes; it is evident from the figure that a strong upward flow develops at the boundary layer adjacent to the cathode. This buoyancy-driven flow results in the mapping of clear fluid onto the surface of the suspension and forces, by way of continuity, the suspension downward (Acrivos, 1979).
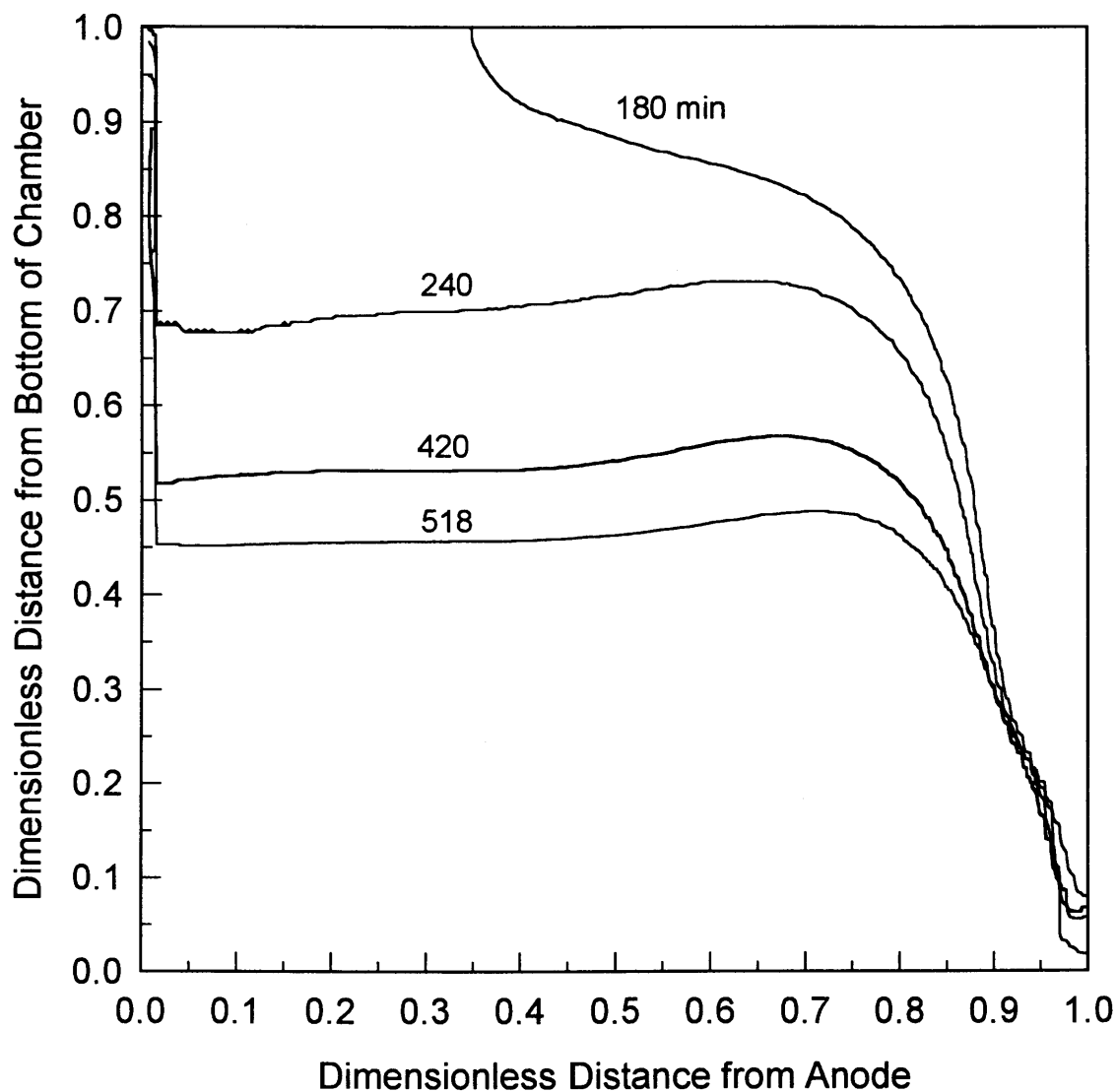
Figure 2.9: Contours of normalized volume fraction equal to 0.95. $\Delta\phi$ = 40 V, Λ = 10^3, Re = 0.26, silica mobility = 5.8×10^{-4} cm^2/V·s, conductivity = 250 μS/cm, and pH = 9.3. Initial silica concentration = 8×10^{-10} M, 1.95×10^{-3} M HNO$_3$ and 1.97×10^{-3} M KOH added to maintain a constant ion distribution. Anode on left boundary. Grid: 130 × 130.
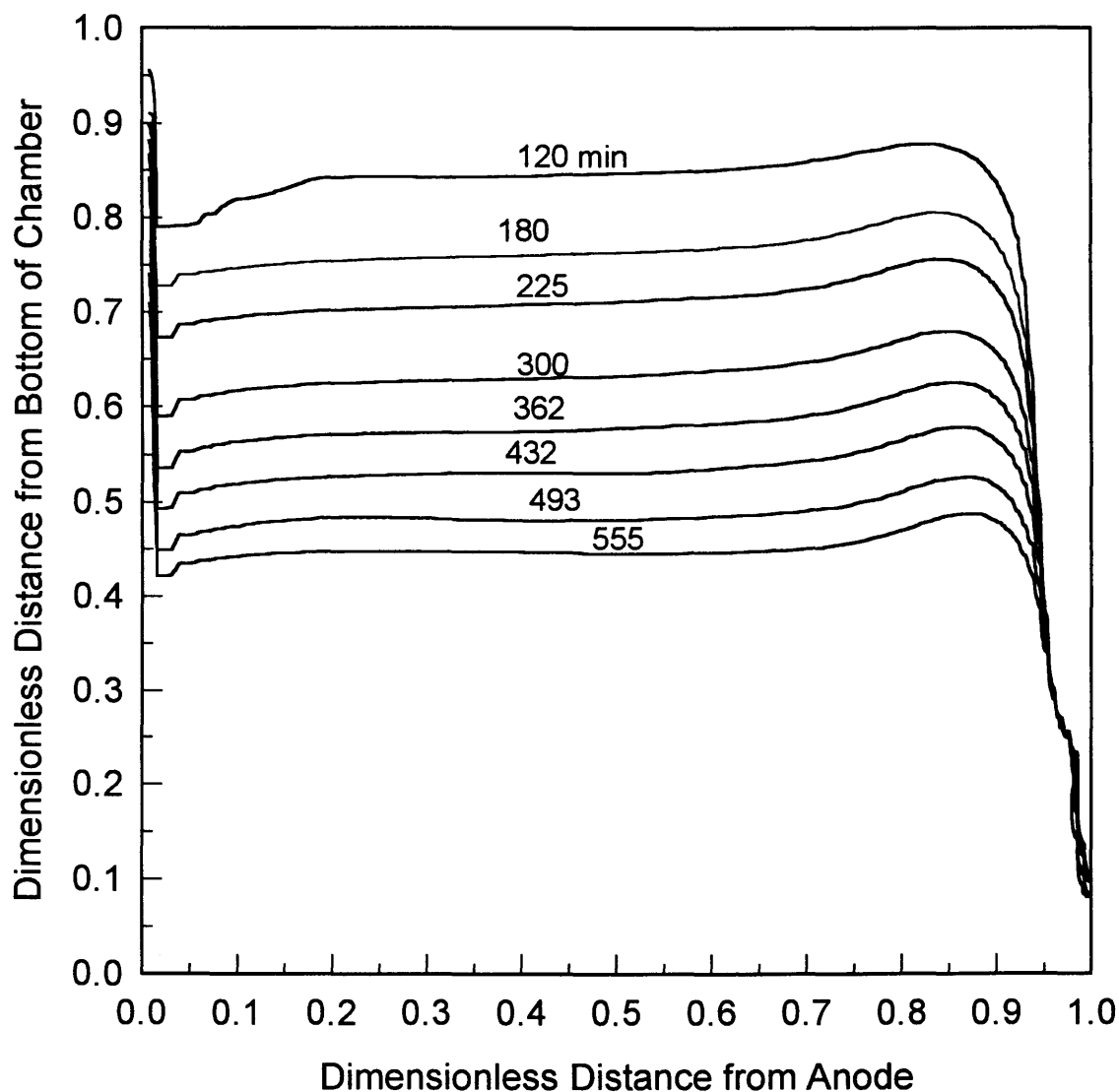
Figure 2.10: Contours of normalized volume fraction equal to 0.95. $\Delta\phi = 40$ V, $\Lambda = 10^4$, Re = 0.26, silica mobility = $5.8 \times 10^{-4} \text{ cm}^2/\text{V} \cdot \text{s}$, conductivity = 250 μS/cm, and pH = 9.3. Initial silica concentration = 8×10^{-10} M, 1.95×10^{-3} M HNO_3 and 1.97×10^{-3} M KOH added to maintain a constant ion distribution. Anode on left boundary. Grid: 130×130.
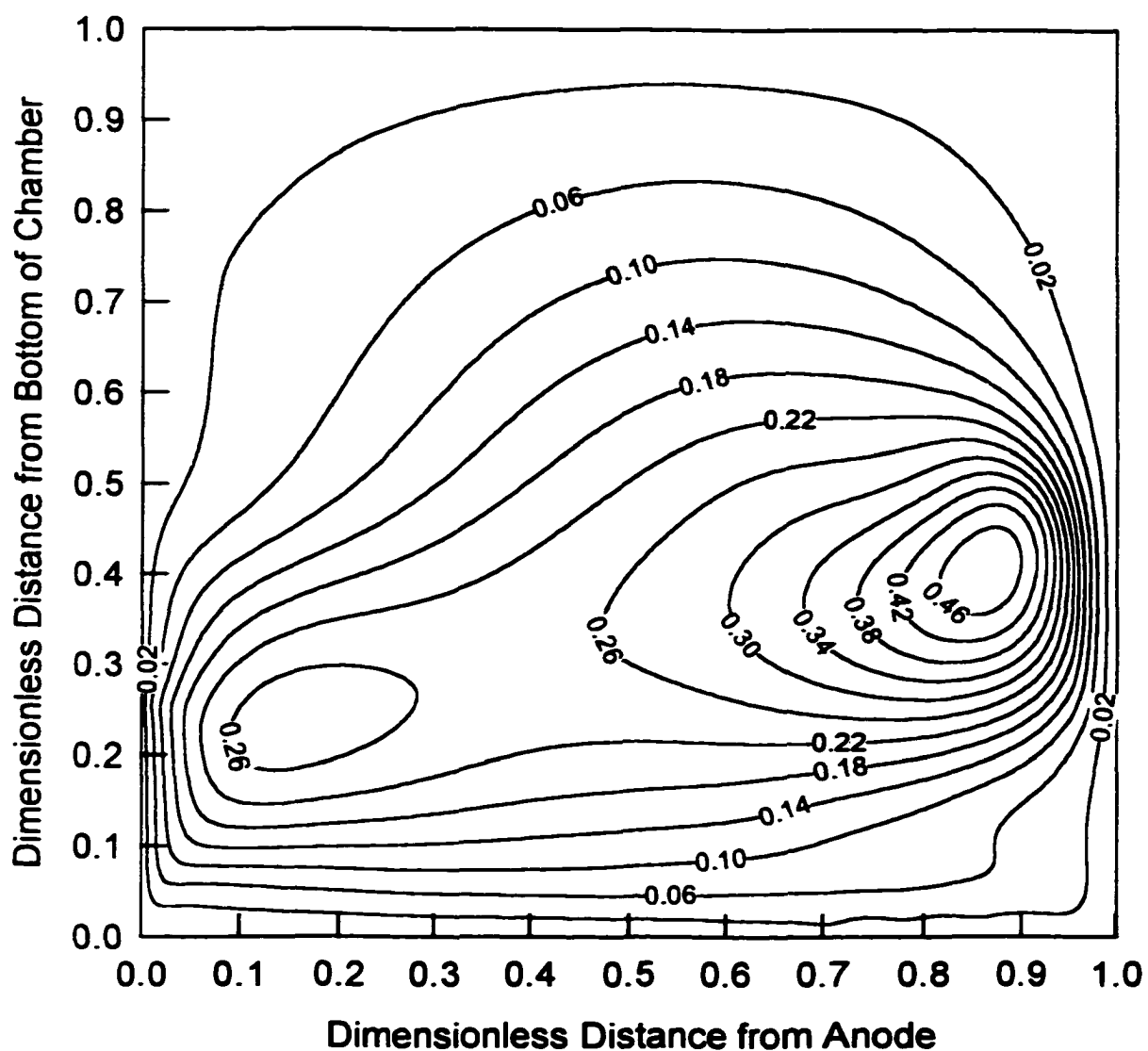
Figure 2.11: Stream function contours at 555 minutes. $\Delta\phi$ = 40 V, Λ = 10^4, Re = 0.26, conductivity = 250 μS/cm, and pH = 9.3. Initial silica concentration = 8×10^{-10} M, 1.95×10^{-3} M HNO_3 and 1.97×10^{-3} M KOH added to maintain constant ion distribution. Anode on left boundary. Grid: 130 × 130

Figure 2.12 shows concentration contours after 555 minutes for $\Lambda = 10^4$. These contour lines indicate the accumulation of solids in the bottom of the container, with some bias towards the corner next to the anode. Because Pe_e is on the order of 10^5, particle diffusion is inconsequential and electrophoretic motion of the particles (see Appendix B), coupled with the natural convection, will govern the separation process. As the separation unfolds, solids accumulate at the anode since there are no significant forces to keep the particles off the wall. This is evident in the simulations shown in Figures 2.9 and 2.10—and in the experiments, some particle deposition was observed when the polarity of the electrodes was not switched (see section 2.3.2). As the particles accumulated near the anode, solids begin to fall to the bottom of the chamber because of the density increase associated with the particle accumulation.

The contours for the normalized volume fractions of 0.05 and 0.95 indicate that, as the clear fluid is mapped onto the surface, a transition zone from clear fluid to the initial concentration of the bulk suspension may develop. Figure 2.13 compares the transition zone for simulations at lambda of 10^3 and lambda of 10^4. It should be noted, the formation of a transition zone may be an artifact of the (coarse) grid spacing used in these simulations and further studies are needed to investigate this matter. The formation of a transition zone is not predicted by the boundary-layer model, which states that a sharp interface should form if the boundary layer is stable.

As described in section 2.3.2 and Appendix B, the clear fluid boundary layer should grow to a thickness proportional to $\Lambda^{-\frac{1}{3}}$. For the two simulations shown in Figure 2.13, $\Lambda^{-\frac{1}{3}}$ is 1/10 and 1/22 for Λ of 10^3 and 10^4, respectively. The ratio of $\Lambda^{-\frac{1}{3}}$
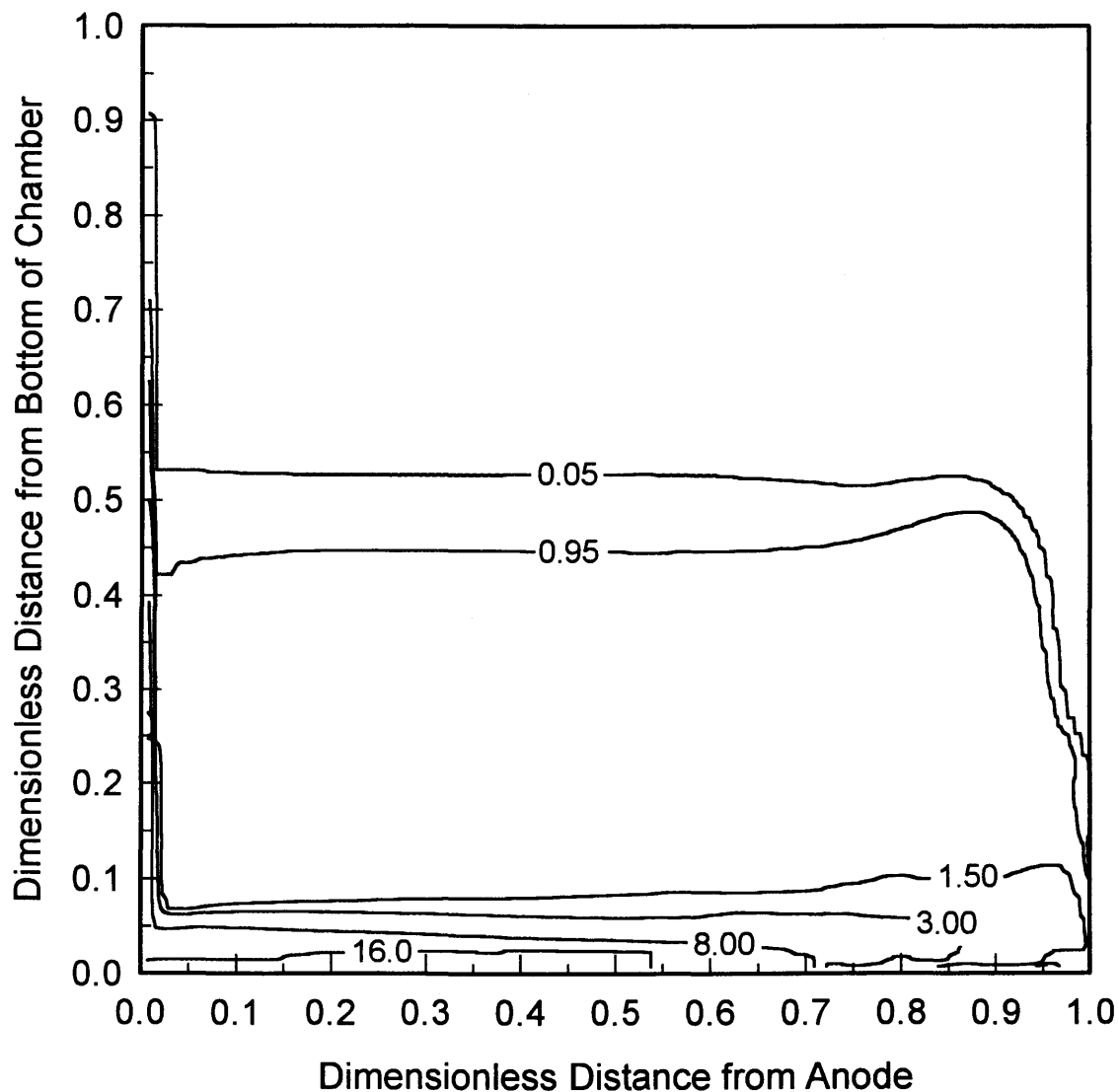
Figure 2.12: Increased concentration of solids on the bottom of the chamber. Contours of normalized volume fraction at 555 mins. $\Delta\phi$ = 40 V, Λ = 10^4, Re = 0.26, conductivity = 250 μS/cm, and pH = 9.3. Initial silica concentration = 8×10^{-10} M, 1.95×10^{-3} M HNO_3 and 1.97×10^{-3} M KOH added to maintain a constant ion distribution. Anode on left boundary. Grid: 130 × 130
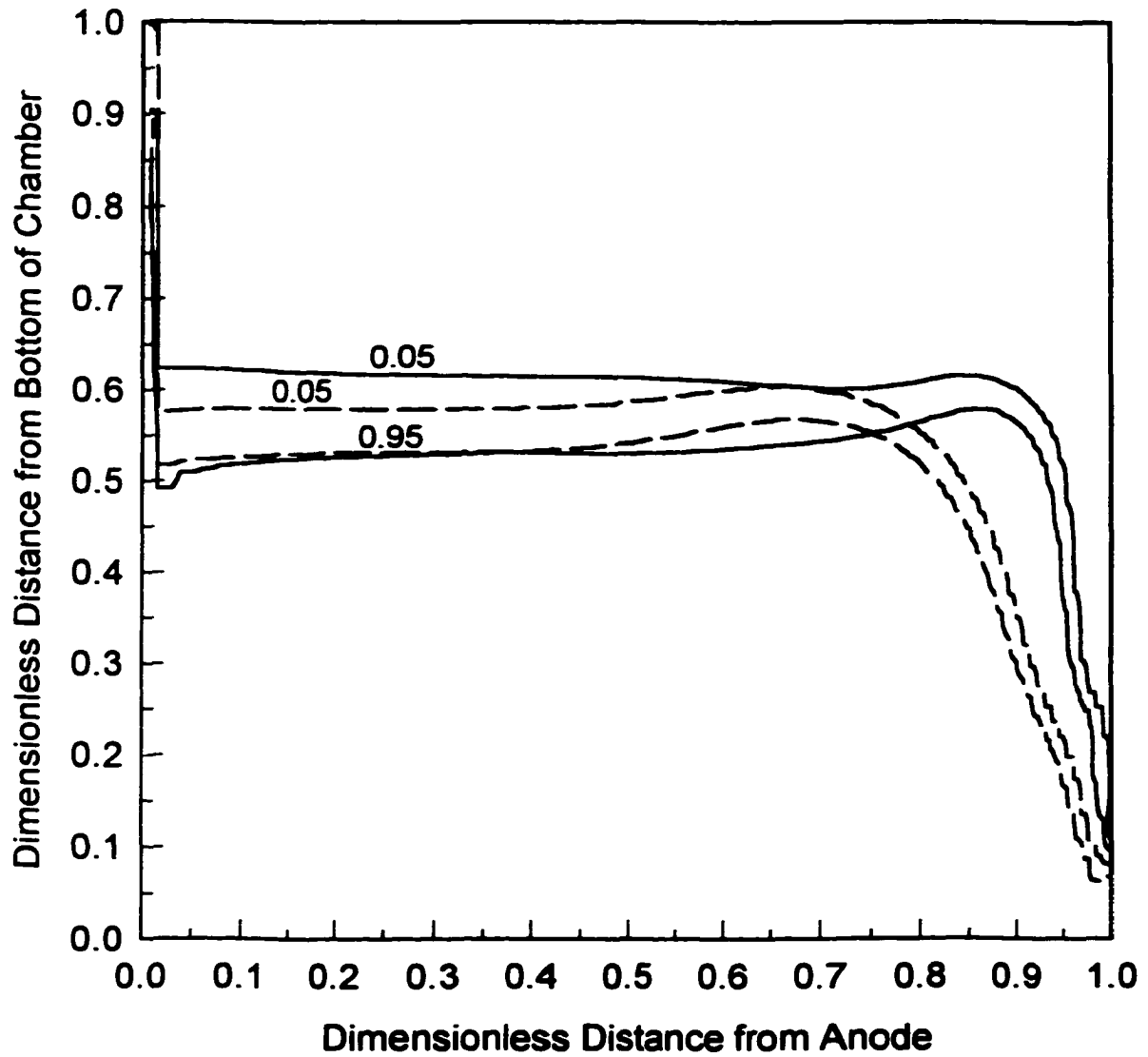
Figure 2.13: Contours of normalized volume fraction at 420 minutes. Dashed line for $\Lambda = 10^3$ and solid line for $\Lambda = 10^4$. $\Delta\phi = 40$ V, Re = 0.26, conductivity = 250 μS/cm, and pH = 9.3. Initial silica concentration = 8×10^{-10} M, 1.95×10^{-3} M HNO_3 and 1.97×10^{-3} M KOH added to maintain a constant ion distribution. Anode on left boundary. Grid: 130 × 130

for these two cases is 2.2. From the boundary-layer model, the boundary layer for Λ $O(10^3)$ should be approximately 2 to 2.5 times thicker than the boundary layer for Λ $O(10^4)$. Figure 2.13 shows that this is indeed the case.

To suppress deposition of solids on the electrode surface, experiments were performed where the polarity of the electric field was periodically reversed (section 2.2 and Appendix A). To investigate the prediction of the boundary-layer model that switching the electrode polarity would not significantly affect electrodecantation, numerical simulations were performed with a periodically-reversing electric field. Figure 2.14 shows the results of a simulation where the polarity of the electric field was reversed every 180 minutes. As is expected, the boundary layer reforms at the opposite electrode when the polarity is reversed. Also apparent from this figure is that, when the polarity is reversed, the accumulated solids at the electrode surface electrophoretically migrate towards the opposite electrode and disperse back into the bulk suspension.

Shown on Figure 2.15 are results from a simulation where the polarity was switch every 180 minutes (open circles), juxtaposed against the simulation without switching. The results shown in Figure 2.15 suggest that reversing the electric field polarity did not have a significant effect on the decantation. This should be the case if the frequency of reversal is long compared to the characteristic time required to form the boundary layer. For these results, the polarity was switched every 180 minutes and the characteristic time, $\Lambda^{-1/3}b/v_0$, was approximately 30 minutes. The slight effects due to switching can be attributed to the fact that the ratio of the frequency of reversal to the characteristic time is only 6. For the experiments summarized on Figure 2.8, the ratio of the frequency of
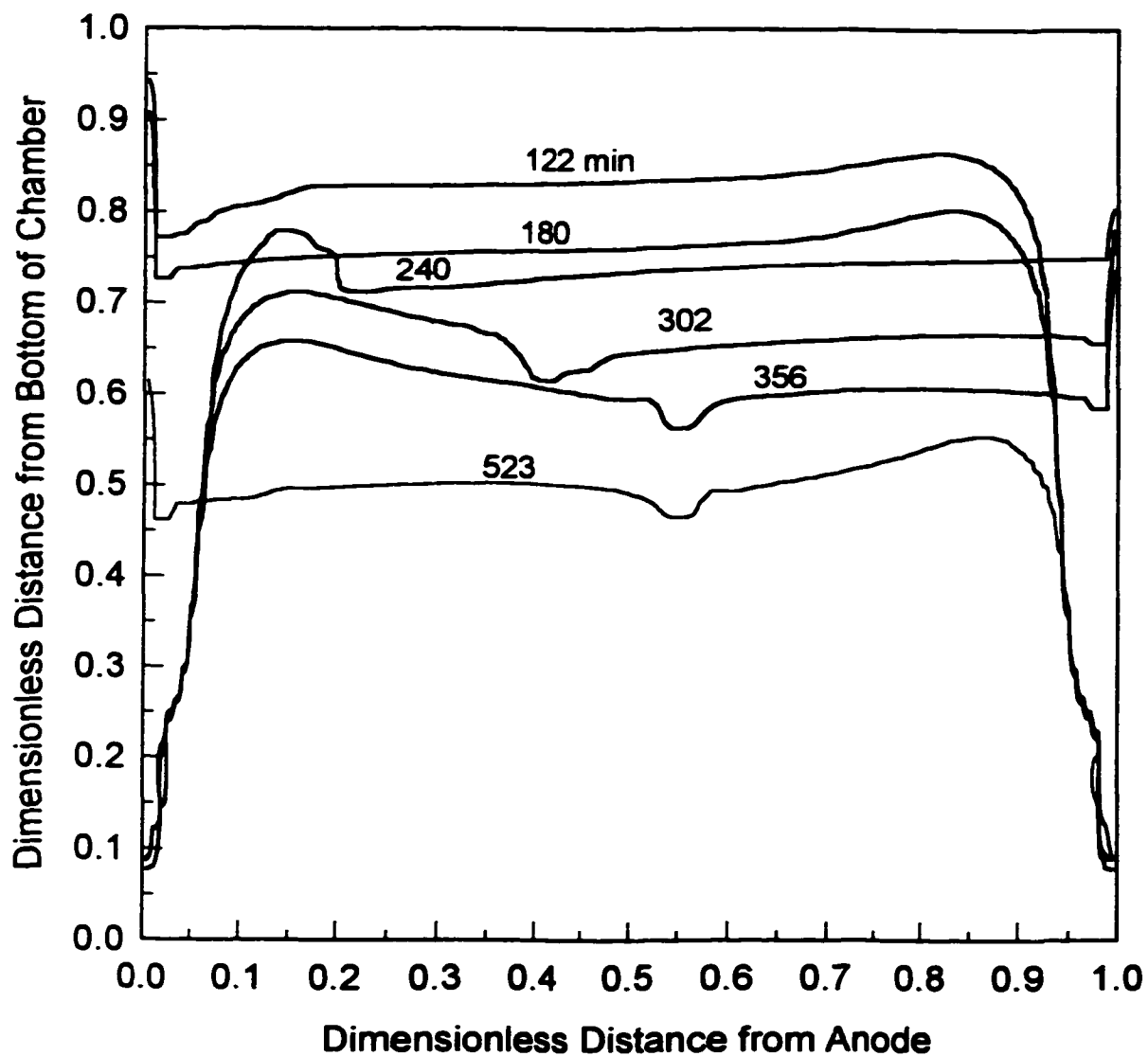
Figure 2.14: Contours of normalized volume fraction equal to 0.95. Polarity switched every 180 minutes, $b/(v_e\Lambda^{1/3}) \approx 30$ minutes. $\Delta\phi = 40$ V, $\Lambda = 10^4$, Re = 0.26, conductivity = 250 μS/cm, and pH = 9.3. Initial silica concentration = 8×10^{-10} M, 1.95×10^{-3} M HNO_3 and 1.97×10^{-3} M KOH added to maintain a constant ion distribution. Anode on left boundary. Grid:130 $\times$ 130
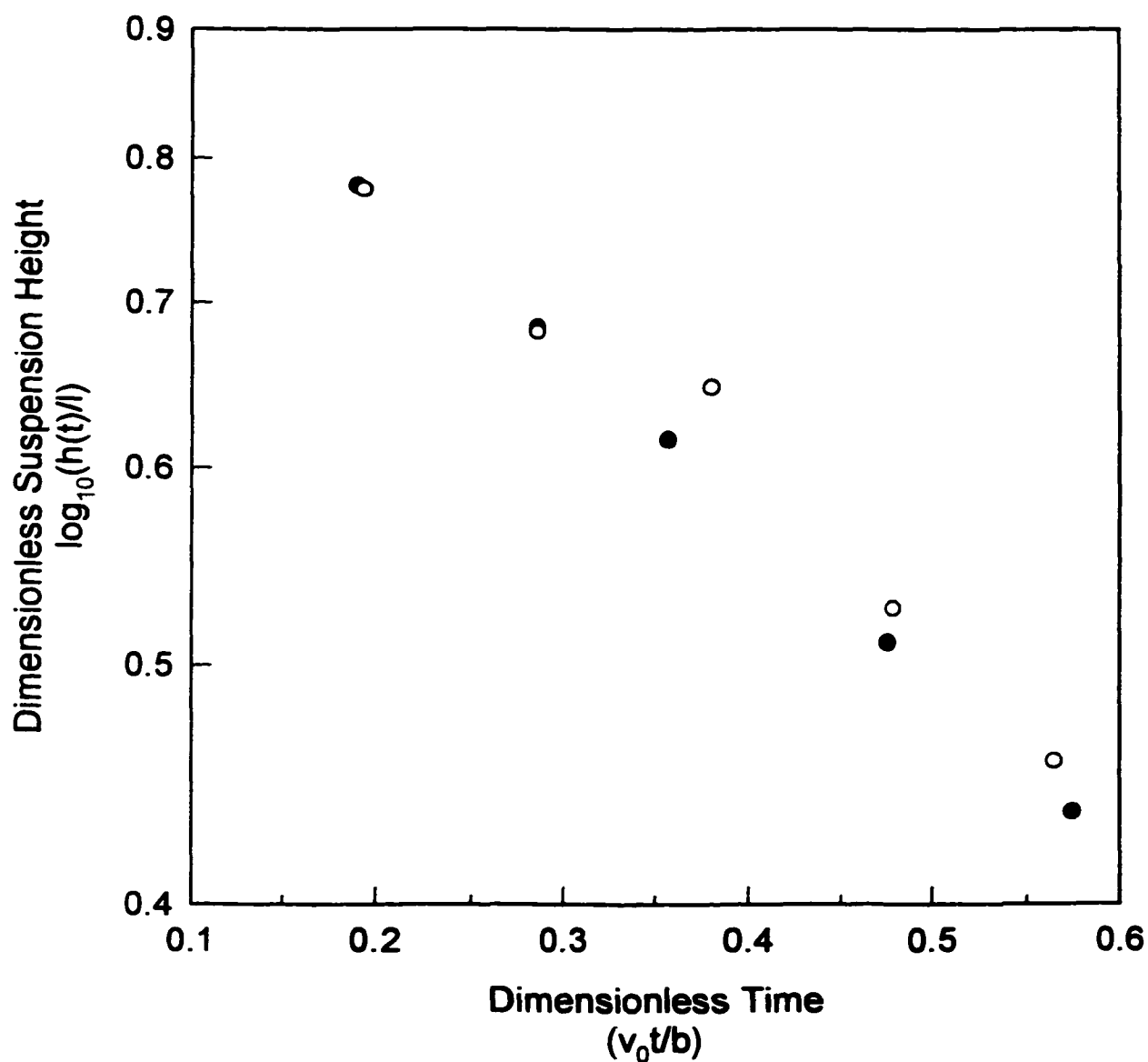
Figure 2.15: The effects of polarity switching on decantation. ●, Data from Figure 2.10 (no polarity switching), O, Data from Figure 2.12 (polarity switched every 180 minutes, $\tau \approx 0.35$). Data for $h(t)$ were taken midway between the anode and cathode for the 0.95 contour.

reversal to the characteristic time was at least 15 and no effect due to polarity switching was observed.

Finally, the decantation rate from the boundary-layer model was compared to that of the simulations. Figure 2.16 shows a plot of the bulk suspension height normalized to the electrode height as a function of dimensionless time. The solid line is the predicted rate from the boundary-layer model. The circles represent the height of the suspension for simulations where the electrodes were the top 75% of the chamber side walls (no polarity switching). These data are taken from Figure 2.10 at the midpoint between the cathode and anode. The squares depict $h(t)/l$ for the case where the electrodes were the top 95% of the chamber side walls and the remaining parameters the same as those used in Figure 2.10. The filled and open symbols are used to represent the normalized volume fractions of 0.95 and 0.05, respectively. It is evident from the simulation results presented in Figure 2.16 that the boundary-layer model is in agreement with the simulations. The boundary-layer assumes the electrodes extend to the bottom of the chamber. Figure 2.16 shows that as the amount of space below the electrodes is decreased from 25% to 5% of the vertical boundaries, better agreement is seen between the boundary-layer model and the simulation results. This suggests that the dead space below the electrodes does indeed have an influence on the rate of decantation, albeit a minor one. In Chapter 3, Future Studies, steps to identify the effect of the chamber design on electrodecantation will be discussed.

One final note, all of the two-dimensional simulations were performed on a 130 by 130 uniformly spaced grid. In the current state, the length of time required to perform
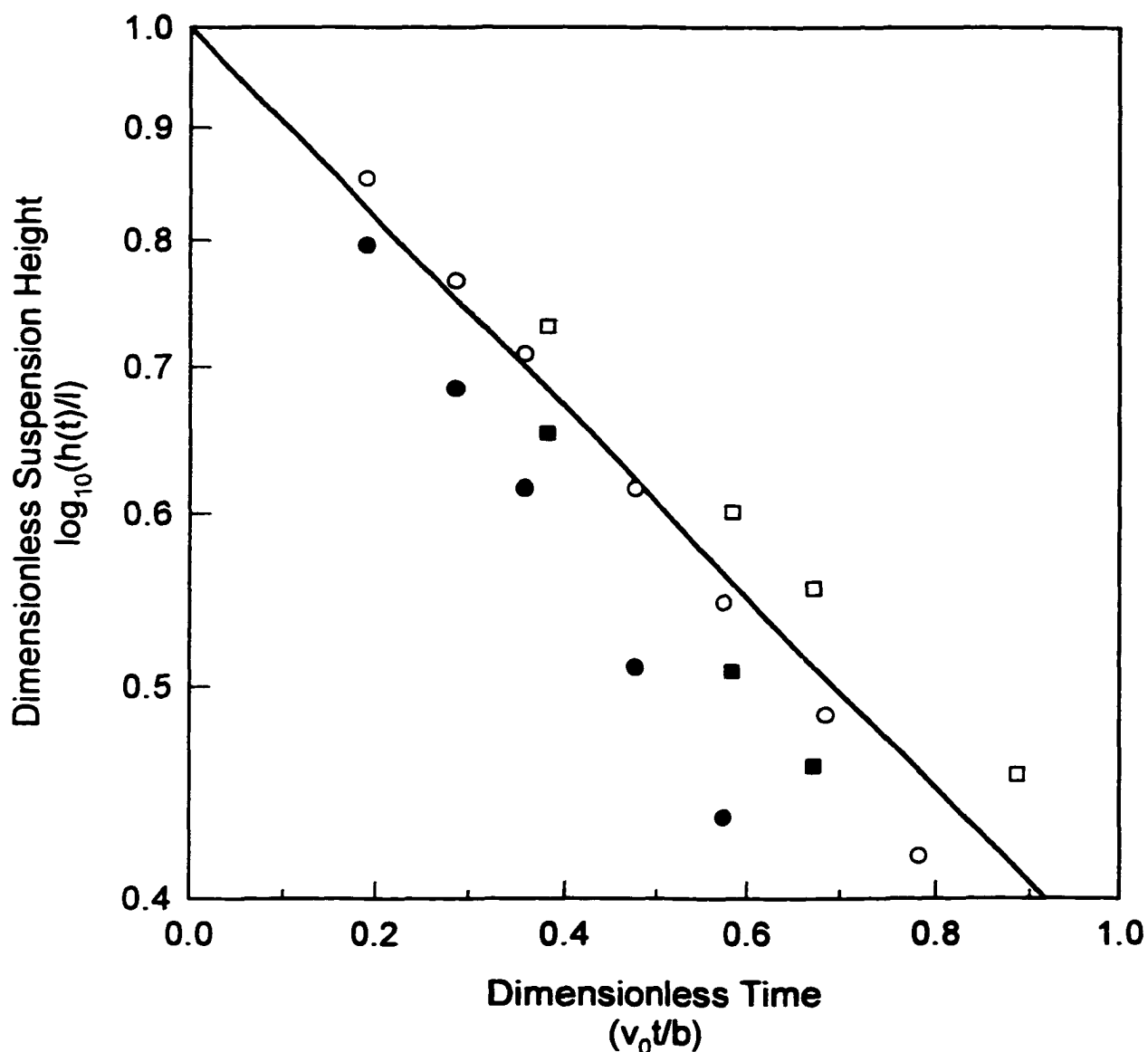
Figure 2.16: Comparison of simulation results to the boundary–layer model. The boundary–layer model prediction is given by the solid straight line. Legend: ●, Normalized volume fraction equal to 0.95 (Figure 2.4) where electrodes are 75% submerged, O. Normalized volume fraction equal to 0.05 where electrodes are 75% submerged, ■, Normalized volume fraction equal to 0.95 where electrodes are 95% submerged, □, Normalized volume fraction equal to 0.05 where electrodes are 95% submerged. All data were obtained at 0.5 dimensionless distance from the anode and remaining conditions are the same as those listed in Figure 2.10. Grid: 130 × 130.

simulations with a uniformly spaced grid of 500 by 500 or even a grid of 200 by 200 will be prohibitively long. A discussion of how this can be overcome is given in the future studies section.

2.4.4 Summary of the Two-dimensional Simulations

Two-dimensional simulations confirm the formation of a clear boundary layer and illustrate the redistribution of clear fluid onto the surface of the suspension as a result of buoyancy-driven motion. The buildup of particles at one of the electrodes and the eventual accumulation of particles on the bottom of the container are also confirmed by the simulation results. In addition, the simulations demonstrate that, as seen in experiments, the periodic reversal of the electric field polarity only has a minimal effect on the decantation rate.

The two-dimensional simulations were also used to investigate the effects of cell geometry on electrodecantation. The boundary-layer model does not account for the space below the electrodes or the space between the chamber walls and the electrodes, as was the case in the experiments. The two-dimensional simulations suggest that the distance the electrodes were submerged may modestly influence the growth rate of the clear fluid layer on the surface of the suspension. These results did not explain why the experiments revealed a slower accumulation of clear fluid than that predicted by the boundary-layer model.

2.5 One-dimensional Model of pH, Conductivity, and Concentration Variations

As discussed in section 2.3.2, experimental measurements on electrodecantation showed vertical stratification of the conductivity and pH (see Figures 2.26 and 2.27 below; also Table 3, Appendix B) in the suspension chamber. As hydrogen ions are either consumed or produced at the electrodes (equations 2.5 & 2.6), the rising fluid will redistribute the ions resulting in vertical pH and conductivity stratification. This non-uniform ion distribution will cause local variations of the electric field between the electrodes. To study, in the absence of any fluid motion, the effects of the electrode reactions, pH gradients, and conductivity gradients, one-dimensional numerical simulations were developed. To perform full two-dimensional simulations, with fluid motion, would required more computing speed than is currently accessible. An electric field of 6.0 V/cm was chosen as a representative electric field strength since experiments were performed at electric fields between 0.5 and 10 V/cm.

Determining the local electrical conductivity and pH of the suspension requires that the distribution be determined for all ions in solution. Conservation equations similar to those written for the suspended solids can be used to determine the ion distributions, viz.

$$\frac{\partial n_k}{\partial t} + \nabla \cdot \mathbf{f}_k = 0, \quad k = 1, 2, \ldots, I \tag{2.13}$$

where the flux of species k is

$$\mathbf{f}_k = -e z_k \omega_k n_k \nabla \phi - k_B T \omega_k \nabla n_k, \quad k = 1, 2, \ldots, I \tag{2.14}$$

Here n_k is the concentration, z_k is the valence and ω_k is the mobility of species k, and I is the number of ionic species present excluding H^+ and OH^-.

The approach taken in advancing the ion and suspended solids distributions forward in time is very similar to the procedure described in section 2.4 for the particle concentration. Initial ion and solids concentrations are used to calculate the pH, conductivity, and particle valence. If the number of colloidal (particulate) species is M, the local electrical conductivity is given by

$$\sigma \equiv e^2 \sum_{k=1}^{I} z_k^2 \omega_k n_k + e^2 \sum_{j=1}^{M} [(z_j^0)^2 - 2\overline{V}_j z_j^0 + \overline{V_j^2}] \omega_j c_j, \qquad (2.15)$$

where $\overline{V}_j$ is the average number of protons that are dissociated, and z_j^0 and c_j are the valence and local concentration of particulate species j, respectively. The definition for pH,

$$pH = -\log[H^+], \qquad (2.16)$$

the relationship for the dissociation of water, $K_w = [H^+][OH^-] = 10^{-14} M$, and electroneutrality,

$$0 = \sum_{k=1}^{I} z_k n_k + \sum_{j=1}^{M} z_j c_j, \qquad (2.17)$$

are the used, along with equation (2.9) and (2.15), to solve simultaneously for the suspension pH, conductivity, and particle valence. Here K_w is the dissociation constant for water, $[H^+]$ is the hydrogen ion concentration, and $[OH^-]$ is the hydroxyl ion concentration. Locally, electroneutrality may be invoked since the relevant length scales are much greater than the Debye screening length.

Invoking conservation of charge, the electric field $\mathbf{E}$ can be determined by combining the ion and particle balances; an equation for the electrical potential ϕ, results:

$$\sigma\nabla^2\phi + \nabla\sigma\cdot\nabla\phi = -\nabla\cdot\left\{ek_BT\sum_{k=1}^{I}\omega_k z_k\nabla n_k + ek_BT\sum_{j=1}^{M}\omega_j\nabla(z_jc_j)\right\} \qquad (2.18)$$

with $\mathbf{E} \equiv -\nabla\phi$. The elliptic equation solver is not required to resolve the electric field since the simulation is one-dimensional and simple central differences can be employed where needed. To determine the one-dimensional solids and ion distributions at the new time, the numerical integration of equations (2.7) and (2.13) for each component requires that the unsteady fluxes in equations (2.8) and (2.14) be calculated. The divergence of the fluxes are again determined using a second order central differencing scheme. A no flux condition is prescribed at the boundaries for the suspended solids and ions, except H^+ and OH^-. The boundary conditions on the fluxes of H^+ and OH^- must satisfy the charge balance. To satisfy the conservation of charge requirement, the flux of H^+ and OH^- must provide a current, which is consistent with the reactions given in equations (2.5) and (2.6).

It should be noted that Mosher et al. (1992) have discussed these balance laws in more detail, describing diffusion, electromigration, and convection of solutes in electrophoretic separations. The balance laws are summarized by Baygents et al. (1997) and include dissociation-association equilibria needed to describe amphoteric compounds, weak bases, and weak acids. The conservation and equilibrium equations for ampholytes, weak bases, and weak acids have not been reproduced here since the

ionogenic species present in the current study are treated as fully-dissociated (except for

$H_2O \leftrightarrow H^+ + OH^-$.

As before, the PLPE-FCT algorithm is used in the integration of equations (2.7) and (2.13). This flux-limiter was developed by Boris and Book (1976) to solve general unsteady advection-dominated (hyperbolic) equations and is used here to suppress numerical oscillations that may result from sharp concentration and pH gradients that arise since Pe_e is $O(10^6)$. The size of the time step used is determined by the stability limit described in equation (2.12).

After the concentration profiles of all the species are determined at the new time, the process is repeated, i.e. the pH, conductivity, particle valence, and electric field are recalculated for the new time step. The fluxes are once again determined and the process advanced explicitly forward in time to determine the new ion and suspended particle distributions. Table 2.3 provides a summary of the procedure used to advance the concentration and ion distributions forward in time.

2.5.1 Particle Migration Away from the Electrode

Figures 2.17-2.20 illustrate the case for low-conductivity media at $E = 6.0$ V/cm; electric fields on the order of 1 to 10 V/cm were used in experiments. Figure 2.17a shows that, in the absence of any fluid motion, suspended silica particles accumulate at one of the electrodes, as would be expected. Figure 2.17a also shows that silica particles are being electrophoretically pushed away from the cathode. After 15 seconds, the concentration at the boundary has decreased to nearly zero, and a particle-

Figure 2.17a: One-dimensional simulation of the accumulation and depletion of silica solids at the electrodes using an initial uniform electric field of 6.0 V/cm, conductivity of 16.5 μS/cm, and pH = 4.4. Initial silica concentration = 5×10^{-10} M, 4×10^{-5} M HNO$_3$ added to adjust pH, Nodes = 1001. Anode on left boundary.

Figure 2.17b: One–dimensional simulation of the accumulation and depletion of NO₃⁻ ions at the electrodes using an initial uniform electric field of 6.0 V/cm, conductivity of 16.5 μS/cm, and pH = 4.4. Initial silica concentration = 5×10^{-10} M, 4×10^{-5} M HNO₃ added to adjust pH, Nodes = 1001. Anode on left boundary.

Figure 2.18: Electric field strength. Initial experimental conditions: conductivity of 16.5 μS/cm, and pH = 4.4. Initial silica concentration = 5×10^{-10} M, 4×10^{-5} M HNO$_3$ added to adjust pH, Nodes = 1001. Anode on left boundary.

Figure 2.19: One–dimensional simulation of the pH distribution using an initial uniform electric field of 6.0 V/cm, conductivity of 16.5 μS/cm, and pH = 4.4. Initial silica concentration = 5×10^{-10} M, 4×10^{-5} M HNO$_3$ added to adjust pH, Nodes = 1001. Anode on left boundary.

Figure 2.20: One–dimensional simulation of the electrical conductivity distribution at an initial uniform electric field of 6.0 V/cm, conductivity of 16.5 μS/cm, and pH = 4.4. Initial silica concentration = 5×10^{-10} M, 4×10^{-5} M HNO$_3$ added to adjust pH, Nodes = 1001. Anode on left boundary.

depleted boundary layer has formed. Were fluid motion included, a buoyancy-driven flow up the surface of the electrode would develop (see section 2.3). Figure 2.17a also shows an accumulation of particles adjacent to the particle-depleted boundary layer. This stems from an increase in the electric field in the boundary layer where particles (Figure 2.17a) and NO_3^- ions (Figure 2.17b) have been removed. The electric field strength is given in Figure 2.18. As the particles and ions are electrophoretically pushed away from the cathode, the local conductivity is diminished and the electric field increases, causing an increase in the electrophoretic velocity of the remaining particles; particles accumulate in the adjacent suspension as a result. Figures 2.18 to 2.20 provide a self-consistent picture of these results.

Another set of experiments was performed to investigate the effects of ionic strength on clear fluid boundary layer formation. Silica suspensions at ionic strengths around 250 μS/cm did not develop a clear fluid layer on the surface, even though electrodecantation was controlling the separation process. Figure 2.21 provides the results of a one-dimensional simulation on a silica suspension at 250 μS/cm. A comparison between Figures 2.17a and 2.21 shows that for comparable field strength experiments, a particle-free boundary layer will develop at the cathode in approximately 10 seconds in low conductivity suspensions (16.5 μS/cm), but even after 4 minutes, a particle-free boundary layer had not yet formed in the 250 μS/cm suspension. This is a consequence of ions building up at the electrodes, increasing the local conductivity (Figure 2.22 and 2.23), resulting in a decreased electric field (Figure 2.24). The
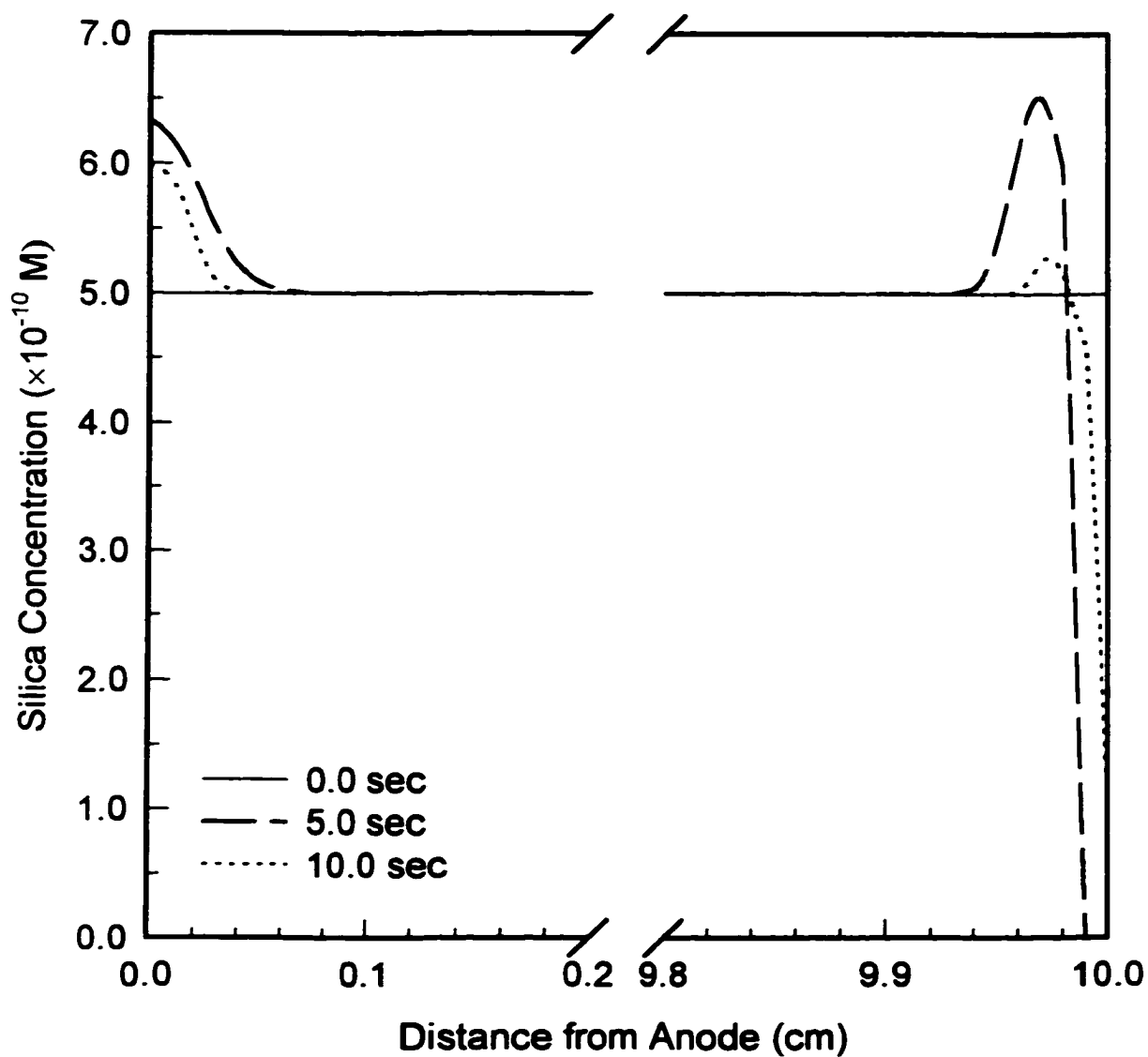
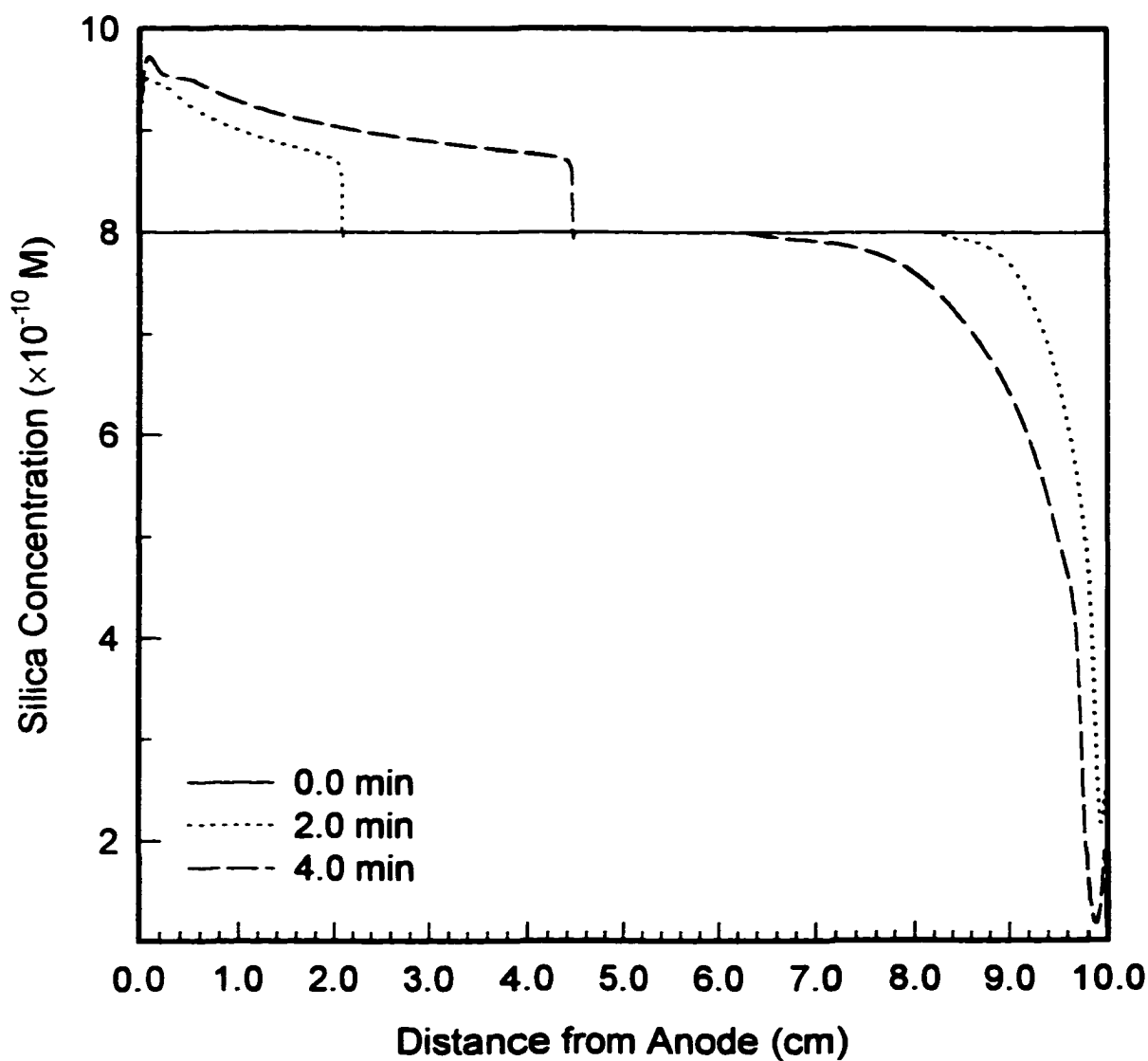
Figure 2.21: One-dimensional simulation of the accumulation and depletion of silica solids at an initial uniform electric field of 6.0 V/cm, conductivity of 250 μS/cm, and pH = 9.3. Initial silica concentration = 8×10^{-10} M, 1.95×10^{-3} M HNO_3 & 1.97×10^{-3} M KOH added to adjust pH and conductivity, Nodes = 2001. Anode on left boundary.
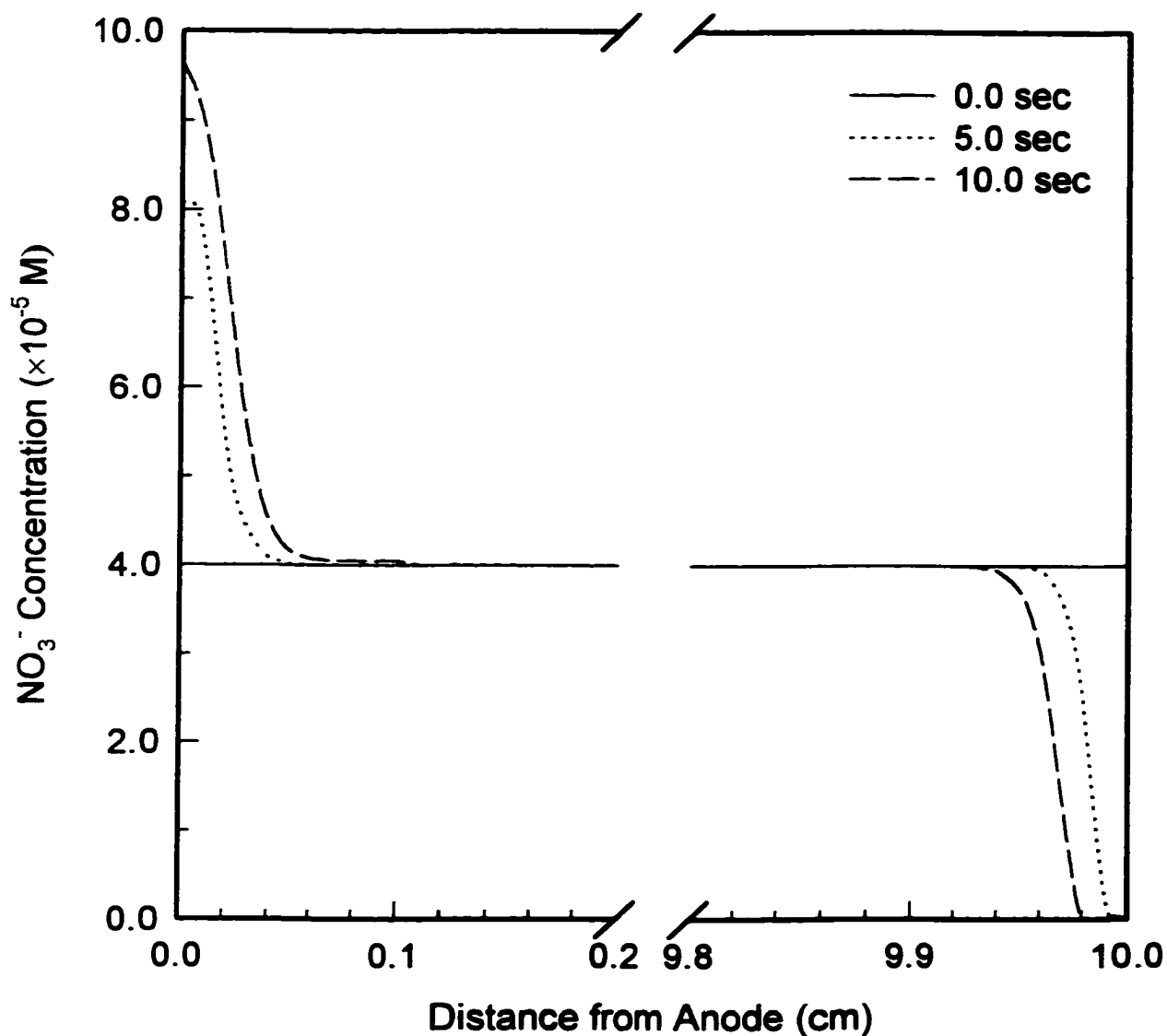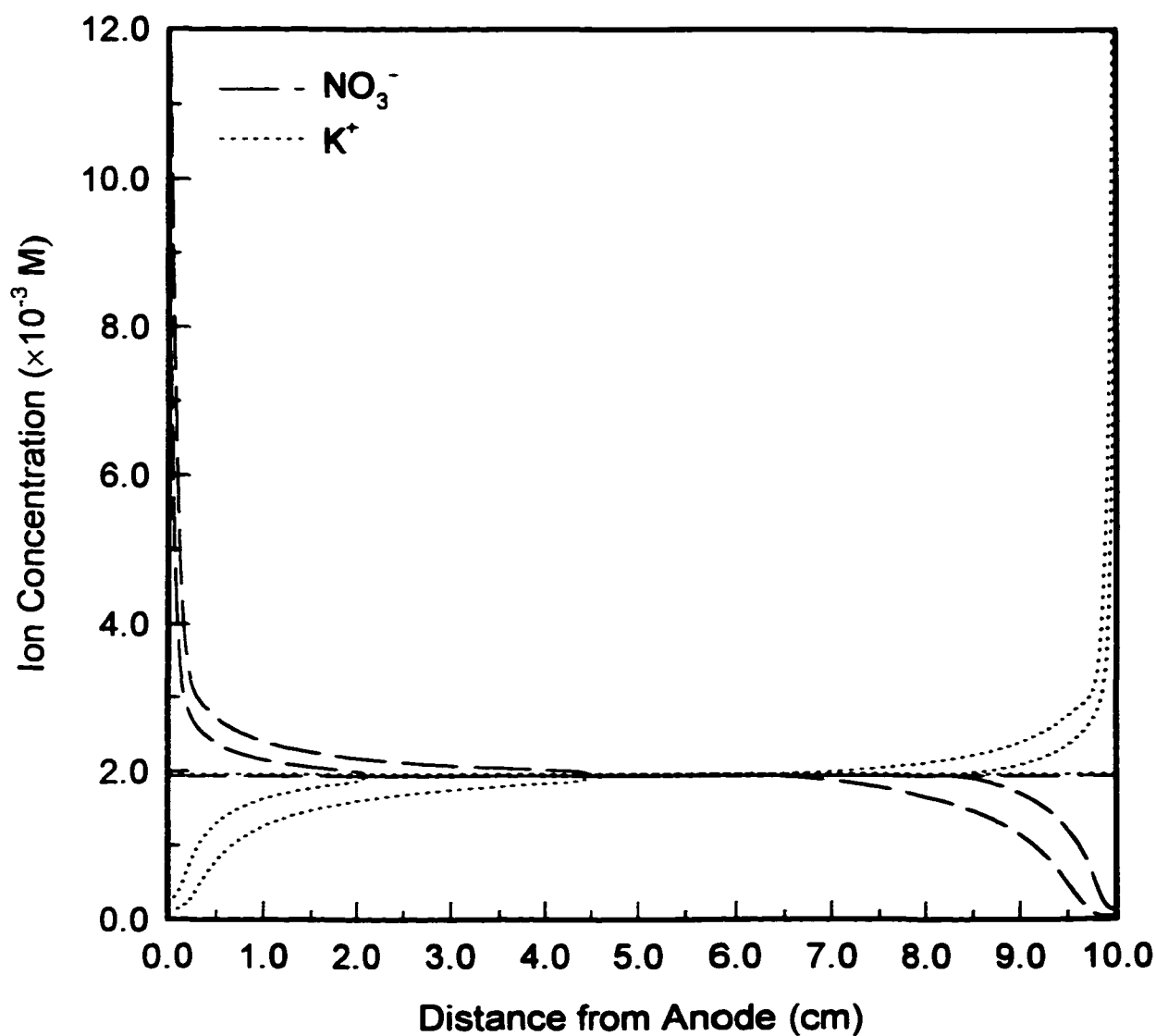
Figure 2.22: One–dimensional simulation of the accumulation and depletion of KNO_3 ions at an initial uniform electric field of 6.0 V/cm, conductivity of 250 μS/cm, and pH = 9.3. Initial silica concentration = 8×10^{-10} M, 1.95×10^{-3} M HNO_3 & 1.97×10^{-3} M KOH added to adjust pH and conductivity, Nodes = 2001. Each line represents 2.0 minute intervals starting at time equal to zero. Anode on left boundary.
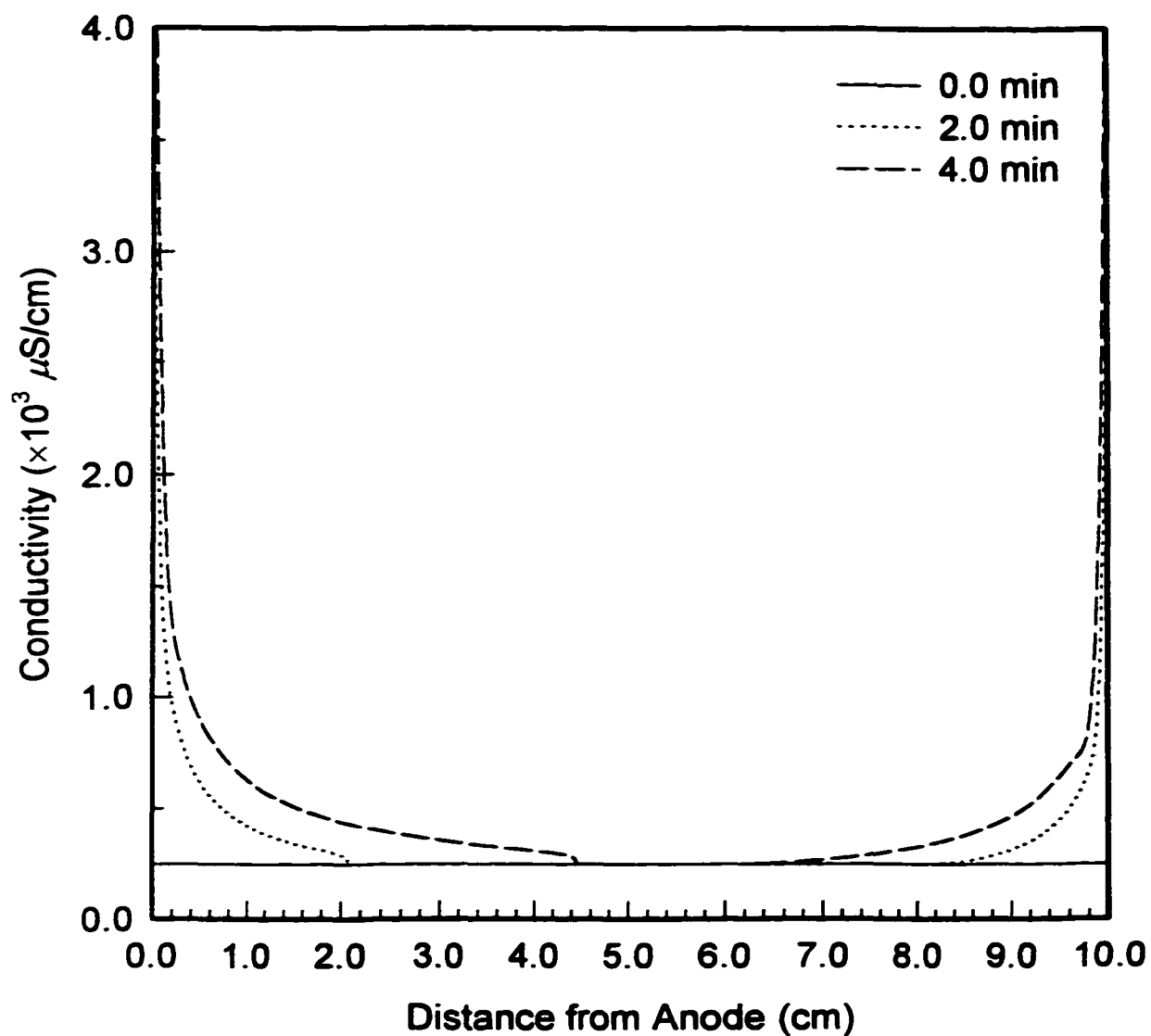
Figure 2.23: One–dimensional simulation of the electrical conductivity distribution at an initial uniform electric field of 6.0 V/cm, conductivity of 250 μS/cm, and pH = 9.3. Initial silica concentration = 8×10^{-10} M, 1.95×10^{-3} M HNO_3 & 1.97×10^{-3} M KOH added to adjust pH and conductivity, Nodes = 2001. Anode on left boundary.
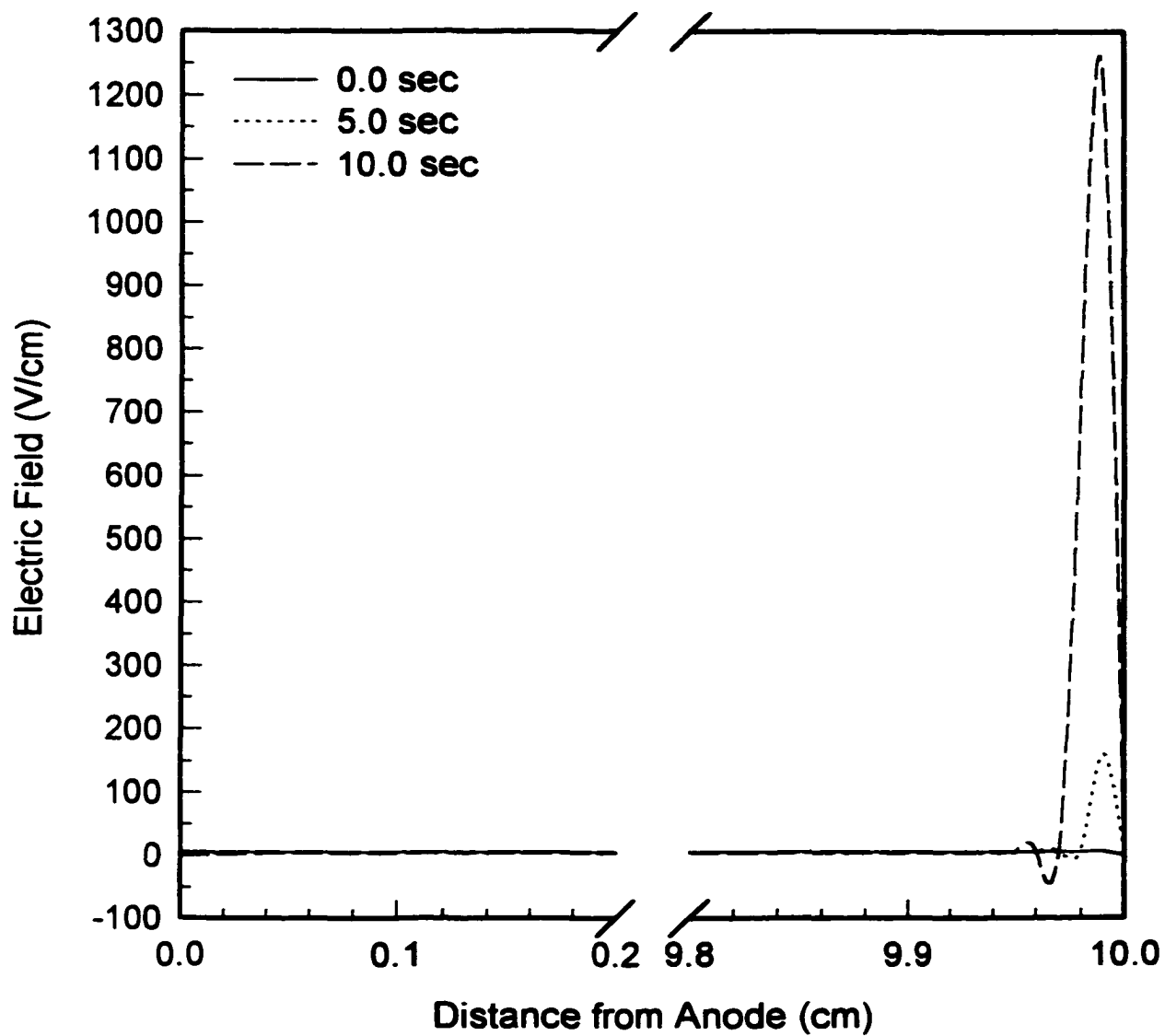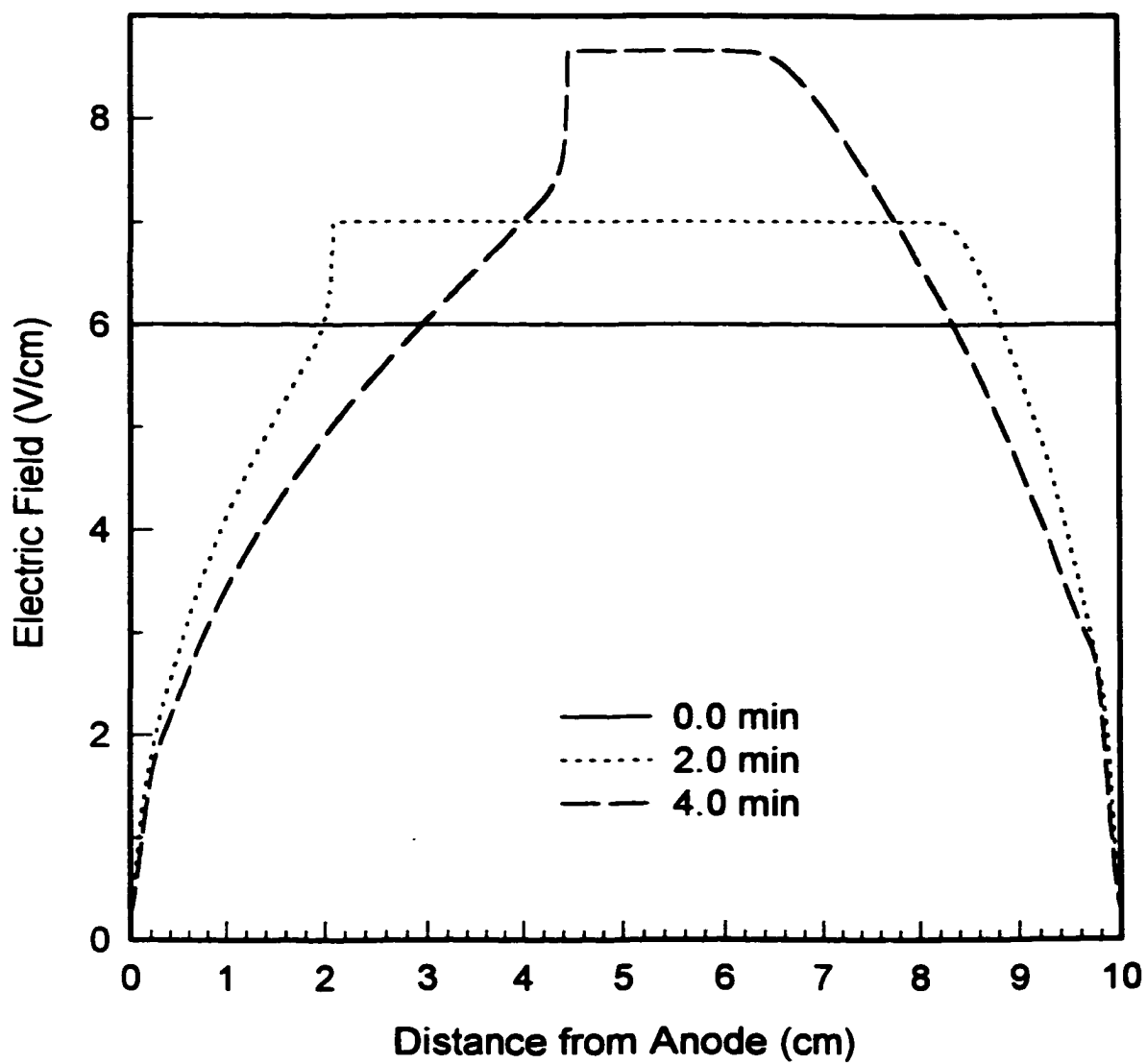
Figure 2.24: Electric field strength. Initial experimental conditions: conductivity of 16.5 μS/cm, and pH = 4.4. Initial silica concentration = 5×10^{-10} M, 4×10^{-5} M HNO$_3$ added to adjust pH, Nodes = 2001. Anode on left boundary.

decreased electric field strength causes the silica particles to electrophoretically migrate at a slower rate; giving rise to a slowly developing clear fluid boundary layer.

Since the particle concentration has decreased in the region next to the cathode, a buoyancy force will still result, causing suspension to rise along the cathode toward the surface; while this suspension has a diminished volume fraction of particles, it is not void of particles. This will result in a reduced concentration of particles at the surface, though a clear fluid layer will not develop. Results for the ion, conductivity, and pH distributions are provided in Figures 2.22, 2.23, and 2.25, respectively.

2.5.2 pH Variations

Figure 2.19 shows the pH changes for the simulation in section 2.5.1 at an initial electric field of 6.0 V/cm. Due to reactions at the electrodes (Equations 2.5 and 2.6), pH gradients develop adjacent to the electrodes. Since silica particles electrophoretically migrate away from the cathode, the resulting upward convection will carry higher pH fluid to the surface while lower pH suspension is driven to the bottom. Conversely, for positively charged particles, such as alumina, the particle-depleted layer will form next to the anode, causing the lower pH fluid to rise to the surface. These results are consistent with measurements conducted at the completion of electrodecantation experiments (Figure 2.26 and Table 3, Appendix B).
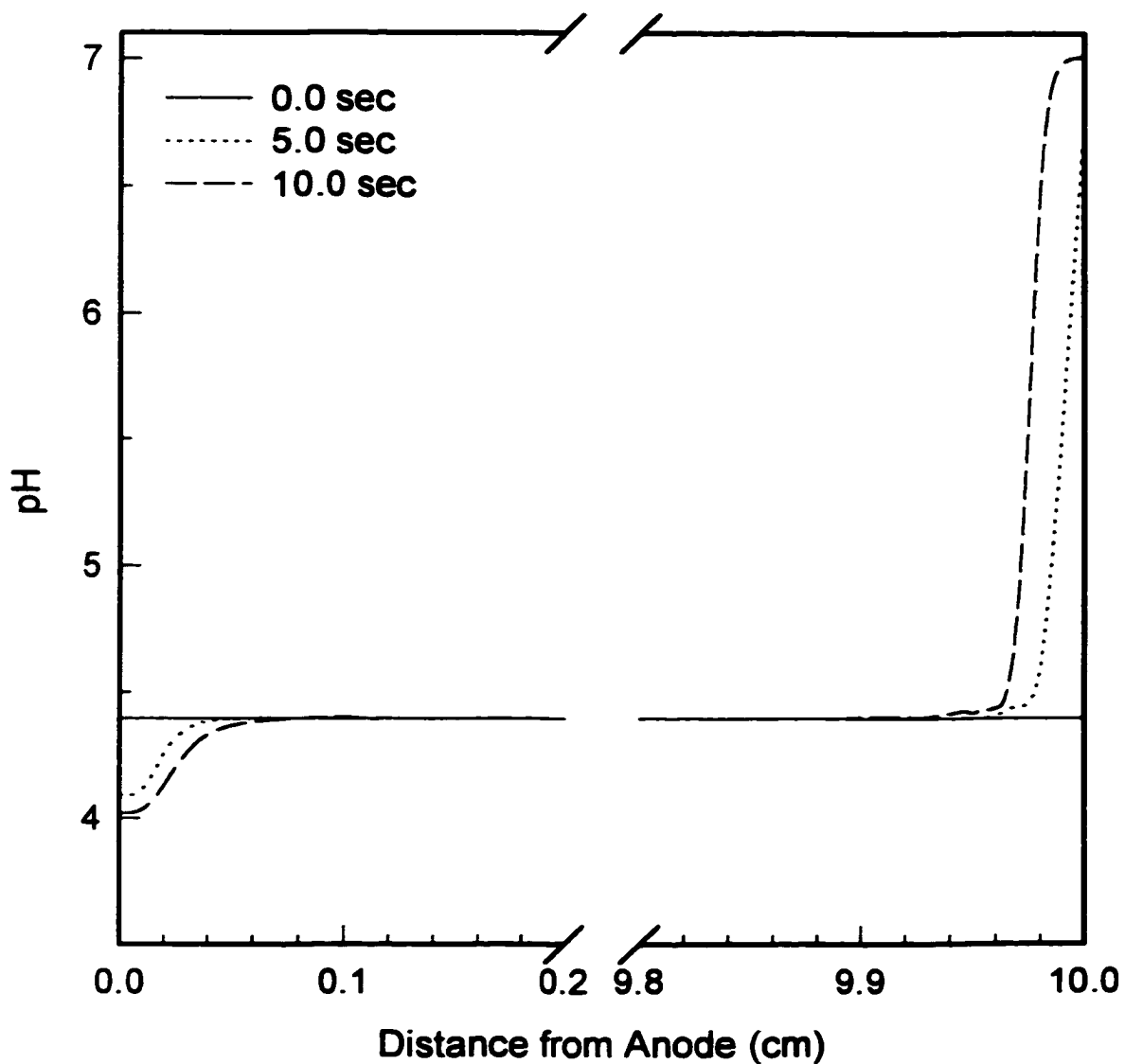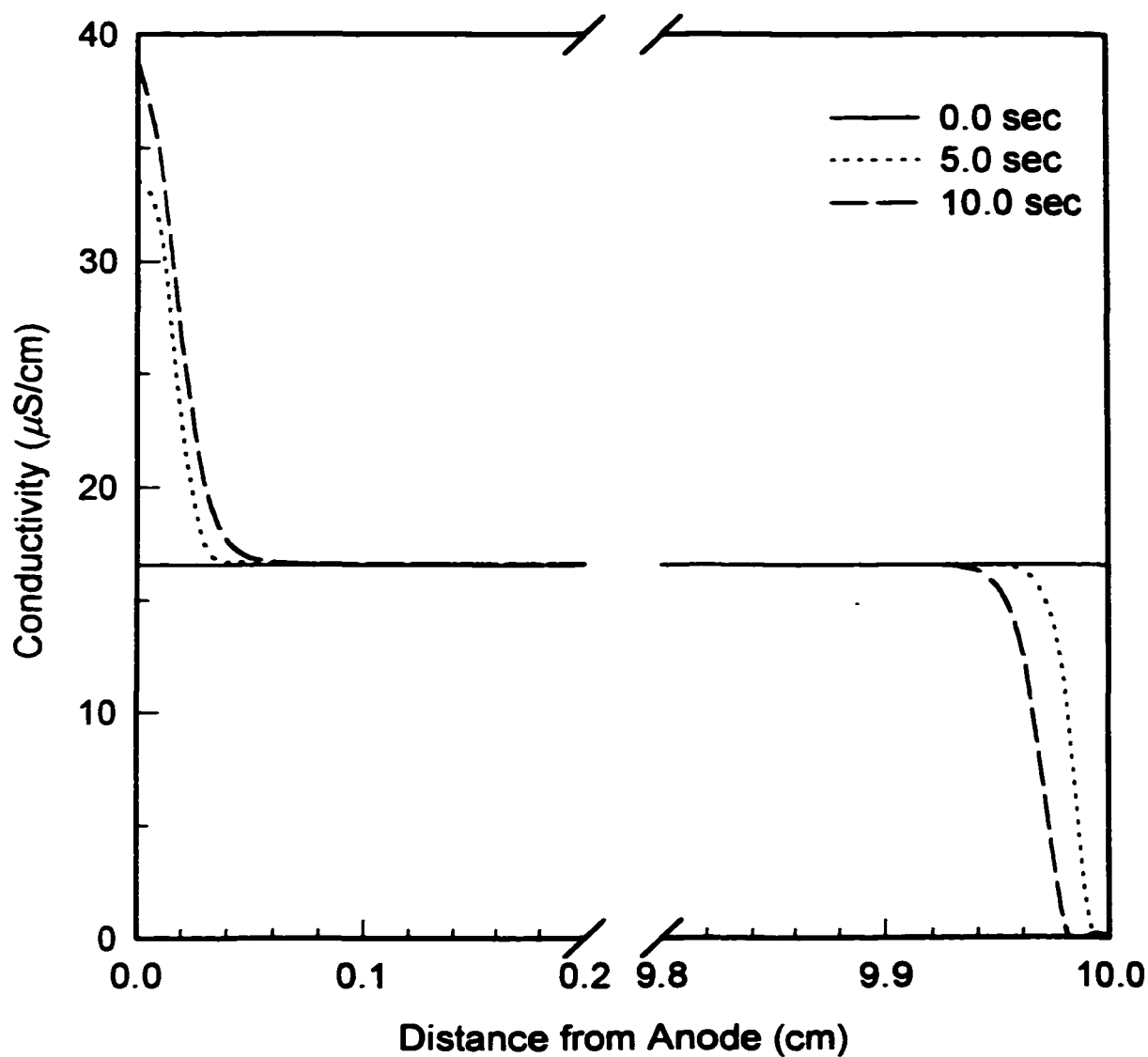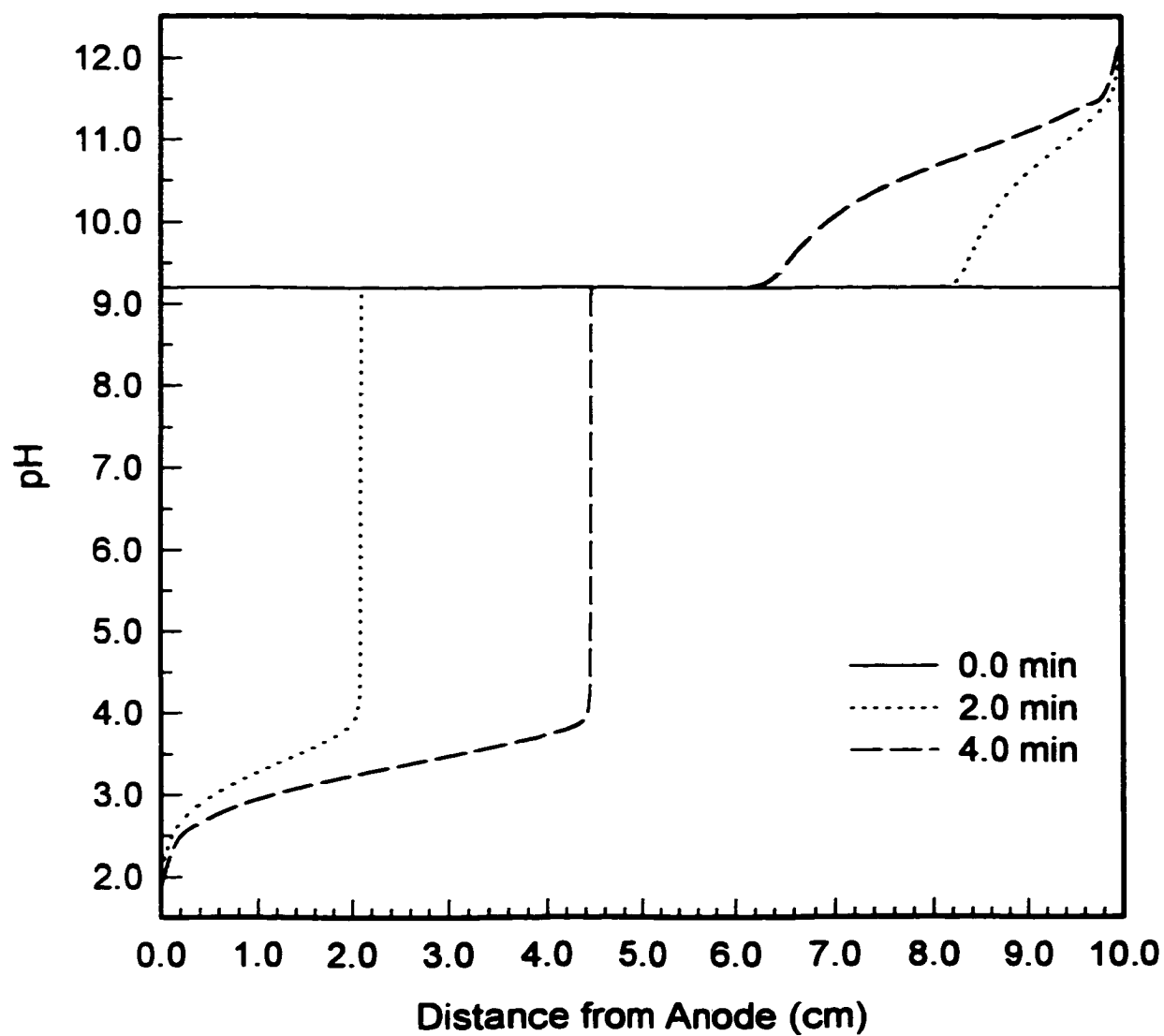
Figure 2.25: One–dimensional simulation of the pH distribution at an initial uniform electric field of 6.0 V/cm, conductivity of 250 μS/cm, and pH = 9.3. Initial silica concentration = 8×10^{-10} M, 1.95×10^{-3} M HNO$_3$ & 1.97×10^{-3} M KOH added to adjust pH and conductivity, Nodes = 2001. Anode on left boundary.
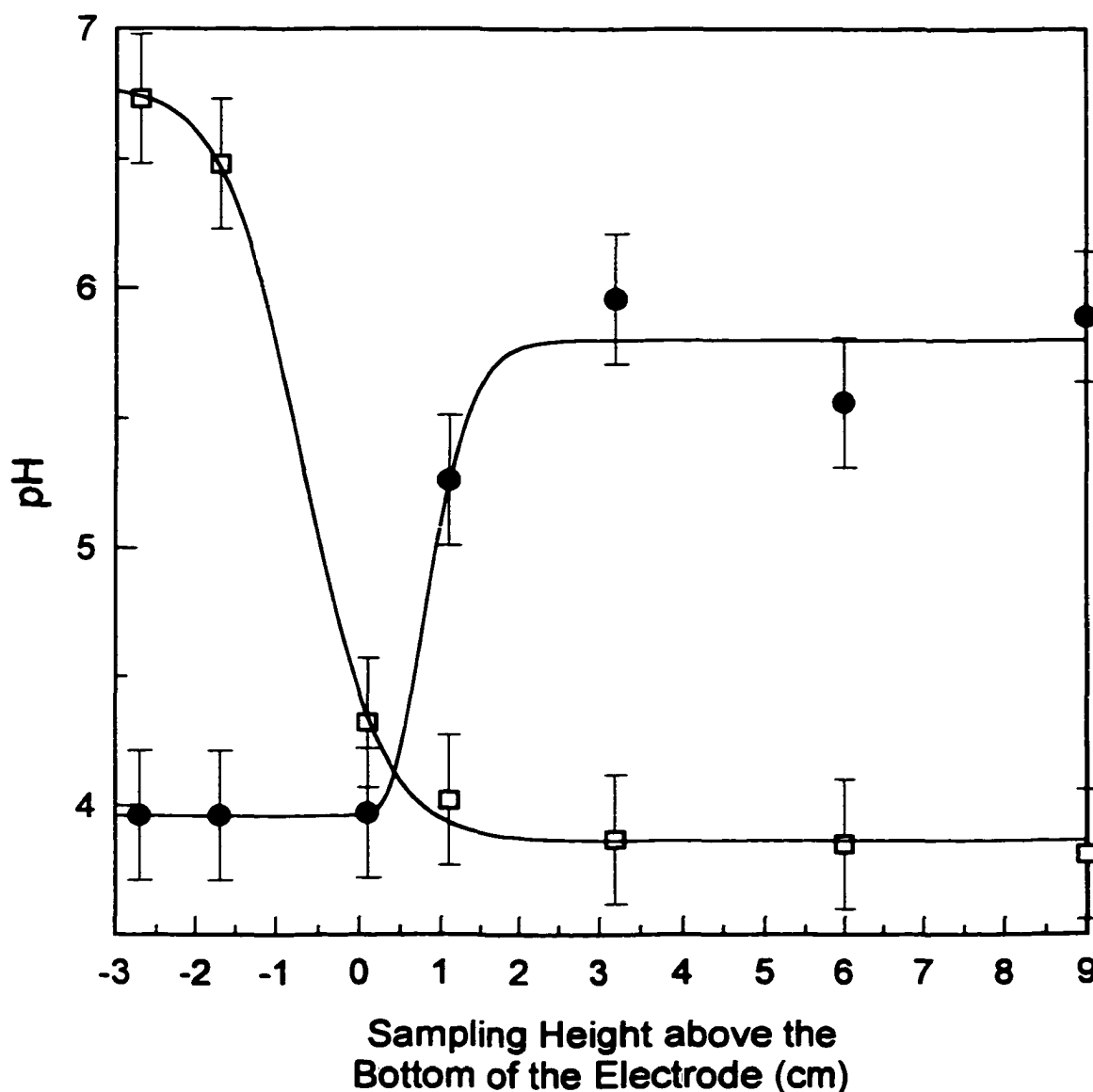
Figure 2.26: Stratification of pH. ●, Silica particles, Electrodecantation after 7 hours, E = 7.3 V/cm, polarity switched every 30 minutes, $c_0 = 2.3 \times 10^{-3}$, $\sigma_0 = 5.7$ μS/cm, and initial pH = 4.4. □, Alumina particles, Electrodecantation after 8.5 hours, E = 3.6 V/cm, polarity switched every 30 minutes, $c_0 = 1.3 \times 10^{-3}$, $\sigma_0 = 15.5$ μS/cm, and initial pH = 4.2. The lines are fit to the data to assist the reader and the clear fluid surface layer is approximately 1.0 cm above the bottom of the electrodes.

2.5.3 Conductivity Variations

As the hydrogen ion concentration is increased at the anode, the conductivity of the layer of fluid adjacent to the electrode will increase, while at the cathode, the conductivity will decrease as hydrogen is removed. Because the mobility of hydrogen ions is high $(36.25 \times 10^{-4}\ cm^2/V \cdot s)$ and the ionic strength is low, these local alterations of the electrical conductivity are substantial. Results from the numerical simulation at 6.0 V/cm, shown in Figure 2.20, illustrate the formation of conductivity gradients during treatment of silica suspensions. For the results presented in Figure 2.20, 85 to 90% of the local conductivity can be attributed to the hydrogen ions, with the remainder attributed to the NO_3^- ions. The current carried by the silica particles is negligible. As a result of the depletion of the silica particles near the cathode (Figure 2.17a), lower conductivity fluid will rise to the surface.

The calculations for the conductivity and pH support the postulate that electrodecantation couples with the electrode reactions to redistribute and stratify the ionic solutes. Experimental data presented in Figure 2.27 (see also Table 3, Appendix B) show that, for silica suspensions, low-conductivity fluid has been convected to the surface, while high-conductivity fluid has been driven to the bottom of the chamber. The opposite effect is observed in alumina suspensions: buoyancy effects force higher conductivity fluid to the surface.
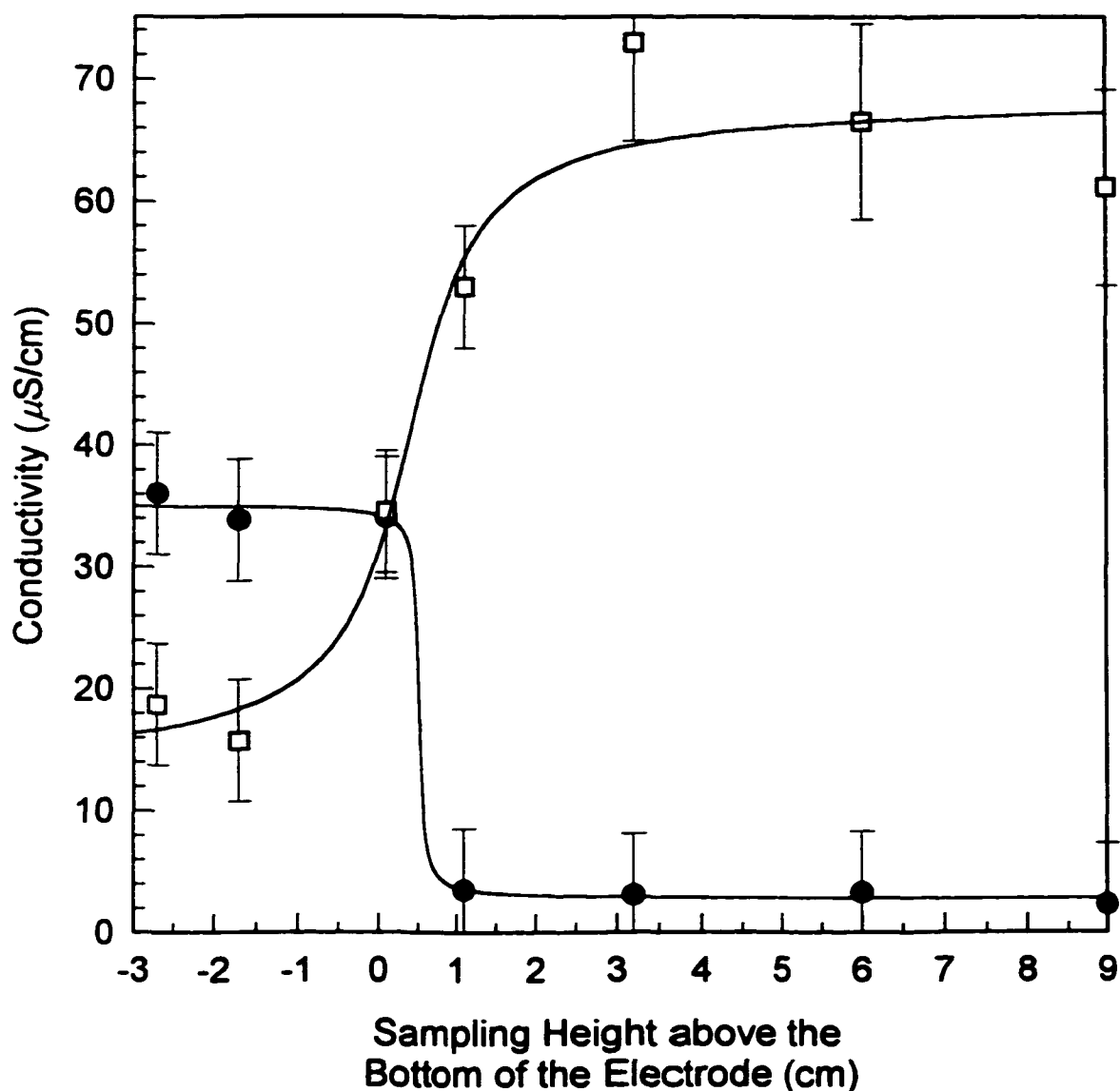
Figure 2.27: Stratification of electrical conductivity. •, Silica particles, Length of electrodecantation = 7 hours, E = 7.3 V/cm, polarity switched every 30 minutes, c_0 = 2.3×10^{-3}, σ_0 = 5.7 μS/cm, and initial pH = 4.4. □, Alumina particles, Length of electrodecantation = 8.5 hours, E = 3.6 V/cm, polarity switched every 30 minutes, c_0 = 1.3×10^{-3}, σ_0 = 15.5 μS/cm, and initial pH = 4.2. The lines are fit to the data to assist the reader and the clear fluid surface layer is approximately 1.0 cm above the bottom of the electrodes.

2.5.4 Summary of One-dimensional Simulations

To study the development of pH and conductivity gradients in the absence of fluid motion, one-dimensional simulations were performed. Taking into account the electrode reactions, one-dimensional simulation results indicated pH and conductivity gradients at the surface of the electrodes. The resulting pH and conductivity changes produced during the numerical simulations were found to be in agreement with pH and conductivity gradients measured at the completion of experiments.

One-dimensional simulations on high (250 μS/cm) and low-conductivity ($<$ 20 μS/cm) suspensions were compared. The simulations show that in high-conductivity suspensions a particle free layer fails to develop next to the cathode, in contrast to low-conductivity suspensions where a clear boundary layer forms. This results in particle depleted suspension (but not particle-free fluid) being mapped onto the surface and the formation of a particle-depleted layer but not a clear fluid layer being formed on the surface of the suspension.

2.6 Summary of Modeling versus Experiments

In summary, numerical simulations were an important tool in explaining experimental observations and verifying boundary-layer model predictions. The two-dimensional simulations confirm the formation of a clear boundary layer and illustrate the redistribution of clear fluid onto the surface of the suspension as a result of buoyancy-driven motion. The buildup of particles at one of the electrodes and the eventual accumulation of particles on the bottom of the container are also confirmed by the

simulation results. In addition, the simulations demonstrate that, as seen in experiments, the periodic reversal of the electric field polarity only has a minimal effect on the decantation rate.

The two-dimensional simulations were also used to investigate the effects of cell geometry on electrodecantation. The boundary-layer model does not account for the space below the electrodes or the space between the chamber walls and the electrodes, as was the case in the experiments. The two-dimensional simulations suggest that the distance the electrodes were submerged may influence the growth rate of the clear fluid layer on the surface of the suspension. However, these results did not explain why the experimental results had a slower accumulation of clear fluid than that predicted by the boundary-layer model. Further research needs to be completed to determine the effects of the area between the chamber walls and the electrodes and to completely understand the effects of the area beneath the electrodes (see Chapter 3, Future Studies).

Numerical simulations may explain the experimental observation that a narrow transition zone between clear fluid and the bulk suspension develops. This is in direct contrast to the boundary-layer model predictions which state that a sharp transition will occur between the clear fluid and bulk suspension if the boundary layer is stable. Further studies are required to establish if numerical convergence was achieved before any conclusions can be made regarding the transition zone.

To explain pH and conductivity gradients observed during experiments, one-dimensional simulations were performed. Taking into account the electrode reactions, these simulation results indicated pH and conductivity gradients at the surface of the

electrodes. These pH and conductivity changes will be convected to the surface or bottom of the chamber by the attending fluid motion. The pH and conductivity changes measured at the completion of experiments were in agreement with those predicted by the simulations.

Finally, to help explain why a clear fluid layer failed to develop during experiments on high conductivity silica suspensions, one-dimensional simulations on high (250 μS/cm) and low-conductivity (< 20 μS/cm) suspensions were compared. The simulations show that in high-conductivity suspensions a particle free layer fails to develop next to the cathode, in contrast to low-conductivity suspensions where a clear boundary layer forms. This results in particle depleted suspension (but not particle-free fluid) being mapped onto the surface and the formation of a particle-depleted layer but not a clear fluid layer being formed on the surface of the suspension.

2.7 Characterization of Particles in Suspension

Two techniques were developed to characterize the important properties of suspended particles. Taylor-Aris dispersion measurements and capillary electrophoresis experiments were used to determine diffusion coefficients, particle sizes, and electrophoretic mobilities of the particles in suspension.

2.7.1 Taylor-Aris Measurements

A Beckman P/ACE 2100 capillary electrophoresis system was used to carry out Taylor-Aris dispersion experiments (see Fig. 1 Appendix C). A small volume of dilute

analyte suspension, containing either microspheres or tobacco mosaic virus, was injected

into a narrow bore capillary. Preparation and characterization of samples and capillaries

is described in Appendix C. By imposing a pressure drop across the capillary, the sample

plug was driven down the capillary past an UV detector and the changes in absorbance

recorded. The spatio-temporal distribution of the solute was then fit with a Gaussian

curve, and from the equation parameters, the first and second moments determined. The

diffusion coefficient was then extracted from the first and second moments (Alizadeh, et.

al., 1980).

Taylor-Aris dispersion measurements of a slug of sample traversing down a

narrow bore capillary were shown to yield accurate measurements of diffusion

coefficients for particles less than 0.3 μm in diameter. Experiments on rod-shaped

Tobacco Mosaic Virus (TMV) and hydrophilic polystyrene spheres in uncoated and

coated fused-silica capillaries yielded diffusion coefficients to within 5% of benchmark

values (results presented in Appendix C). Benchmark values for TMV were provided by

the supplier, and the benchmarks for the spheres were obtained from photon correlation

spectroscopy measurements. As a reasonable indicator for when the dispersion data

would yield accurate diffusivities, the shape of the elution profiles were required to be

Gaussian. This constraint did not suffice as the sole determinant of when Taylor-Aris

theory could be used to interpret the dispersion data. An additional constraint that

$\Delta t_R / \sigma$ be less than unity, where Δt_R is the difference between the mean residence times

of the particles and some tracer solute and σ is the standard deviation in the particle

residence time, is required. The particle elution profiles measured when $\Delta t_R / \sigma$

approached or exceeded unity where not adequately interpreted using classical Taylor-Aris theory.

2.7.2 Capillary Electrophoresis Measurements of Electrophoretic Mobility

Dilute samples of bacteria or microspheres (preparation described in Appendix D) were injected into a narrow bore capillary using a P/ACE capillary electrophoresis device. An electric field was applied down the axis of the capillary, causing samples to migrate past an UV detector. The analytes were transported down the capillary by two mechanisms: electrophoresis and electroosmosis. Electrophoresis stems from the native charge on the analyte particles, while electroosmosis involves the bulk motion of the electrolyte in which the particles are immersed. The electroosmosis rate was measured by doping the sample with a neutral solute marker, mesityl oxide, which moves with the bulk fluid. The change in absorbance was recorded as the analyte and neutral marker passed a UV detector. The difference between the measured translation rate of the sample and that of the neutral marker was then used to determine the electrophoretic mobility of the particles.

Capillary electrophoresis was shown to be an accurate and feasible way to determine electrophoretic mobilities of colloids (Appendix D). Capillary electrophoresis measurements were performed on three different strains of bacteria and three chemically distinct microspheres. The electrophoretic mobilities determined using capillary electrophoresis were in good agreement with electrophoretic mobilities determined by microelectrophoresis. The standard deviations of the electrophoretic mobilities

determined by capillary electrophoresis were typically 2 to 10 times smaller than comparable measurements by microelectrophoresis. In addition, capillary electrophoresis provided a means of resolving multimodal behavior found in some of the bacterial and microsphere samples. Mobility measurements with microelectrophoresis did not resolve the multimodal characteristics.

2.8 Nomenclature

Variable	Definition
a_p	particle radius, m
A	aspect ratio of the separation chamber
b	distance between electrodes, m
c	local concentration of suspended particles (e.g. local volume fraction)
c_0	initial concentration of suspended particles (e.g. initial volume fraction)
D	diffusion coefficient, m^2/s
e	charge of a proton, 1.6×10^{-19} C
E	electric field, V/m
f	flux of species, s^{-1}
g	gravitational constant, 9.8 m/s^2
h	height of suspension above the bottom of the electrodes, m
I	number of ionic components
k_B	Boltzmann constant, 1.381×10^{-23} J/K
l	height of electrodes, m

M	number of suspended colloidal species (particles)
M_E	electrophoretic mobility, $m^2/V \cdot s$
n	concentration of ionic species, mol/L
P	dimensionless dynamic pressure
t	time, s
T	temperature, K
u	dimensionless velocity
u_{max}	maximum dimensionless velocity
u_x	dimensionless x-component of the velocity
u_y	dimensionless y-component of the velocity
v	suspension velocity, m/s
v_0	characteristic velocity, m/s
v_e	electrophoretic velocity, m/s
x	horizontal coordinate
X	dimensionless x-coordinate
y	vertical coordinate
Y	dimensionless y-coordinate
z	valence of species
ϕ	electrical potential, V
Φ	normalized local volume fraction of suspended particles

κ	Debye screening parameter, m^{-1}
μ_0	suspension viscosity, $kg/m \cdot s$
ν_0	suspension kinematic viscosity, m^2/s
ρ_0	suspension density, kg/m^3
ρ_p	particle density, kg/m^3
ρ_f	fluid density, kg/m^3
σ	local conductivity, S/m
τ	dimensionless time
ω	mobility, $m/(N \cdot s)$
Ψ	dimensionless stream function
Co	Courant number
Gr	Grashof number
Pe_c	cell Peclet number
Pe_e	electric Peclet number
Pe_p	particle Peclet number
Re	Reynolds number
Re_p	particle Reynolds number

3.0 FUTURE STUDIES

The purpose of this dissertation is to delineate physical and chemical phenomena that substantively influence electrically-assisted separation of colloids from stable suspensions. Two distinct separation mechanisms, electrodecantation and electro-coagulation, were found to occur in different situations. The work presented here has focused primarily on electrodecantation. Even so, some questions regarding the fundamentals of electrodecantation remain unanswered and further studies are needed to clarify other points.

The existing chamber was designed to test the feasibility of using electric fields to destabilize colloidal suspensions and to provide visual insight into the clarification of suspensions. To more fairly compare theoretical predictions to experimental results, a new electrodecantation chamber needs to be developed. The first change that needs to be implemented is to replace the wire mesh electrodes with solid, flat plates. This will eliminate local non-uniformities in the electric field caused by the wire grid, as well as difficulties with the no-slip boundary conditions applied to the motion of the suspension. The use of inert electrodes should also be considered to ensure that metal ions are not being produced at the electrodes and the placement of the electrodes should be carefully planned. The electrodes should be placed at the sidewalls of the chamber, eliminating the zones of suspension in the current setup between the electrodes and walls. Furthermore, the depth the electrodes are submerged should be adjustable. Experimental tests can be performed where the distance between the bottom of the chamber and the bottom of the electrodes is systematically changed and the effect on the decantation rate investigated.

These experimental results can then be used to further test whether the boundary-layer model and numerical simulations accurately describe electrodecantation. The efficiency of electrodecantation can be investigated experimentally by adjusting the aspect ratio of the chamber. The scaling in the boundary-layer model indicates that electrodecantation will be more effective in a high aspect ratio chamber.

The lag in the experimental decantation rate at early times, as compared to the boundary-layer model, can be studied by introducing membranes to isolate the electrodes. By isolating the electrodes from suspension, fresh electrolyte can be continuously circulated in the electrode chambers to reduce ion polarization. Electrodecantation experiments can be performed as before, measuring the growth of the clear fluid layer on the surface, to determine if the delay is indeed due to pH and other ion gradients.

In addition to isolating the electrodes, membranes can be introduced to assist in the separation process, especially at higher ionic strengths. As was described in the previous chapter, high ionic strength suspensions do not readily decant. A more effective way to treat these high conductivity suspensions may be to filter them through a membrane while applying an electric field to counter the build up of particles at the membrane surface. By electrophoretically migrating the particles away from the membrane, cake formation will be retarded and filtration can continue. Therefore, even if a clear fluid boundary layer doesn't develop, the solids levels at the membrane will be low, allowing filtration to efficiently remove water from the suspension.

After the decantation chamber is redesigned, experiments to resolve the boundary layer and fluid flow patterns can be done using polystyrene spheres in water. Since

polystyrene spheres have densities close to that of water, suspensions at low volume fractions will decrease lambda significantly to $O(10^5)$. By decreasing lambda, the clear fluid layer at the electrode may become thick enough to measure and compare to theory. Other parameters that may be manipulated to reduce lambda include the suspension viscosity, initial volume fraction of particles, and the gravitational constant, which can be reduced by performing the experiments in a microgravity environment.

One major advantage in using two-dimensional numerical simulations to study electrodecantation is that certain aspects of the separation can be turned off. For example, in the simulations presented here, ion gradients have been turned off, thus allowing a steady electric field to be applied across the suspension. Though these simulations substantiate the essential predictions of the simple model, the discrepancy between the model and experimental results at short times remain unresolved. As described in chapter 2, experimental and one-dimensional numerical studies have shown that, due to electrode reactions, ion gradients develop during electrodecantation. To determine if vertical stratification of pH and conductivity play a significant role in electrodecantation, two-dimensional simulations need to be performed under conditions where ions can be redistributed by electrodiffusional and convective processes.

Though numerical simulations at Λ on the order 10^3 and 10^4 were valuable in illustrating the buoyancy-driven flows that underlie electrodecantation, the experiments were performed with Λ on the order of 10^7. Numerical simulations were not performed at a higher lambda because, with a uniform numerical grid, prohibitively long time was required. For example, a lambda of 10^6 will require approximately one month to simulate

one hour of experiment time. The reason for this is because as lambda is increased, the thickness of the boundary layer diminishes, requiring more grid nodes to resolve the concentration and velocity fields. Since most of the changes take place over this thin boundary layer, applying a uniformly spaced grid to the entire suspension wastes a significant amount of computational time. To eliminate this numerical inefficiency, an adaptive mesh needs to be introduced. By applying a non-uniform grid, many nodes can be used to resolve the large gradients at the boundaries while comparatively fewer nodes need to be used to resolve the bulk suspension. The introduction of an adaptive mesh will allow an entire array of conditions to be simulated in a reasonable amount of time.

Studies, experimental and numerical, on higher conductivity suspensions may prove to be more applicable to real life situations. For example, solid laden waste streams from CMP processes contain many additional impurities, such as complexants, corrosion inhibitors, and metal ions that will increase the conductivity of the suspensions. As described in Appendix A, solids in high-conductivity suspensions may exhibit a tendency to form aggregates when an electric field is applied. Experimental studies to determine the rate of aggregate formation and the size of the aggregates should be performed at different ionic strengths and electric fields. Using this experimental data and existing coagulation theory, numerical simulations can be adapted to account for the possibility of aggregate formation. By developing a numerical simulation that can predict the formation of aggregates and the rate at which they will precipitate, the intermittent application of the electric field, and the strength of the electric field needed for efficient separation, can be optimized.

As mentioned above, CMP waste streams may contain metal ion impurities, and the removal of these impurities to comply with environmental regulations is becoming increasingly important. Recently, experiments have shown that metal ions can be plated onto a cathode while the suspended solids are simultaneously electrodecanted or electrocoagulated. Numerical simulations that account for the electroplating chemistry, and the interactions between the metal ions and decantation rate, would prove to be a valuable tool in determining the extent of metal ion removal. In addition, the proper numerical code would provide a unique opportunity to study electroplating and effects, e.g. altering the electrode surface or distorting the electric field, that electroplating might have on the concentration of suspended solids. The optimization of experimental parameters would simplify significantly the process of designing and improving the efficiency of a process for simultaneously removing solids and metal ions from suspension.

One additional factor to consider is Joule heating. Natural convection due to temperature gradients may disturb the separation processes by disrupting the structure of the flow field, reentraining particles into the boundary layer at the electrode, or inhibiting the formation of aggregates. Especially in higher conductivity suspensions, care needs to be taken to avoid significant heating of the suspension. Experiments can be performed to determine when Joule heating will disrupt the separation process, and numerical simulations can be extended to predict the maximum electric field strength that may be applied to a suspension, of prescribed ionic strength, before Joule heating becomes important.

Finally, the boundary-layer model is predicated on the clear-fluid boundary driving the separation process, and no attempt has been made to describe what is occurring at the other electrode where particles are accumulating. A more complete model will be very important if membranes are introduced into the system for either isolating the electrodes or performing filtration. An expanded model may provide some insight into how to minimize membrane fouling that will occurring as the particles electrophoretically migrate and concentrate at the membrane surface.

References

Acrivos, A. and Herbolzheimer, H., Enhanced Sedimentation in Settling Tanks with Inclined Walls, *J. Fluid Mech.*, **92**, 435 (1979).

Alizadeh, A., Nieto de Castro, C.A., and Wakeham, W.A., The Theory of the Taylor Dispersion Technique for Liquid Diffusivity Measurements, *Int. J. Phys.*, **1**, 243 (1980).

Beck, E.C., Giannini, A.P., and Ramirez, E.R., Electrocoagulation Clarifies Food Wastewater, *Food Techn.*, **28**, 18 (1974).

Bier, M., Terminiello, L., Duke, J.A., Gibbs, R.J., and Nord, F.F., Investigations on Proteins and Polymers. X. Composition and Fractionation of Ovomucoid, *Arch. Biochem. Biophys.*, **47**, 465 (1953).

Bier, M., in *Electrophoresis; Theory, Methods and Applications*, (M. Bier ed.), p. 270, Academic Press, New York, New York, (1959).

Bird, R.B., Stewart, W.E., and Lightfoot, E.N., *Transport Phenomena*, p. 297, John Wiley & Sons, New York, New York, (1960).

Biswas, N. and Lazarescu, G., Removal of Oil from Emulsions using Electrocoagulation, *Intern. J. Environmental Studies.*, **38**, 65 (1991).

Bjorstad, P.E., Numerical solution of the biharmonic equation., Ph.D. dissertation, Stanford University (1980).

Blank, F., and Valko, E., *Biochem. Z.*, **195**, 220 (1928).

Book, D.L., *Finite–Difference Techniques for Vectorized Fluid Dynamics Calculations*, Springer-Verlag, New York, New York (1981).

Boris, J.P. and Book, D.L., Flux–Corrected Transport. III. Minimal–Error FCT Algorithms, *J. of Comp. Phys.*, **20**, 397 (1976).

Cann, J.R., Kirkwood, J.G., Brown, R.A., and Plescia, O.J., The Fractionation of Proteins by Electrophoresis–Convection. An Improved Apparatus and its Use in Fractionating Diphtheria Antitoxin, *J. Am. Chem. Soc.*, **71**, 1603 (1949).

Cann, J.R., Brown, R.A., Kirkwood, J.G., The Fractionation of Bovine Serum Proteins by Electrophoresis–Convection, *J. Am. Chem. Soc.*, **71**, 1609, 2687 (1949).

Chen, G., Measurement and Control of Organic Contaminants in Ultrapure Water Systems, Ph.D. Dissertation, The University of Arizona (1997).

Corlett, G.L., Can CMP Waste Treatment Ever Be Environmentally Friendly?, *Adv. Appl. Contam. Control*, **12**, 19 (1998).

Dalrymple, W., Electrocoagulation of Plating Wastewaters, American Electroplaters and Surface Finishers Society, EPA, *15th Conference on Pollution Prevention and Control*, January 21-27, 1994, Orlando, Florida.

de Zeeuw, P.M., Matrix-dependent prolongations and restrictions in a blackbox multigrid solver, *J. Comput. Appl. Math.*, **33**, 1 (1990).

Do, J.-S. and Chen, M.-L., Decolourization of dye–containing solutions by electrocoagulation, *J. Appl. Electrochem.*, **24**, 785 (1994).

Donnin, J.C., Kan, J., Hassan, T.A., and Kar, K.L., The Operating Cost of Electrocoagulation, *Can. J. Chem. Eng.*, **72**, 1007 (1994).

Gutfreund, H., An Improved Method for the Fractionation of Protein Mixtures by Electrophoresis, *Biochem. J.*, **37**, 186 (1943).

Johnson, T.J. and Davis, E.J., Electrokinetic Clarification of Colloidal Suspensions, *Environ. Sci. Technol.*, **33**, 1250 (1999).

Kirkwood, J.G., A Suggestion for a New Method of Fractionation of Proteins by Electrophoresis Convection, *J. Chem. Phys.*, **9**, 878 (1941).

Kirkwood, J.G., Cann, J.R., Brown, R.A., The Theory of Electrophoresis–Convection, *Biochim. et Biophys. ACTA*, **5**, 301 (1950).

Largier, J.F., Purification of Tetanus Toxin, *Biochem. et Biophys. Acta*, **21**, 433 (1956).

Largier, J.F., The Purification of Formol Diphtheria Toxoid by Multi–membrane Electrodecantation, *J. Immunol*, **79**, 181 (1957).

Leal, L.G., *Laminar Flow and Convective Transport Processes*, p.71, Butterworth–Heinemann, Boston, Massachusetts, (1992).

Lee, C., Gidaspow, D., and Wasan, D.T., Paper presented at the *International Powder and Solids Handling and Processing Conference*, Philadelphia, PA (1979).

Matsumoto, K., Kutowy, O., and Capes, C.E., An Experimental Investigation of the Electrophoretic Sedimentation of Fine Particles in Waste Kerosene, *Powder Technol.*, 28, 205 (1981).

Matteson, M.J., Dobson, R.L., Glenn, R.W., Kukunoor, N.S., Waits, W.H., and Clayfield, E.J., Electrocoagulation and Separation of Aqueous Suspensions of Ultrafine Particles, *Colloids & Surfaces A: Physicochem. Eng. Aspects*, 104, 101 (1995).

Mendicino, L., and Brown, P.T., The Environment, Health and Safety Side of Copper Metalization, *Semiconductor International*, 6, 105 (1998).

Mosher, R.A., Saville, D.A., and Thormann, W., *The Dynamics of Electrophoresis*, VCH, Weinheim (1992).

Murphy, E.A., Electrodecantation for Concentrating and Purifying Latex, *Rubber Chem. & Techn.*, 16, 529 (1943).

Murphy, E.A., *Trans. Inst. Rubber Industry*, 18, 173 (1942).

Nielsen, L.E., and Kirkwood, J.G., The Fractionation of Proteins by Electrophoresis–Convection, *J. Am. Chem. Soc.*, 68, 181 (1946).

Parekh, B.K., Groppo, J.G., and Justice, J.H., Removal of Fine Particulates and Metal Ions from Process Discharge Waste Water using AC Electro–Coagulation Technique, *Proc. American Filtration Society*, March (1990).

Pauli, W., J. and St. Szper, The Structure and Proprieties of Highly Purified Reduction Gold Sols, *Trans. Faraday Soc.*, 35, 1178 (1939).

Pauli, W., Hochgereinigte Kolloide (Von der Elektrodialyse zur Elektrodekantation, *Helv. Chim. Acta.*, 25, 137 (1942).

Pauli, W., Untersuchungen an elektrolytfreien, wasserloslichen Proteinkorpern, *Biochem. Z.*, 152, 355 (1924).

Polson, A., Multi–membrane Electrodecantation and its Applications to Isolation and Purification of Proteins and Viruses, *Biochem. et Biophys. Acta*, 11, 315 (1953).

Pouet, M.-F., and Grasmick, A., Urban Wastewater Treatment by Electrocoagulation and Flotation, *Wat. Sci. Tech.*, 31(4), 275 (1995).

Pouet, M.-F., Persin, F., and Rumeau, M., Intensive Treatment by Electrocoagulation–Flotation–Tangential Flow Microfiltration in Areas of High Seasonal Population, *Wat. Sci. Tech.*, 25(12), 247 (1992).

Pouet, M.-F., and Grasmick, A., Electrocoagulation and Flotation: Applications in Crossflow Microfiltration, *Filtration & Separation*, **31**(3), 269 (1994).

Renk, R.R., Electrocoagulation of Tar Sand and Oil Shale Wastewaters, *Energy Progress*, **8**(4), 205 (1988).

Sauer, J.E. and Davis, E.J., Electrokinetically Enhanced Sedimentation of Colloidal Contaminants, *Environ. Sci Technol.*, **28**, 737 (1994).

Shang, J.Q. and Lo, K.Y., Electrokinetic Dewatering of a Phosphate Clay, *J. Hazard Mater.*, **55**, 117 (1997).

Shih, Y.T., Gidaspow, D., and Wasan, D.T., Sedimentation of Fine Particles in Nonaqueous Media. 1. Experimental, 2. Modeling, *Colloids & Surf.*, **21**, 393 (1986).

Silebi, C.A. and DosRamos, J.G., Axial Dispersion of Submicron Particles in Capillary Hydroynamic Fractionation, *AICHE J.*, **35**, 1351 (1989).

Sprute, R.H. and Kelsh, D.J., *Bur. Mines Rep. Invest.*, No. 8666 (1982).

Stamberger, P., The Method of Purifying and Concentrating Colloidal Dispersions by Electrodecantation, *J. Colloid Interface Sci.*, **1**, 93 (1946).

Svensson, H., Preparative Electrophoresis and Ionophoresis, *Adv. Protein Chem.*, **IV**, 251 (1948).

Szynkarczuk, J., Kan, J., Hassan, T.A., and Donnini, J.C., Electrochemical Coagulation of Clay Suspensions, *Clays & Clay Minerals*, **(42)**6, 667 (1994).

Tolliver, D.L., in *Handbook of Contamination Control in Microelectronics. Principles, Applications, and Technology.*, p.185, Noyes Publications, Park Ridge, New Jersey, (1988).

Verwey, E.J., and Kruyt, H.R., Zur Kenntnis der elektrischen Doppelschicht bei Kolloiden, *Z. Physik. Chem. (Leipzig)*, **167A**, 149 (1933).

Vik, E.A., Carlson, D.A., Eikum, A.S., and Gjessing, E.T., Electrocoagulation of Potable Water, *Water Res.*, **18**(11), 1355 (1984).

APPENDIX A: Treatment of Alumina and Silica CMP Waste by Electrodecantation and Electrocoagulation

This manuscript has been published in the *Journal of the Electrochemical Society*, (146(11), 4124-4130, 1999) and is reproduced here with kind permission from The Electrochemical Society, Inc.

Treatment of Alumina and Silica Chemical Mechanical Polishing Waste by Electrodecantation and Electrocoagulation

B. M. Belongia,[a,*] P. D. Haworth,[b,**] J. C. Baygents,[a] and S. Raghavan[b,**,z]

[a]Department of Chemical and Environmental Engineering and [b]Department of Materials Science Engineering, The University of Arizona, Tucson, Arizona 85721, USA

Electrocoagulation and electrodecantation were investigated as methods to concentrate solids from the dilute suspensions typically encountered as waste streams of chemical mechanical polishing operations. Model silica and alumina suspensions containing particles of approximately 200 nm in diameter were studied. 3 L batches of suspension were subjected to electric fields of several volts per centimeter and monitored for particle removal. Electrodecantation was shown to clarify charge stabilized, low conductivity suspensions (20 mS/cm) without modifying the mean particle size or surface-charge characteristics. The technique is thus suited to circumstances where recycle and reuse of particles is desirable, though the results also show that Joule heating may disrupt the decantation process and so must be controlled in order to apply the method to higher conductivity suspensions. Electrocoagulation was shown to effectively destabilize and clarify high conductivity suspensions (1300 μS/cm), producing aggregates several-fold larger than the primary particle size, which subsequently sedimented from suspension. Intermittent application of the electric field was found to yield superior rates of particle removal while consuming substantially less electrical power (*ca.* 1 Wh/L of clear solution).
© 1999 The Electrochemical Society. S0013-4651(99)02-042-X. All rights reserved.

Chemical mechanical polishing (CMP) has emerged as a preferred planarization technology in the manufacture of multilevel integrated circuits, and both dielectric and metal films are amenable to planarization using this technique. Dielectric films such as SiO_2 are typically planarized using highly alkaline, silica-based slurries. These slurries contain approximately 10 to 12% solids by weight and are characterized by a pH in the vicinity of 11. Acidic, alumina-based slurries are used for planarizing metal films such as W, Al, and Cu. Alumina slurries used for metal CMP contain roughly 3 to 5% solids and chemicals such as complexants, corrosion inhibitors, and oxidants. The alumina or silica particles in the slurry are submicron in size and hence may be considered to be in the colloidal regime.

A key consumable in the CMP process is the polishing/planarizing slurry. The major waste stream from a CMP tool is the polishing slurry in a very diluted form. For example, the waste from a dielectric planarization step is a suspension of silica particles at a concentration of 0.05 to 0.2%. Available information indicates that approximately 30 to 50 L of waste slurry may be generated per 200 mm wafer for each level of planarization. Waste slurries may undergo further dilution if mixed with post-CMP clean rinse water. With increased implementation of the CMP technique in fabrication areas, the problem of slurry waste treatment is attracting increasing attention. To comply with environmental regulations and to allow for recycling of deionized water, these dilute slurries have to be treated to separate solids from the liquid dispersion medium. In addition, there is some interest in recycling the silica waste slurries; this requires that the waste slurry be thickened to approximately 10% solids without altering the size of the particles.

Dispersed particles may be removed from suspension by coagulation or flocculation. Coagulating agents are usually polyvalent electrolytes such as calcium, aluminum, and iron salts, which reduce the electrostatic interparticle repulsion sufficiently so that the van der Waals attraction predominates, allowing the particles to agglomerate. Flocculants are typically high molecular weight polymers that adsorb onto particles and bind the solids together by the formation of interparticulate bridges. In both cases, aggregates result, which then settle under the action of gravity.

Concentration of colloidal suspensions has also been observed when an electrical current is passed through suspensions. This approach has been used to separate colloidal matter from the disper-

sion medium. There are believed to be two distinct mechanisms responsible for this observation: electrocoagulation and electrodecantation. These electrochemical phenomena represent an alternative approach to chemical conditioning for solid-liquid separation in colloidal suspensions, and have been applied to the separation and purification of organic and inorganic colloidal matter on both industrial and laboratory scales.

Electrocoagulation has been studied as a means of treating waste waters containing food and protein,[1] oil,[2] dyes,[3] and various suspended particles including clays and silica.[4-7] The mechanism is believed to involve the *in situ* generation of ions by the dissolution of the electrodes. Consumable metal electrodes, such as iron or aluminum, are used to continuously produce metal ions in the vicinity of the anode. Electrophoretic motion simultaneously concentrates negatively charged particles in the region of the anode. The released ions neutralize the charge of the particles thereby facilitating coagulation.[8,9] Inert electrodes, such as titanium,[9] and the passage of an alternating current[10] have also been observed to remove metal ions from solution, and to initiate the coagulation of suspended solids.

In the electrocoagulation process, the electric field is applied to the medium for a short time (less than 10 min), and the treated dispersion transferred to a separation stage where settling occurs. In many applications the efficiency of the reaction has been improved by gentle agitation during the electrochemical treatment, by either stirring or bubbling gas.[1-3] In the latter case, a combination of electrocoagulation and flotation has been found to be an effective treatment of urban wastewater.[1,11] Electrocoagulation has also been used in conjunction with filtration to remove silica and suspended solids that tend to foul reverse osmosis membranes, thereby extending the life of the membranes.[12,13]

Electrodecantation, by contrast, is a technique that has drawn limited interest in recent years. A complete historical perspective of the subject can be found in various review articles.[14-16] The phenomenon was first observed when Pauli[17] noted that the passage of a direct electrical current through a suspension of charged colloids resulted in the development of two distinct layers; the bottom one contained most of the colloidal material. A mechanism for this process was first proposed by Blank and Valko,[18] and then verified by Verwey and Kruyt.[19] Electrodecantation results from the charged particles migrating electrophoretically toward the electrode of opposite charge. The accumulation of particles around that electrode increases the density locally and thus the particle-enriched suspension sinks to the bottom of the vessel. At the opposite electrode, a colloid-depleted region develops and rises. The stratification, or

decantation, process is stabilized against mixing by the resultant vertical density gradients.

The electrodecantation mechanism has been applied to the separation of gold sols,[20] proteins,[21-26] and viruses.[27,28] Variations have been exploited to facilitate the separation of a variety of colloidal matter. For example, particles with a specific gravity less than the surrounding medium tend to accumulate at the top of the vessel, and rubber latex has been collected as a cream in this way.[29,30] The passage of an electric current has no effect on uncharged material; this allows the separation of mobile particles from those at their isolectric point.[22] Multiple membrane devices[28,31] and semicontinuous/continuous flow designs[29,32] have also been developed. Many of these approaches have been adapted to industrial-scale applications.

The objective of this work was to investigate the effect of passing an electrical current through well-characterized aqueous dispersions of submicron-sized silica or alumina particles. Electrocoagulation and electrodecantation were both studied to assess their utility for removing solids from simulated waste CMP slurries. Specifically, the effect that the applied field had on the concentration and size distribution of suspended and sedimented particles was characterized.

Experimental

Suspension preparation.—Colloidal silica and alumina suspensions were used. Silica (SiO_2) suspensions were prepared by diluting a commercially available, KOH-based, silica CMP slurry, containing ≈ 11.5 wt/vol % silica, with deionized water. Alumina (Al_2O_3) stock suspensions were prepared at a concentration of 5 wt/vol % by dispersing high-purity, submicron-sized, α-alumina particles in deionized (DI) water. Appropriate amounts of stock silica and alumina slurries were diluted with distilled water to achieve concentrations of 0.1–0.7 and 0.3–0.6 wt/vol %, respectively. The suspensions were sonicated for 5 min with a model W-375 sonicator/cell disruptor (Heat Systems-Ultrasonics, Inc.) to break up aggregates and disperse the solids.

The size distribution of particles in suspension was measured with a Coulter N4 plus particle size analyzer. Turbidity, conductivity, and pH measurements were performed with a Hach ratio/XR turbidimeter, Orion model 122 hand held conductivity meter using the standard probe, and an Orion model 701A digital ion analyzer pH meter, respectively. Electrophoretic mobility measurements were made on diluted suspensions (approximately 0.01 wt/vol % solids) with a Lazer Zee meter, model 501 (Pen Kem, Inc.). The pH of the suspensions was adjusted by adding small amounts of KOH/HNO_3 or $NaOH/HCl$.

Experiments.—A Plexiglas chamber, depicted in Fig. 1, was designed to perform the experiments. Three liters of a suspension were placed in the chamber. Two 10.0 cm wide 304 stainless steel mesh electrodes (wire diameter 0.24 mm, 15.75 × 15.75 wires/cm) were oriented vertically and submerged 11.5 cm into the suspension. Electrodes of platinum–coated glass plates, 10.0 cm wide, and submerged 8.0 cm into the suspension, were also tested. The electrodes were placed 11.0 cm apart and connected to a manual switching device, which in turn was connected to a Hewlett Packard 6634A dc power supply. The switching device was used to reverse the polarity of the electric field to suppress accumulation of particles on the electrodes. An electric field (E) of 2.5 to 10.0 V/cm was applied to the suspension and the polarity was switched periodically. The suspension was monitored visually for the formation of a clear fluid layer. Turbidity, conductivity, and pH measurements were performed on samples taken from the top clear layer (directly below the suspension surface), bottom concentrated layer (collected from the bottom of the container), and six sample ports (indicated on Fig. 1) at the end of the experiments; sample ports above the suspension surface were not used. Size measurements on the concentrated solids were carried out as previously described.

Analogous studies were also performed on alumina suspensions doped with KNO_3, which was added to increase conductivity and diminish charge stabilization of the suspension. Suspensions with KNO_3 concentrations of 1 or 10 mM were studied. Electric fields of
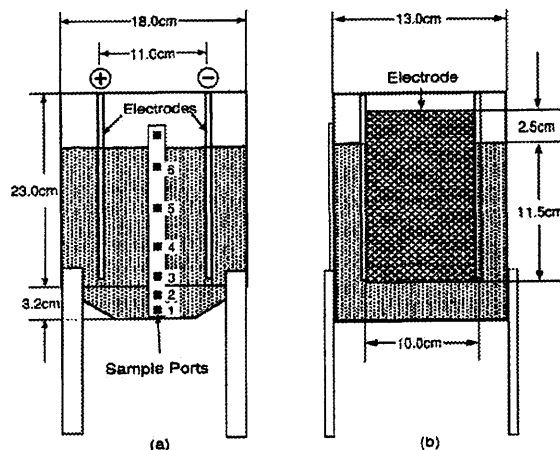
Figure 1. Experimental apparatus: (a) Front view with six sample ports labeled. (b) Side view.

7.3 or 3.6 V/cm were applied, and the polarity of the electric field periodically reversed. After an interval of treatment, the field was removed and the particle concentration changes monitored by turbidity measurements.

Results and Discussion

Suspension characteristics.—Silica (SiO_2) and alumina (Al_2O_3) particles used in the preparation of model suspensions had mean diameters of 208 ± 59 and 203 ± 72 nm, respectively. Figure 2 shows the electrophoretic mobility of silica and alumina particles as a function of solution pH. The isoelectric points (IEP) of the silica and alumina samples can be identified to be approximately 2 and 9, respectively.

Experimental results.—Figures 3 and 4 illustrate the effect of an applied electric field on the separation of particles from silica ($\sigma \approx$ 250 μS/cm, pH $\approx$ 9.3) and alumina ($\sigma \approx$ 20 μS/cm, pH $\approx$ 4.2) suspensions, respectively. The suspension characteristics were chosen
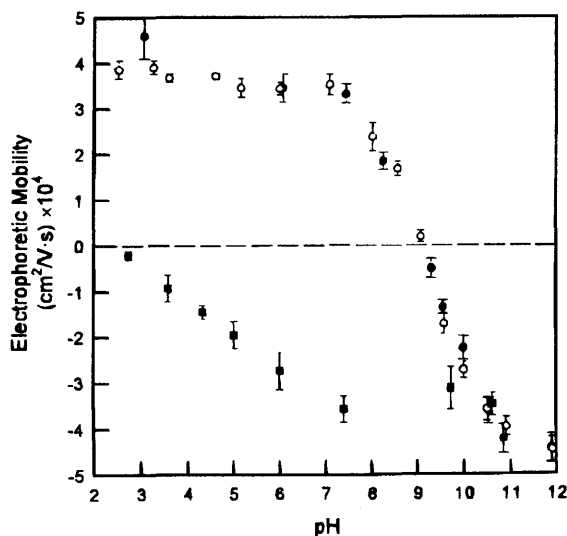
Figure 2. Electrophoretic mobility as a function of pH. (O) 203 nm alumina in DI water; (●) 203 nm alumina in 5 mM KCl; (■) 208 nm silica in 5 mM KCl.

to represent typical slurry wastes from dielectric and metal CMP operations. Figures 3a and 4a show the concentration of solids on the bottom of the container (c_{scd}) normalized to the original solids concentration (c_0). It may be seen that the solids concentration increased at a rate of ≈ 5.1 and ≈ 3.2 h^{-1}, respectively, for silica in a field of 2.5 V/cm and for alumina in a field of 7.5 V/cm. Particle size measurements on these concentrated solids (≈ 10 wt/vol % SiO_2 and ≈ 3.5 wt/vol % Al_2O_3) showed that the mean diameter of the particles was 215 ± 84 and 238 ± 84 nm for silica and alumina, respectively. These sizes matched the mean primary particle size in the initial slurries. To ensure that ferric ions released during dissolution of

the stainless steel anode were not responsible for the particle/liquid separation, two experiments were performed with inert platinum electrodes. The results of these two experiments are also plotted on Fig. 4a and show that, as with the stainless steel electrodes, the solids were concentrated at a comparable rate when an electric field was applied. Again, no change in particle size was measured.

Measurements on the electrophoretic mobility of the particles concentrated at the bottom of the chamber (data not shown) were identical to those on the initial suspensions (Fig. 2). These mobility data, showing no difference between the treated and untreated parti-
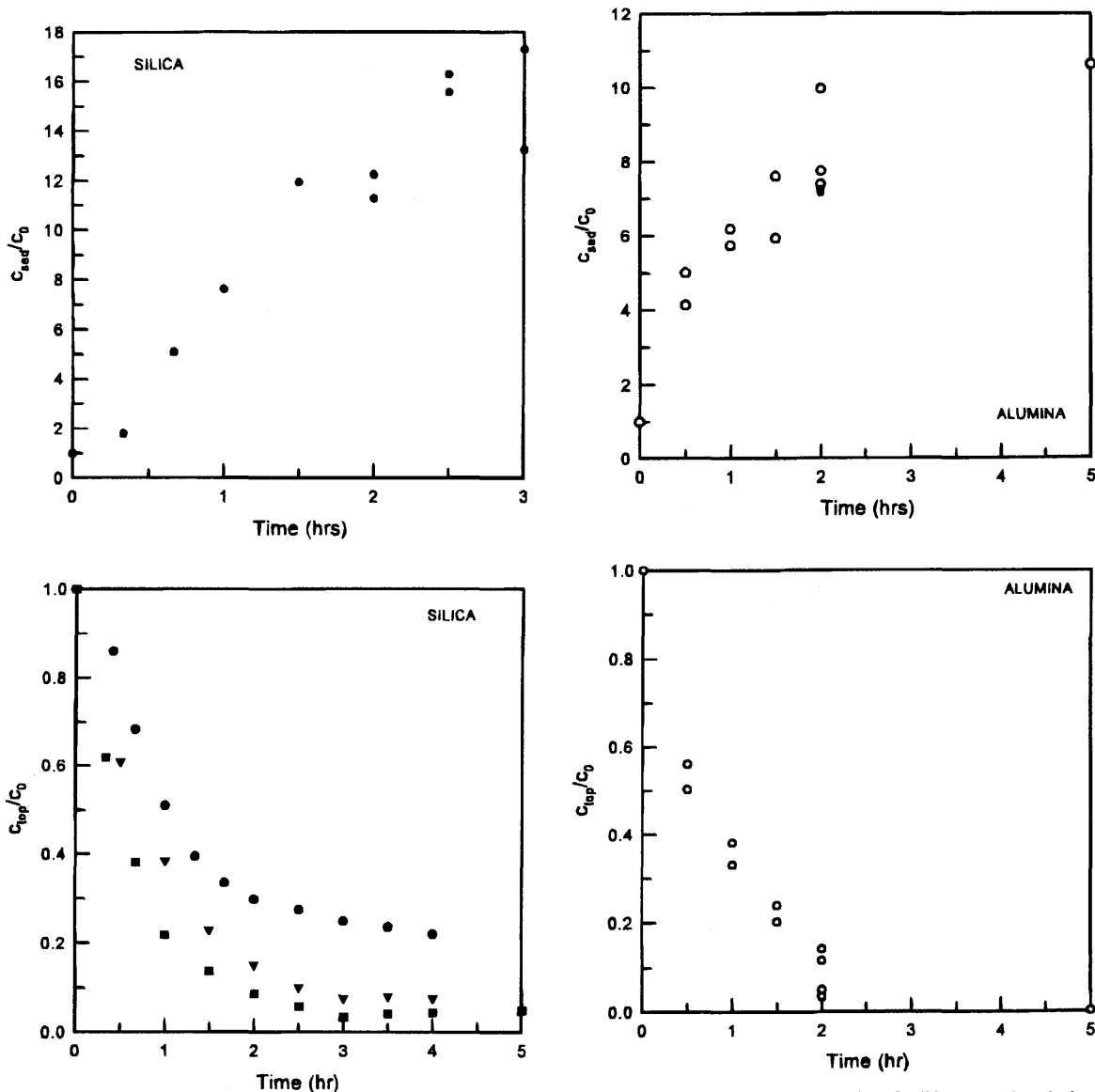
Figure 3. (a, top) Normalized concentration of solids measured on the bottom of the container. (208 nm silica, $c_0 = 0.66$ wt/vol %, $\sigma \approx 250$ μS/cm, pH *ca.* 9.3, no polarity switching, $E = 2.5$ V/cm.) (b, bottom) Normalized concentration of solids measured 2.5 cm below the surface. 208 nm silica, $c_0 = 0.66$ wt/vol %, $\sigma \approx 250$ μS/cm, pH ≈ 9.3, no polarity switching. (●) $E = 2.5$ V/cm; (▼) $E = 5.0$ V/cm; (■) $E = 10.0$ V/cm.

Figure 4. (a, top) Normalized concentration of solids measured on the bottom of the container. 203 nm alumina, $c_0 = 0.32$-0.63 wt/vol %, $\sigma \approx 20$ μS/cm, pH ≈ 4.2, $E = 7.3$ V/cm, polarity switched every 2 min. (○) Stainless steel electrodes, (●) inert platinum electrodes. (b, bottom) Normalized concentration of solids measured 2.5 cm below the surface. (203 nm alumina, $c_0 = 0.32$-0.63 wt/vol %, $\sigma \approx 20$ mS/cm, pH ≈ 4.2, E = 7.3 V/cm, polarity switched every 2 min, with stainless steel electrodes.

cles, along with the absence of aggregation, indicate that electrode-cantation is the active mechanism causing stratification of the solids in these suspensions.

Figures 3b and 4b show the rate of particle removal from the top layer of silica and alumina suspensions; samples were taken 2.5 cm beneath the surface, about three-quarters of the way up from the bottom of the electrodes (see sample port 6 in Fig. 1). As can be seen in the figures, the normalized concentration of solids in the top layer (c_{top}/c_0) decreases with time. In each case a stage is reached where continued application of the electric field has little effect on c_{top}, though a significant difference between the silica and alumina suspensions was observed. In the alumina suspensions ($\sigma \approx 20$ μS/cm), a clear fluid layer developed above the bulk of the suspension. This clear layer continued to grow as the experiment proceeded, and the interface between the clear fluid layer and the bulk suspension reached the sampling position (2.5 cm below the surface) at 120 min (see Fig. 4b). The silica suspensions did not develop a distinct clear fluid layer during the separation process, which may be due to Joule heating associated with the higher suspension conductivity (see below).

For the apparatus shown in Fig. 1, imposition of fields on the order of several volts per centimeter produced temperature increases of several degrees Celsius (or more) in higher conductivity suspensions ($\sigma > 100$ μS/cm). No temperature increases were detected in the low conductivity suspensions ($\sigma \approx 20$ μS/cm). The electrode-cantation process will be most effective under (otherwise) quiescent conditions. Joule heating causes thermal convection, and this interferes with the decantation. In a separate set of experiments (data not shown), fumed silica particles were dispersed in deionized water to produce a low conductivity suspension (≈ 0.65 wt/vol %, $\sigma \approx 5$ μS/cm, pH ≈ 4.4). When an electric field of 7.3 V/cm was applied to the suspension, a clear layer formed and behavior analogous to that of the alumina suspensions was observed.

To further establish that electrodecantation is the controlling separation mechanism for the data shown in Fig. 3 and 4, a test with silica suspensions was performed where stirring was introduced. The results of this experiment (Fig. 5) show that as long as there was stirring, no significant separation occurred. As soon as stirring ceased, a substantial drop occurred in the concentration of solids 2.5 cm

below the surface. Additionally, when the field was removed, the rate of particle depletion fell to nil.

The extent and rate at which solids are removed from the top layer increases with the electric field strength provided Joule heating is avoided. Figure 6 shows the solids removal rate 2.5 cm below the surface for the data in Fig. 3b. The rates were calculated by plotting these data on a semilog plot, fitting a line to the portion of the curve where significant removal of the solids occurred, and determining the slope of these lines. Electrodecantation stems from electrophoretic motion of the particles, which is directly related to the applied field strength. Higher electrophoretic velocities imply that particles migrate faster toward the electrode of opposite charge, causing more rapid density increases at this electrode. Similarly, a particle–depleted region forms more rapidly at the opposite electrode. The differences in densities cause the particles to settle out along one of the electrodes and the particle–depleted layer to rise toward the surface along the other electrode.[33]

An operational problem related to the mechanism of electrodecantation is that particles may form a cake on the electrode of opposite charge. In our studies, cakes formed during experiments that involved the continuous application of a dc field. As the cake continued to grow, the strength of the electric field was probably reduced within the suspension. To eliminate the buildup of particles on the electrodes, periodic reversal of the polarity of the electrode was investigated. Figure 7 displays the effects of periodic reversal of the electric field on the concentration of silica particles at two different electric field strengths. The results imply that polarity switching need not hinder the separation and may actually enhance the rate of separation at higher field strengths.

Due to dissolved metal ions and chemical additives, slurry wastes from metal CMP processes are often characterized by electrical conductivities on the order of 100 to 1000 mS/cm. Consequently, aqueous alumina suspensions containing 1 mM and 10 mM KNO_3 ($\sigma \approx 150$ μS/cm, pH ≈ 5.2 and $\sigma \approx 1350$ μS/cm, pH 5.7, respectively) were prepared. These suspensions remained stable for over 2 h in the absence of an electric field. Application of an electric field across these suspensions caused particles to settle, as may be seen in Fig. 8. A field of 7.3 V/cm was required to accomplish approximately the same particle removal from the 1 mM KNO_3 suspension as was managed with 3.6 V/cm field in the 10 mM KNO_3 suspension.
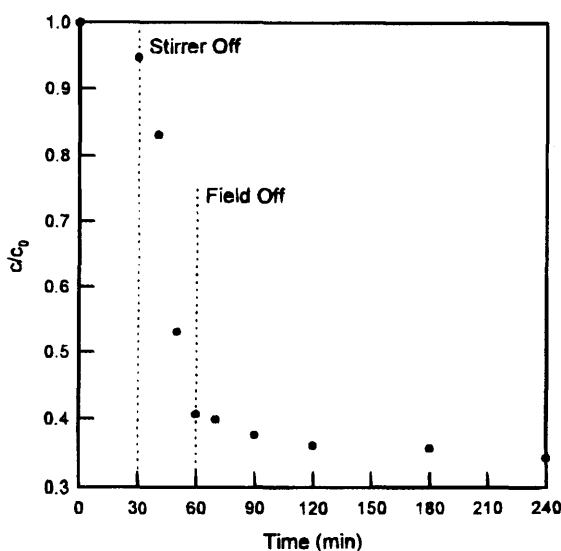
Figure 5. Effects of stirring and removing the electric field on particle concentration, as measured 2.5 cm below the suspension surface. (208 nm silica, $c_0 = 0.13$ wt/vol %, $\sigma \approx 55$ μS/cm, pH ≈ 9.3, $E = 5.0$ V/cm, no polarity switching.)
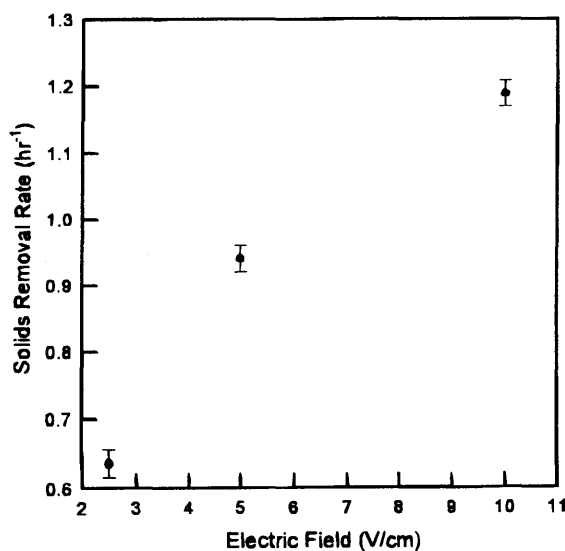
Figure 6. Removal rate of silica particles 2.5 cm below the surface at different field strengths. (208 nm silica, $c_0 = 0.66$ wt/vol %, $\sigma \approx 250$ μS/cm, pH ≈ 9.3, no polarity switching.)
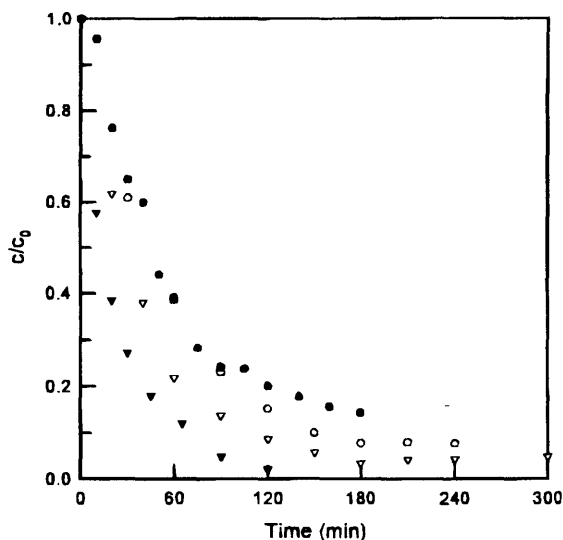
Figure 7. Effect of switching the polarity of the electrodes on 208 nm silica removal 2.5 cm below the surface ($c_0 \approx 0.65$ wt/vol %, $\sigma \approx 250$ μS/cm). (O) $E = 5.0$ V/cm, no polarity switching; (●) $E = 5.0$ V/cm, polarity switched every 2 min; (∇) $E = 10.0$ V/cm, no polarity switching; (▼) $E = 10.0$ V/cm, polarity switched every 2 min.

This can be explained by the increased Debye screening that results with larger salt concentrations. Diminished electrostatic repulsions allow the particles to more readily form aggregates that settle out of suspension. In both 1 and 10 mM suspensions, large aggregates were visually observed to form and settle during the experiments, indicating that the electric field either induced coagulation or markedly enhanced the coagulation kinetics. Particle size

measurements on the collected solids showed that the mean size of particles in the sediment was approximately 500 nm in the 1 mM KNO_3 suspensions and greater than 1000 nm in diameter in the 10 mM KNO_3 suspensions. These results are in direct contrast to those depicted in Fig. 3 and 4, where particle aggregation was negligible. Furthermore, it is interesting to note that the experiments on silica suspensions at pH 9.3 (Fig. 3), performed at approximately the same conductivity as the 1 mM KNO_3 alumina suspensions, did not show any size change after treatment. It is well known that silica suspensions are highly charge–stabilized at high pH values [34] and presumably this explains why coagulation was not observed.

Figure 9 shows the results of different electric field application schemes on particle removal by electrocoagulation. The three data sets were obtained for the same initial conditions (10 mM KNO_3, 3.6 V/cm). As can be seen, the concentration of solids 2.5 cm below the surface was roughly the same whether the periodically reversed electric field was applied for the first 15 min, or for the entire 120 min. Only 70% of the solids were removed after 120 min in both of these experiments. The results show that if the electric field is removed after 15 min, the particle depletion substantially decreases after 30 min, indicating that not all of the particles have coagulated. Continually applying the electric field for 120 min causes significant stirring due to Joule heating and gas evolution at the electrodes. This mixing holds some of the solids in suspension and may also result in smaller aggregate size, slowing the collection of the solids at the chamber bottom.

The experiment in which an electric field of 3.6 V/cm was applied for 5 min, removed for 10 min, reapplied for 5 min, and so on, yielded the greatest particle removal. Intermittent application of the electric field allows large agglomerates to settle when the field is removed. When the electric field is subsequently reapplied, particles that have not been subsumed into large aggregates can be captured/aggregated. Some resuspension of large aggregates may also occur (due to Joule heating and gas evolution), but the resuspended aggregates simply settle out of suspension after the field is removed.

The applied electric field, whether continuous or intermittent, affects the nature of the solid/liquid separation of alumina suspensions
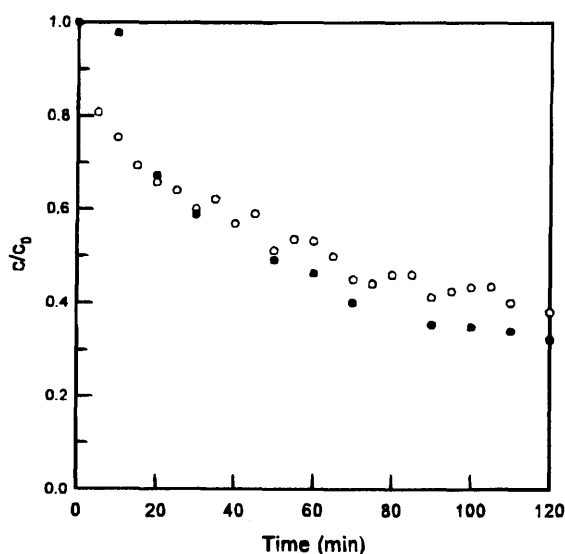
Figure 8. Normalized concentration of alumina 2.5 cm below the surface for high conductivity suspensions. (O) 203 nm alumina and 1 mM KNO_3, $c_0 \approx$ 0.40 wt/vol %, $\sigma \approx 150$ μS/cm, pH $\approx$ 5.2, $E = 7.3$ V/cm, polarity switched every 2 min; (●) 203 nm alumina and 10 mM KNO_3, $c_0 \approx 0.40$ wt/vol %, $\sigma \approx 1350$ mS/cm, pH $\approx$ 5.7, $E = 3.6$ V/cm, polarity switched every 2 min.
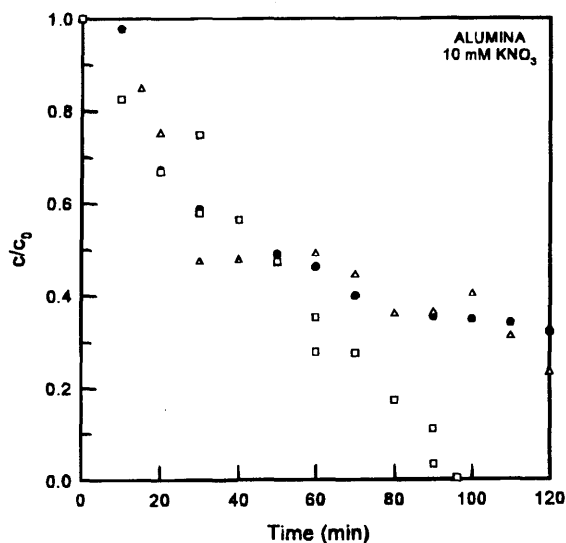
Figure 9. Influence of electric field on alumina particle removal by electrocoagulation. (Concentration measured 2.5 cm below the surface. $c_0 \approx$ 0.40 wt/vol %, $\sigma \approx 1350$ mS/cm, pH $\approx$ 5.7, $E = 3.6$ V/cm, with polarity switched every 2 min. (●) Field applied for entire experiment; (△) field applied for first 15 min of experiment; (□) field applied for 5 min, off for 10 min, on for 5 min, and so on.)

(a)

(b)
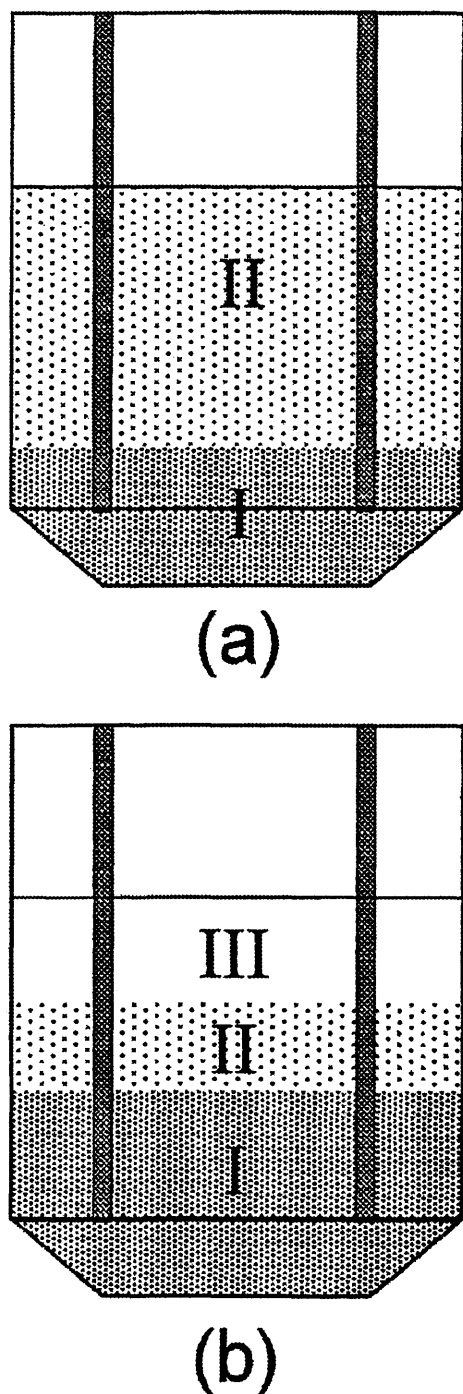
Figure 10. Schematic of the different concentration layers formed due to electrocoagulation of alumina suspensions ($\sigma \approx 1350$ mS/cm). (a) $E = 3.6$ V/cm continuously applied for 2 h. Region I, concentrated solids layer, $c = 0.13-1.98$ wt/vol %. Region II, particle-depleted layer, $c \approx 0.13$ wt/vol %. (b) $E = 3.6$ V/cm applied for 5 min, removed for 10 min, applied for 5 min, etc. for a total of 90 minutes. Region I, concentrated solids layer, $c = 0.13-1.63$ wt/vol %. Region II, particle-depleted layer, $c \approx 0.13$ wt/vol %. Region III, clear fluid layer, $c \approx 0.01$ wt/vol %.

as is indicated in Fig. 10. The situation depicted in panel (a) is obtained when the field is continuously applied (with polarity switching). The particle concentration of about two-thirds (2000 mL) of the suspension was reduced from 0.40 to ≈ 0.13 wt/vol % after 2 h (cf. region II). Three distinct concentration zones, instead of two, formed when the electric field was applied intermittently (panel b); 97% of the solids were removed from ≈ 700 mL (23%) of the suspension after 90 min (region III), and an additional transition zone of ≈ 700 mL, containing ≈ 0.13 wt/vol % solids (region II), developed between the clear top layer and the bottom concentrated layer. A rough calculation using the measured current shows that the power requirement to create a particle–depleted zone, ≈ 0.13 wt/vol % solids, using a continuous field was 3.5×10^{-2} kWh/L. By using an intermittent electric field, the power consumption can be reduced to 1.1×10^{-3} for a clarified region containing ≈ 0.01 wt/vol % solids.

Conclusions

Electrodecantation and electrocoagulation have been demonstrated as techniques to separate colloidally stable alumina and silica particles from suspensions. Electrodecantation was found to be the controlling mechanism in the treatment of silica ($\sigma \approx 250$ μS/cm) and alumina ($\sigma \approx 20$ μS/cm) suspensions and appears to be a potentially useful technique for the concentration of diluted charge-stabilized suspensions at these low ionic strengths. Because the physical and electrochemical properties of the particles in suspension remain unchanged by the concentration process, this process is suited to collecting particles to be recycled and reused in CMP. This is in direct contrast to the higher conductivity alumina suspensions where aggregates formed during the application of the electric field (electrocoagulation). The transition from electrodecantation to electrocoagulation is gradual and will depend on the suspension stability as a function of ionic strength and pH. It was found that when electrocoagulation occurs, periodic removal of the electric field increased the efficiency of separation.

The experimental approach discussed in the manuscript pertains to the feasibility of using electrocoagulation and electrodecantation to concentrate solids from simulated waste CMP slurries. The treatment of large amounts of waste generated during CMP requires that the separation process evolve from a batch process to a semibatch or continuous process. In developing a continuous flow apparatus, the separation chamber characteristics, such as distance between electrodes, need to be optimized to efficiently treat waste streams. In addition, chemicals present in CMP waste streams, *e.g.*, complexants, corrosion inhibitors, and metal ions, may influence which mechanism, electrodecantation/electrocoagulation, will dominate solid/liquid separation.

References

1. E. C. Beck, A. P. Giannini, and E. R. Ramirez, *Food Technol.*, **18-19**, 22 (1974).
2. N. Biswas and G. Lazarescu, *Int. J. Environ. Stud.*, **38**, 65 (1991).
3. J.-S. Do and M.-L. Chen, *J. Appl. Electrochem.*, **24**, 785 (1994).
4. J. C. Donnin, J. Kan, T. A. Hassan, and K. L. Kar, *Can. J. Chem. Eng.*, **72**, 1007 (1994).
5. J. Szynkarczuk, J. Kan, T. A. Hassan, and J. C. Donnini, *Clays Clay Miner.*, **42**, 667 (1994).
6. M. J. Matteson, R. L. Dobson, R. W. Glenn, N. S. Kukunoor, W. H. Waits, E. J. Clayfield, *Colloids Surf. Physicochem. Eng. Aspects*, **104**, 101 (1995).
7. R. R. Renk, *Energy Prog.*, **8**, 205 (1988).
8. E. A. Vik, D. A. Carlson, A. S. Eikum, and E. T. Gjessing, *Water Res.*, **18**, 1355 (1984).
9. W. Dalrymple, Paper presented at American Electroplators and Surface Finishers Society EPA, 15th Conference on Pollution Prevention and Control, Jan 21-27, 1994, Orlando, FL.
10. B. K. Parekh, J. G. Groppo, and J. H. Justice, in *Proceedings of American Filtration Society* Meeting (March 1990).
11. M.-F. Pouet and A. Grasmick, *Water Sci. Technology*, **31**, 275 (1995).

12. M.-F. Pouet, F. Persin, and M. Rumeau, *Water. Sci. Technol.,* **25,** 247 (1992).
13. M.-F. Pouet and A. Grasmick, *Filtr. Sep.,* **31,** 269 (1994).
14. P. Stamberger, *J. Colloid Interface Sci.,* **1,** 93 (1946).
15. H. Svensson, *Adv. Protein Chem.,* **IV,** 251 (1948).
16. M. Bier, in *Electrophoresis: Theory, Methods and Applications,* M. Bier, Editor, p. 270, Academic Press, New York (1959).
17. W. Pauli, *Biochem. Z.,* **152,** 355 (1924).
18. F. Blank and E. Valko, *Biochem. Z.,* **195,** 220 (1928).
19. E. J. Verwey and H. R. Kruyt, *Z. Phys. Chem. (Leipzig),* **167A,** 149 (1933).
20. W. Pauli, J. Szper, and St. Szper, *Trans. Faraday Soc.,* **35,** 1178 (1939).
21. J. G. Kirkwood, *J. Chem. Phys.,* **9,** 878 (1941).
22. H. Gutfreund, *Biochem. J.,* **37,** 186 (1943).
23. L. E. Nielsen and J. G. Kirkwood, *J. Am. Chem. Soc.,* **68,** 181 (1946).
24. J. R. Cann, J. G. Kirkwood, R. A. Brown, and O. J. Plescia, *J. Am. Chem. Soc.,* **71,** 1603 (1949).

25. J. R. Cann, R. A. Brown, and J. G. Kirkwood, *J. Am. Chem. Soc.,* **71,** 1609, 2687 (1949).
26. M. Bier, L. Terminiello, J. A. Duke, R. J. Gibbs, and F. F. Nord, *Arch. Biochem. Biophys.,* **47,** 465 (1953).
27. J. F. Largier, *Biochem. Biophys. Acta,* **21,** 433 (1956).
28. J. F. Largier, *J. Immunol.,* **79,** 181 (1957).
29. E. A. Murphy, *Rubber Chem. Technol.,* **16,** 529 (1943).
30. E. A. Murphy, *Trans. Inst. Rubber Ind.,* **18,** 173 (1942).
31. A. Polson, *Biochem. Biophys. Acta,* **11,** 315 (1953).
32. W. Pauli, *Helv. Chim. Acta.,* **25,** 137 (1942).
33. J. C. Baygents, B. M. Belongia, P. D. Haworth, S. Raghavan, and L. R. White. *Ind. Eng. Chem. Res.,* Submitted.
34. T. W. Healy, in *Stability of Aqueous Silica Salts in Colloid Chemistry of Silica,* H. E. Bergna, Editors, pp. 147-165, American Chemical Society, Washington, DC (1994).

APPENDIX B: Electrodecantation of Stable Colloidal Dispersions

This manuscript is to be submitted to *Industrial & Engineering Chemistry Research*.

ELECTRODECANTATION OF STABLE COLLOIDAL DISPERSIONS

J.C. Baygents,[*,†] B.M. Belongia,[‡] P.D. Haworth,[§] S. Raghavan[§] & L. R. White[†,¶]

†Department of Mathematics and Statistics,
The University of Melbourne, Parkville, Victoria 3052, Australia

‡Department of Chemical and Environmental Engineering,
The University of Arizona, Tucson, AZ 85742, U.S.A.

§Department of Materials Science and Engineering,
The University of Arizona, Tucson, AZ 85742, U.S.A.

to be submitted to *Industrial & Engineering Chemistry Research*

[*]Corresponding author; permanent address:

Department of Chemical and Environmental Engineering

The University of Arizona

Tucson, AZ 85742, U.S.A.

(520)621-6043

(520)621-6048 fax

jcb@maxwell.che.arizona.edu

[¶]Permanent address:

Department of Chemical Engineering

Carnegie Mellon University

Pittsburgh, PA 15213, U.S.A.

Abstract

Electrically-driven stratification of stable, mondisperse suspensions of sub-micron-sized particles has been studied in a 3-liter batch cell. A horizontally-directed electric field ($<$ 10 V/cm) produces a clear fluid layer that grows atop low-conductivity ($<$ 20 μS/cm) aqueous dispersions of silica or alumina particles, as particles concentrate in the bottom of the cell. A model of the process, which neglects particle diffusion and sedimentation, indicates that the clear layer results from the rise of fluid adjacent to the electrode from which particles are electrophoretically repelled. Particle depletion near this electrode occurs rapidly compared to b/v_e, the time scale for the stratification process, where b is the separation between electrodes (11 cm) and v_e is the electrophoretic velocity of the particles in suspension (ca. 10^{-3} cm/sec). Reversal of electrode polarity with a frequency of 10^{-2}–10^{-3} sec^{-1} prevents particle buildup on the immersed electrodes and does not measurably alter the clear layer growth rate. Neither does it matter whether the particles are positively or negatively charged. The growth rate of the clear layer at the top of the chamber is initially slower than that predicted by the theory; at later stages the theory and experiment are in agreement. The discrepancies may be attributable to several factors, including omission of electrolyte and temperature gradients from the model, the geometry of the electrodes and the design of the batch cell.

Introduction

Electrophoresis is particle translation caused by the imposition of an electric field. In contrast to particle sedimentation, electrophoretic velocities are of the same order of magnitude, in a given electric field, for species ranging from small alkali-metal ions to 100-μm biological cells. Electric fields are thus potentially useful to manipulate suspensions encompassing a broad range of particle sizes for which sedimentation processes are not viable.

One such manipulation scheme is a separations process known alternatively as electrodecantation[1] or electrophoresis-convection[2]. According to Bier[1], electrodecantation was first reported by Adolf and Pauli[3], who were performing electrodialysis experiments on human serum albumin and noticed an attendant stratification of the protein in solution. Subsequently, Blank and Valko[4] described the qualitative mechanism that resulted in the strata: negatively-charged macroions were repelled from the cathode and attracted to the anode. This produced density gradients in the vicinity of the electrodes and resulted in natural convection that, depending on the density of the macroions, either carried them to the top or bottom of the chamber. Three decades later, Kirkwood, et al.[2] offered the first quantitative decription of the phenomenon, formulating a theory for the limit $v_e b/D \ll 1$, where b is the electrode separation and v_e and D are, respectively, an electrophoretic

velocity and diffusivity characteristic of the stratified species in solution. The dimensionless group $v_e b/D$ can be interpreted as an electric Peclet number that weighs the relative importance of electrophoretic (or electromigrational) and diffusive transport, meaning the Kirkwood, et al. analysis applies to highly diffusive systems.

In nearly any circumstance of practical interest, $v_e b/D \geq 10^2$. It is therefore surprising that, despite the design and implementation of industrial and bench-scale electrodecantation devices (cf. Bier[1] for a review), there has been no signifcant advance of the theory beyond the low Peclet number limit.

Here we revisit the principles of electrodecantation and analyze the limit of large electric Peclet number, since this is the appropriate asymptote for particulate suspensions. Our interest in the problem stems from a set of simple batch electrodecantation experiments that we performed on monodisperse, aqueous dispersions of sub-micron silica and alumina particles. The experiments yielded stratified suspension resembling that which results from sedimentation, except the process unfolds on a time scale characterized by b/v_e. In particular, a clear fluid develops and grows on the top of the suspension and particles collect in the bottom of the electrodecantation cell, as sketched in Figure 1.

We begin the presentation with a development of a simple mathematical model of electrodecantation. We assume at the outset that the suspension is isothermal and that the electric field between the elec-

trodes is independent of position. These assumptions were similarly invoked by Kirwood, et al., and allow us to draw heavily on the analysis applied by Acrivos and Herbolzheimer[5] to enhanced sedimentation in inclined settlers. The scaling shows that the system behavior is largely governed by two dimensionless groups: $\mathcal{R} \equiv v_e l/\mu_f$, a Reynolds number of order unity, where l is the electrode height and ρ_f and μ_f respectively denote the fluid density and viscosity; and $\Lambda \equiv l^2 g(\rho_p - \rho f)c_0/\mu_f v_e$, a large parameter denoting the Grashof number divided by the Reynolds number, where g is the acceleration due to gravity and ρ_p and c_0 are the density and initial volume fraction of the particles in suspension.

We then describe the aforementioned experiments and make comparisons with the model. The observations are consistent with the model predictions, except that the clear layer growth rate comes into agreement with the theory only in the later stages of the batch process. Other discrepancies between the model and the observations, as well as their likely explanations, are taken up in the discussion. In addition, because the process leaves the particle zeta-potential and size distribution unaltered, some comments are made concerning the utility of electrodecantation as a method to gently decant clear fluid from suspensions of particles that are far too small to sediment at a practical rate.

Principles of Electrodecantation

The analysis of electrodecantation begins with the balance laws. The simplest possible formulation is one in which the system is taken to be isothermal and void of ion gradients, which we have done. The constant temperature assumption, in effect, omits consideration of Joule heating. In high ionic strength systems, this is clearly a poor assumption. However, as will become evident, it is not obvious that electrodecantation will work properly in systems which are not well-thermostated, since Joule heating drives deleterious stirring.

In the absence of ion gradients, the electric field is essentially independent of position and orthogonal to the electrodes. Additionally, one need not provide a detailed account of the ionic solutes.

Balance laws

Given these simplifying assumptions, the remaining conservation laws that apply are conservation of momentum and mass. The momentum balance is written in differential form, but is expressed in terms of an ensemble average, or bulk average, suspension velocity. This velocity is denoted **u** and, formally at least, is the local velocity at position **x** obtained by averaging over a representative volume element in the neighborhood of **x**. Note that the representative volume element encompasses both fluid and particles, so **u** is *not* the locally-averaged fluid

velocity. Formulated in this manner, the (dimensionless) momentum balance reads

$$\mathcal{R}\rho(\phi)\frac{D\mathbf{u}}{Dt} = -\nabla P + \mu(\phi)\nabla^2\mathbf{u} - \Lambda(1 - \phi)\hat{\mathbf{e}}, \qquad (1)$$

with

$$\nabla \cdot \mathbf{u} = 0, \qquad (2)$$

where: P is the dynamic pressure, t is the time, $\rho(\phi)$ and $\mu(\phi)$ are, respectively, the suspension density and viscosity normalized to their pure fluid values; and ϕ is the particle volume fraction scaled on c_0. Equation (1) is completely analogous to the suspension momentum balance used by Acrivos and Herbolzheimer[5] to substantiate PNK theory and applies as long as the particle Reynolds number $\mathcal{R}_p \equiv \rho_f v_0 a_p/\mu_f$ is small. Here a_p is the particle radius and v_0 is the characteristic velocity of the particles, which is their electrophoretic velocity v_e at a representative volume fraction in the suspension (e.g. c_0). Using typical values for the relevant quantities, one can show that $\mathcal{R}_p$ is $O(10^{-6})$. The magnitude of other dimensionless groups, as well as the scale factors, are summarized in Table 1.

The parameter Λ is $O(10^7)$. Consequently, whenever the (scaled) volume fraction deviates far from one, a strong buoyancy force results. It is this buoyancy force, which couples with the particle electrophoresis, to drive electrodecantation. The term $-\Lambda(1 - \phi)\hat{\mathbf{e}}$ represents a gravitational body force on the fluid; this body force vanishes when the

volume fraction of the suspension is equal to c_0 (i.e. when the scaled volume fraction $\phi = 1$).

Because the buoyancy force depends on the local volume fraction of particles, it is necessary to account for local variations in ϕ. This is done through a particle conservation relation, viz.

$$\frac{\partial \phi}{\partial t} + \mathbf{u}_p \cdot \nabla \phi = -\phi \nabla \cdot \mathbf{u}_s, \tag{3}$$

with

$$\mathbf{u}_s \equiv \mathbf{u}_p - \mathbf{u} = F(\phi)\hat{\mathbf{E}} = \text{electrophoretic slip velocity of particles} \tag{4}$$

In writing Eqn (3), two assumptions have been made. The first is that particle diffusion can be neglected. This requires that the Peclet number $\mathcal{P}$ be large. Here, the Peclet number is defined by $\mathcal{P} \equiv v_0 l / D_p$, where D_p is the particle diffusion coefficient and l is a characteristic macroscopic length in the system (e.g. the electrode height). Again, using typical values, $\mathcal{P}$ is $O(10^6)$. The second assumption is that the electrophoretic velocity of the particles is considerably larger than their Stokes sedimentation velocity. For silica or alumina particles in the 100 nm size range, the electrophoretic velocity exceeds the Stokes sedimentation velocity by a factor of roughly 500, assuming electrophoretic mobilities on the order 10^{-4} $cm^2/V \cdot sec$ at field strengths of 10 V/cm.

An important implication of Eqn (3) is that, unless there are significant volume fraction gradients in the suspension at the outset, volume fraction gradients can only develop as a result of events near the bound-

aries of the suspension. This can be seen by recognizing that, when there are no spatial gradients in ϕ, the time derivative $\partial\phi/\partial t$ vanishes.

Boundary layer analysis: particle depletion at an electrode

Because particle diffusion is negligible, the volume fraction variation propagates outward from the boundaries. In particular, the particles move away from the electrode at which they experience an electrostatic repulsion. This establishes a particle depleted region in which $\phi = 0$. In the bulk of the suspension, the particle volume fraction remains at $\phi = 1$. Without further analysis, it is not possible to predict the thickness of the depleted region. However, based on the Peclet number, one can estimate that the transition from the particle depleted region to the homogeneous bulk region occurs over a length scale that is small compared to l. More specifically, the thickness of this transition is $O(l/\mathcal{P})$, which is about the size of a single particle. From the macroscopic viewpoint, then, the suspension segregates into a particle depleted region and a homogeneous region (ignoring, for the time being, what happens at the other electrode), with a sharp transition from one region to the other.

As noted previously, the particle depleted region will experience a large buoyancy force, and this will drive the clear fluid layer upwards, causing it to flow along the electrode. To some extent, this rising clear layer is similar to a natural convection boundary layer that develops

adjacent to a vertical, heated plate. The buoyancy force on the fluid is balanced by viscous stresses which resist the motion of the fluid upwards. Additionally, continuity (or incompressibility) requires that the rising fluid must be replaced.

The resultant of these three effects: buoyancy, viscous stresses, and the need to replace the rising fluid, is that the particle depleted region does not grow indefinitely. In fact, on a time scale on the order of

$$\Lambda^{-1/3} l / v_0,$$

the depleted layer has ceased to grow and has established a steady arrangement. The layer ceases to grow after this short interval because the electrophoretic motion of the particles away from the electrode is balanced by the flow of fluid from the bulk suspension, which is required to replenish the fluid rising in the clear layer.

A detailed analysis of the particle depletion at the electrodes follows rather closely that of Acrivos and Herbolzheimer,[5] for sedimentation in tanks with inclined walls. Here we highlight the features of the analysis as they apply to electrodecantation and refer the reader to their work for a complete discussion.

The problem is best viewed from a Cartesian coordinate system local to the boundary layer (cf. Figure 3), with u, the velocity component parallel to the electrode surface, rescaled to account for the large body force. For the time being, we assume that the electrodes are set at an angle θ with respect to the gravity vector, though it will become

evident that the decantation rate is not a function of θ. Because buoyancy is balanced by viscous effects, u is $O(\Lambda^{1/3})$ and the thickness of the particle-free layer is $O(\Lambda^{-1/3})$. Thus we introduce the following stretched variables

$$\tilde{u} = \Lambda^{-1/3}u, \quad \tilde{y} = \Lambda^{1/3}y \qquad (5)$$

and express the position of the boundary between the suspension and the clear layer as

$$\tilde{y} - \tilde{\delta}(x,t) = 0. \qquad (6)$$

The function $\tilde{\delta}(x,t)$ must be determined from a kinematic condition that describes the development of the boundary between the fluid layer and the suspension, viz.

$$\Lambda^{-1/3}\frac{\partial\tilde{\delta}}{\partial t} + \tilde{u}\frac{\partial\tilde{\delta}}{\partial x} - v = 1. \qquad (7)$$

In contrast to the inclined sedimentation problem, the RHS of (7) is unity and this difference arises because the electrophoretic slip velocity of the particles is perpendicular to the electrode surface, assuming the electrodes are flat. The form of (7) indicates that time may be rescaled according to $\tilde{t} = \Lambda^{1/3}t$ and that a steady configuration for $\tilde{\delta}(x,\tilde{t})$ will obtain on a time scale of $O(\Lambda^{-1/3}l/v_0)$, as will be seen.

The velocity components that appear in the kinematic condition follow from the boundary layer solutions to Eqns (1) and (2). In the boundary-layer, the x-component of the momentum balance reads

$$\frac{\partial^2\tilde{u}}{\partial\tilde{y}^2} + \cos\theta = 0 + O(\mathcal{R}\Lambda^{-1/3}, \Lambda^{-1/3}), \qquad (8)$$

with

$$\tilde{u} = 0 \quad \text{at} \quad \tilde{y} = 0, \tag{9}$$

and

$$\partial \tilde{u}/\partial \tilde{y} = o(1) \quad \text{at} \quad \tilde{y} = \tilde{\delta}. \tag{10}$$

In writing (9), we have assumed the electrode is a no-slip boundary. The RHS of the no-stress condition at $\tilde{y} = \tilde{\delta}$ is $O\{[(\rho(1)\mathcal{R}/\mu(1)]^{1/2}\Lambda^{-1/6}\}$ for inclined sedimentation, and similar arguments apply here. The solution for $\tilde{u}$ is thus

$$\tilde{u} = \left(\tilde{y}\tilde{\delta} - \frac{1}{2}\tilde{y}^2\right)\cos\theta + o(1). \tag{11}$$

The fluid motion is two-dimensional and the y-component of the velocity can be obtained from continuity, since $\partial v/\partial \tilde{y} = -\partial \tilde{u}/\partial x$. If the electrode surface is taken to be impenetrable to the flow,

$$v = -\frac{1}{2}\tilde{y}^2\frac{\partial \tilde{\delta}}{\partial x}\cos\theta + o(1). \tag{12}$$

When Eqns (11) and (12) are combined with (7), the kinematic condition for $\tilde{\delta}$ becomes

$$\Lambda^{-1/3}\frac{\partial \tilde{\delta}}{\partial t} + \tilde{\delta}^2\cos\theta\frac{\partial \tilde{\delta}}{\partial x} = 1. \tag{13}$$

By the method of characteristics, one can show that Eqn (13) gives

$$\tilde{\delta} = \begin{cases} \tilde{t}, & \text{for} \quad \tilde{t} < \tilde{t}_* = (3x/\cos\theta)^{1/3} \\ (3x/\cos\theta)^{1/3} & \text{for} \quad \tilde{t} \geq \tilde{t}_* \end{cases} \tag{14}$$

if one assumes that $\tilde{\delta}$ tends to zero as $x \to 0$ (i.e. at the leading edge of the electrode). According to (14), the depleted layer a distance x

from the leading edge of the electrode, grows linearly with time for an interval $\bar{t}_*$, and thereafter growth stops. Based on typical values for Λ, the electrophoretic velocity, and the electrode dimensions (cf. Table 1), the boundary layer develops in approximately $\Lambda^{-1/3}l/v_0 = 50$ sec and is of thickness $O(\Lambda^{-1/3}l) = 0.5$ mm.

Some Implications of the Boundary Layer Analysis

The preceding boundary layer analysis has several important implications for electrodecantation, including:

1. The clear layer is thin compared to the macroscopic dimensions of a separation chamber, but still large compared to the particle size. Provided the rising boundary layer is stable and folds onto the top of the suspension, one can decant clear fluid to the top of the chamber. The rise of the clear fluid sets the core of the suspension in motion, but to the level of approximation employed here, Acrivos and Herbolzheimer show that motion within the core of the suspension has little influence on the particle distribution. As a consequence, the suspension is forced downward and particles concentrate at the chamber bottom.

2. When coupled with the existence of a clear fluid layer, an important result of the particle conservation relationship is the following. Let $h(t)$ denote the height of the suspension above the bottom of

the electrode. Further, let l be the height of the electrode, b the electrode-to-electrode separation, and t the (dimensional) time. The divergence theorem can be applied to Eqn (3) to obtain

$$h(t) = l \exp\left(-\frac{v_0}{b}t\right),$$ (15)

if one ignores the regions of the chamber outside of the electrode gap. The thickness of the clear layer on the top of the suspension will therefore grow as

$$l - h(t) = l\left[1 - \exp\left(-\frac{v_0}{b}t\right)\right]$$ (16)

and, unlike inclined settling, is unaffected by the tilt of the electrode surfaces.

3. The clear layer develops quickly compared to b/v_0, the time required for a particle to migrate electrophoretically across the electrode gap. Nevertheless, during this brief period, one can expect that some particles will deposit on the electrode toward which they are driven. Particle buildup on this 'other' electrode must be controlled or suppressed, if the desire is to effect a solid/liquid separation and concentrate particles on the chamber bottom. Particle deposition will also affect the applied electric field and, presumably, alter the process dynamics. As will be seen, periodic reversal of the electrode polarities can be used to control particle buildup at the electrodes without substantially altering the clearing rate

of the suspension. This practical measure suffices so long as the period of reversal is long compared to the time scale for boundary layer development, but short compared to b/v_0.

Methods

General experimental scheme

Electrodecantation experiments were performed in a Plexiglas container depicted in Figure 2. Three liters of suspension (see below) were placed into the electrodecantation chamber; at the inception of the experiment, the suspension was milky-white. Two 304 stainless steel, wire-mesh electrodes were immersed in the suspension in a vertical orientation; the bottom of each electrode was positioned 11.5 cm beneath the surface. The steel wire of the mesh was 0.24 mm in diameter, with 15.75 × 15.75 wires/cm and spacing between wires of 0.41 mm; the electrodes were 10 cm wide. The electrodes were placed 11cm apart and were connected to a manual switching device, which in turn was connected to a Hewlett Packard 6634A system DC power supply (Hewlett Packard, CA). The switching device was used to periodically reverse the polarity of the electric field in some of the experiments. An electric field was applied to the suspension, which was monitored visually for the appearance of a clear fluid layer, such as that depicted in Figure 1. The depth of the clear layer was observed to increase with time and was measured with a ruler at various stages of development. The time since the intial application of the electric field was also recorded. The experiments were typically continued until the lower boundary of the clear layer approached the bottom of the electrodes. The electrical current was recorded from the power supply at the start and completion of the experiment. At the end of each experiment, turbidity, conductivity, and pH measurements were taken on samples from the top clear layer, bottom layer of concentrated solids, and bottom six sample ports, as indicated on Figure 2 (cf. Table 2 for the port positions). Turbidity measurements were performed on 5-ml samples

diluted ten fold with water and converted to concentrations using calibration curves for each of the suspensions. Samples of 50 ml were used for the conductivity and pH tests. Temperature measurements were performed before and after the experiment using a mercury thermometer. No change in temperature was observed.

Suspension preparation and particle characterization

Monodisperse stock suspensions (approx. 3 liters ea.) were made from either amorphous fumed silica (Cabot Corp, IL) or α-alumina (Degussa, OH) dispersed in distilled water at the following volume fractions: 0.013, alumina stock; 0.019, silica stock. The distilled water originated from a Milli-Q water system (Millipore, MA) at pH 5.7 and electrical conductivity of 1.0 μS/cm. Portions of these stock solution were subsequently diluted with distilled water to produce 3 liters of starting suspension for each of the electrodecantation experiments described above. The concentration of these starting suspensions was determined from turbidity measurements; stock suspension volume fractions were determined by drying 5 ml of stock in a laboratory oven.

To breakup aggregates, suspensions were sonicated for 5 minutes with a model W-375 sonicator/cell disruptor (Heat Systems-Ultrasonics Inc., NY). Particle size measurements were performed on a Coulter N4 particle size analyzer (Coulter Corp., FL). The silica (SiO_2) and alumina (Al_2O_3) particles were found to have mean diameters of 189 $\pm$ 1.4 nm and 203 $\pm$ 2.0 nm, respectively.

A 50-ml sample was taken from the dispersed starting suspension for turbidity, conductivity, and pH measurements. These measurements were taken with a Hach Ratio/XR Turbidimeter (Hach Company, CO), Orion model 122 handheld conductivity meter with the standard probe (Orion Research Inc., MA), and an Orion model 701A digital ion analyzer pH meter (Orion Research Inc., MA), respectively.

Electrophoretic mobility measurements were made with a Lazer Zee Meter, Model 501, (Pen Kem, Inc., NY) on particles in suspensions diluted to approximately 0.01w% solids. Samples were diluted with distilled water and pH was manipulated by adding

small amounts of KOH or HNO_3. Mobility measurements were also taken in 5-mM KCl, with the pH manipulated by the addition of KOH or HCl; within experimental error, these data were the same as those obtained on diluted distilled water suspensions.

Results and Discussion

The principal results of the electrodecantation experiments are given in Figure 4, where $h(t)/l$ is shown as a function of scaled time $v_0 t/b$ for three independent sets of experiments. The characteristic velocities used to scale the time were calculated from the nominal electric field strength and the mobility vs. pH data shown in Figure 5, i.e. $v_0 = \mu_e E$. Also shown on Figure 4 are the predictions of Eqn (15). While it is obvious that the model grossly overpredicts the decantation rate, these data suggest considerable agreement with the theory.

Firstly, the data scale as predicted for experiments that were performed under substantially different conditions; e.g., the SiO_2 particles are negatively-charged, the Al_2O_3 particles are positively-charged, and within experimental uncertainties, the results overlap.

Second, the model is predicated on the idea that the clear layer stems from a particle-free boundary layer adjacent to one of the electrodes. With l/b of $O(1)$, the boundary layer is established on a time scale of $O(\Lambda^{-1/3} b/v_0)$, which is short compared to the predicted growth rate of the clear layer on top of the suspension. Therefore, periodically switching the polarity of the applied field should not dramatically affect the temporal decrease of $h(t)$, provided the period of polarity switching is long compared with $\Lambda^{-1/3} b/v_0$. To obtain the data of Figure 4, one set of Al_2O_3 experiments was done with a steady field of 0.45 V/cm, and another was performed in a field of 7.3 V/cm with the polarity switched every 4 min; the SiO_2 experiments were done with the polarity switched every 30 min. In each instance, the period of switching exceeded $\Lambda^{-1/3} b/v_0$ by at least a factor of 15, and there was no apparent effect on the decantation rate. A

related series of experiments (data not shown), yielded no electrodecantation when the electrodes were forced with an AC frequency of 60 Hz.
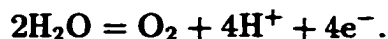
Finally, at longer times, the decantation rate goes over to that predicted by the theory. A line fit through the data for $v_0 t/b \geq 3.75$ has a slope of -0.42, whereas Eqn (15). gives a slope of $-1/e \doteq -0.43$ on the semi-$\log_{10}$ scale.

The discrepancy between theory and experiment, as depicted in Figure 4, may be due to any or all of several factors, beginning with the role of the electrodes. In developing Eqn (15), the electrodes were taken to be flat, rigid surfaces, which allowed for the application of a uniform electric field throughout the volume of the electrodecantation cell. The electrodes employed in the experiments were stainless steel wire mesh, inserted 11.5 cm into the suspension and displaced from the chamber walls, as depicted in Figure 2. The steel wire diameter (0.24 mm) and mesh spacing (0.41 mm) are comparable to $l/\Lambda^{1/3} \doteq 0.5$ mm, the thickness of the predicted particle-free boundary layer. Thus in all likelihood, the electric field is not uniform and perpendicular to the vertical plane of the electrodes; nor is it evident that the no-slip condition will obtain.

In addition to these geometric considerations, further evidence that there are spatial variations of the electric field is given in Table 3, where conductivity and pH changes are listed as a function of vertical position. The data depict the situation after a period of electrodecantation. The initial formulation, pH and conductivity of the suspensions indicate that H^+ ions are one of the significant charge-carrying species. Over the course of an experiment, H^+ ions are consumed at the cathode, e.g.

$$2H^+ + 2e^- = H_2,$$

while at the anode, H^+ ions are generated, e.g.

$$2H_2O = O_2 + 4H^+ + 4e^-.$$

Since SiO_2 particles are repelled from the cathode, a rising particle-free layer would convect higher pH and lower conductivity fluid to the top of silica suspensions. Conversely, Al_2O_3 particles are repelled from the anode, and this would cause lower pH and

higher conductivity fluid to rise to the top of alumina suspensions. The consequent pH and conductivity gradients are qualitatively consistent with those reported in the table, and because the measured changes are significant, it seems reasonable to conclude that the electric field varies substantially with position in the chamber.

These data for the alumina suspension also show that, beneath the superposed clear layer, c/c_0 is not unity—though there is a visibly sharp transition from clear fluid to particle-laden suspension. The data in Figure 6 illustrate that $\phi \equiv c/c_0$ diminishes continuously at port 6 until $v_0 t/b \doteq 2.4$, at which time $h(t)$ reaches the sample port. Similar results were obtained with silica particles, implying that the core of the suspension between the electrodes is altered as the decantation proceeds. Electrophoretic mobility and particle size distributions, measured before and after electrodecantation, showed no significant alteration of the particle surface charge and no aggregation. Changes in particle concentration were also observed to cease upon removal of the electric field. This suggests that gradients within the core are not caused by sedimentation of aggregates that result from coagulation of the particles. Moreover, the invariance of the scaled decantation rate to an order of magnitude change in the nominal field strength, as well as temperature measurements taken on the suspension, imply that Joule heating is not involved.

The concentration changes in the core may be due to instability of the particle-free boundary layer, which is susceptible to travelling-wave instabilites for inclined settlers[8]. For example, Herbolzheimer[9] observed travelling waves in inclined settlers for which $\Lambda^{1/3} \doteq 250$, $\mathcal{R}\Lambda^{-1/3} \leq 0.1$, and $l/b \doteq 10$; for the electrodecantation experiments $\Lambda^{1/3} \doteq 215$, $\mathcal{R}\Lambda^{-1/3} \doteq 0.05$ and $l/b \doteq 1$. Should they be present, the travelling waves would re-intrain particles from the core, in effect disrupting the sharp transition from the boundary-layer to the suspension. Gentle stirring due to buoyancy-driven motion at the electrodes would tend to fold this disrupted, or blurred, transition region onto the core and produce a gradual stratification of the suspension between the electrodes. It would also retard the development and growth-rate of the clear fluid layer atop the

core.

In view of the conductivity and pH gradients that develop, electrical stresses, which have been omittted from the present analysis, probably influence the base state and stability of the particle-free boundary layer. The electrical stresses are $O(\epsilon\epsilon_0 E^2)$, where ϵ_0 is the permittivity of free space and ϵ is the relative permitivity of the suspension. For $\epsilon = 80$, $10^{-6} < \epsilon\epsilon_0 E^2 < 4 \times 10^{-4}$ N/m^2. While this certainly exceeds the nominal stress scale (cf. Table 1), the viscous stresses are $O(\Lambda^{2/3}\mu_f v_0/l) \doteq 4 \times 10^{-3}$ N/m^2 in the particle-free boundary layer. As one moves from the boundary layer into the suspension, the buoyancy and viscous effects diminish as the particle volume fraction increases from zero. One might anticipate, then, that in a region beyond the particle-free boundary layer, electrical stresses compete with the buoyancy and viscous effects, and this may contribute to the vertical gradients summarized in Table 3, as well as to the continuous decrease in ϕ shown in Figure 6. To investigate the existence and structure of such a region, one must employ a more complete description of the ion transport, and so this is a matter for subsequent study.

Literature Cited

(1) Bier, M. Preparative Electrophoresis without Supporting Media. In *Electrophoresis: Theory, Methods and Application*; Bier, M. Ed.; Academic Press: New York, 1959; pp 263-315.

(2) Kirkwood, J.G.; Cann, J.R.; Brown, R.A. The Theory of Electrophoresis-Convection. *Biochim. Biophys. Acta* **1950**, *5*, 301.

(3) Adolf, M.; Pauli, W. *Biochem. Z.* **1924**, *152*, 360. Untersuchungen an Elektolytfreien, Wasserloslichen Proteinkorpern.

(4) Blank, F; Valko, E. Das Schichtugsphanomen bei der Elektrodialyse als Eleckrophoretische Erscheinung. *Biochem. Z.* **1928**, *195*, 220.

(5) Acrivos, A.; Herbolzheimer, E. Enhanced Sedimentation in Settling Tanks with Inclined Walls. *J. Fluid Mech.* **1979**, *92*, 435.

(6) Larson, I.; Drummond, C.J.; Chan, D.Y.C.; Grieser, F. Direct Force Measurements between Silica and Alumina. *Langmuir* **1997**, *13*, 2109.

(7) Nir, A.; Acrivos, A. Sedimentation and Sediment Flow on Inclined Surfaces. *J. Fluid Mech.* **1990**, *212*, 139.

(8) Shaqfeh, E.S.G.; Acrivos, A. Enhanced Sedimentation in Vessels with Inclined Walls: Experimental Observations. *Phys. Fluids* **1987**, *30*, 1905.

(9) Herbolzheimer, E. The stability of the flow during sedimentation beneath inclined surfaces. *Phys. Fluids* **1983**, *26*, 2043.
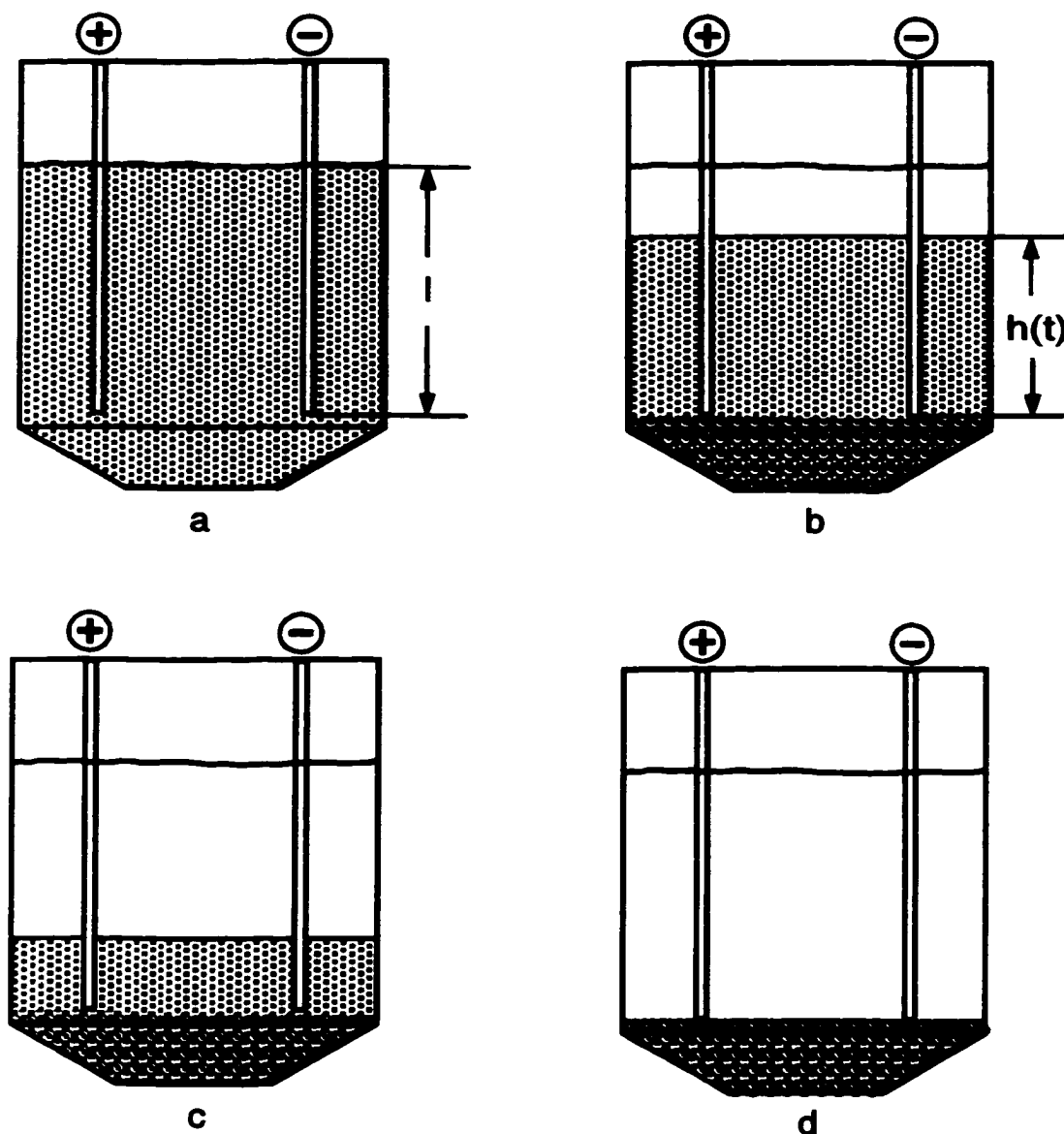
Figure 1. The qualitative features of batch electrodecantation of stable colloidal dispersions. a. a uniform dispersion at the inception of the experiment. b. a clear layer forms atop a particle-laden region, particle concentration increases beneath the electrodes. c. the clear layer grows with time. d. the end of the experiment: the clear layer reaches the bottom of the electrodes and continued application of the field produces little subsequent change. The initial height of the suspension above the bottom of the electrodes is denoted l (panel a); $h(t)$ indicates the suspension height at subsequent times t (panel b).
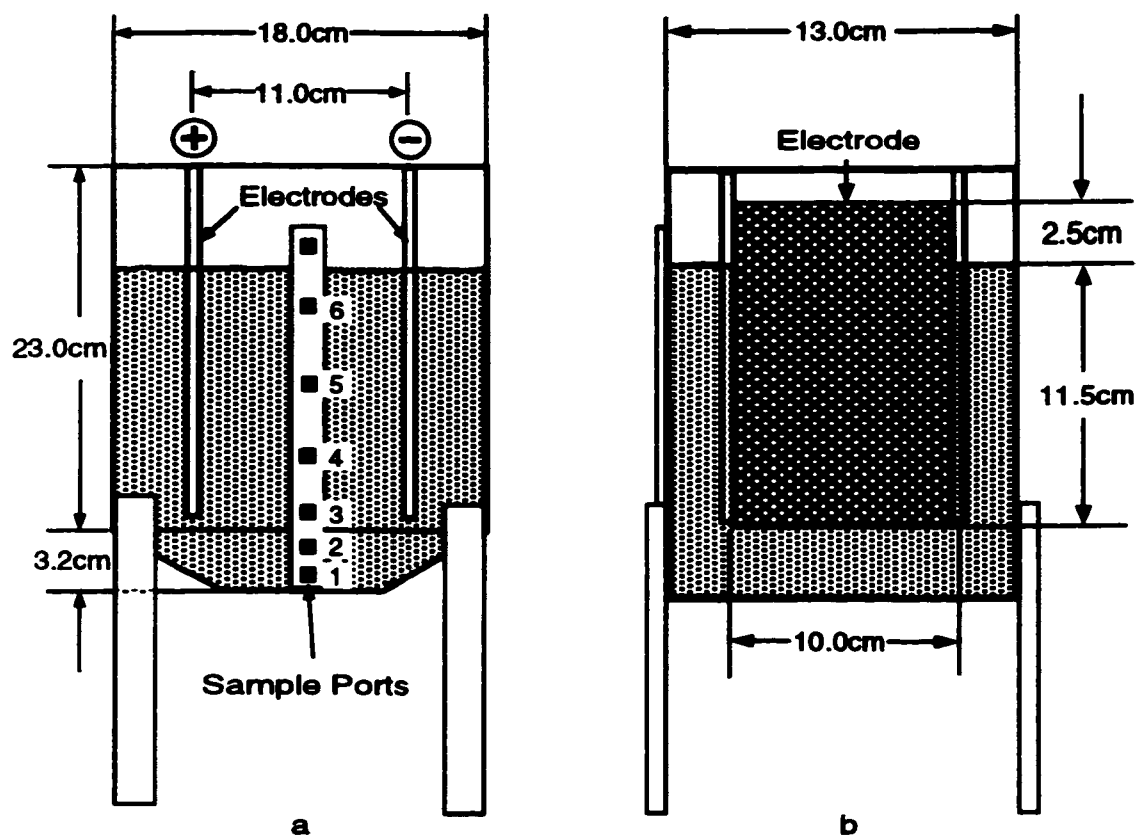
Figure 2. Electrodecantation chamber. a. front view. b. righthand side view.
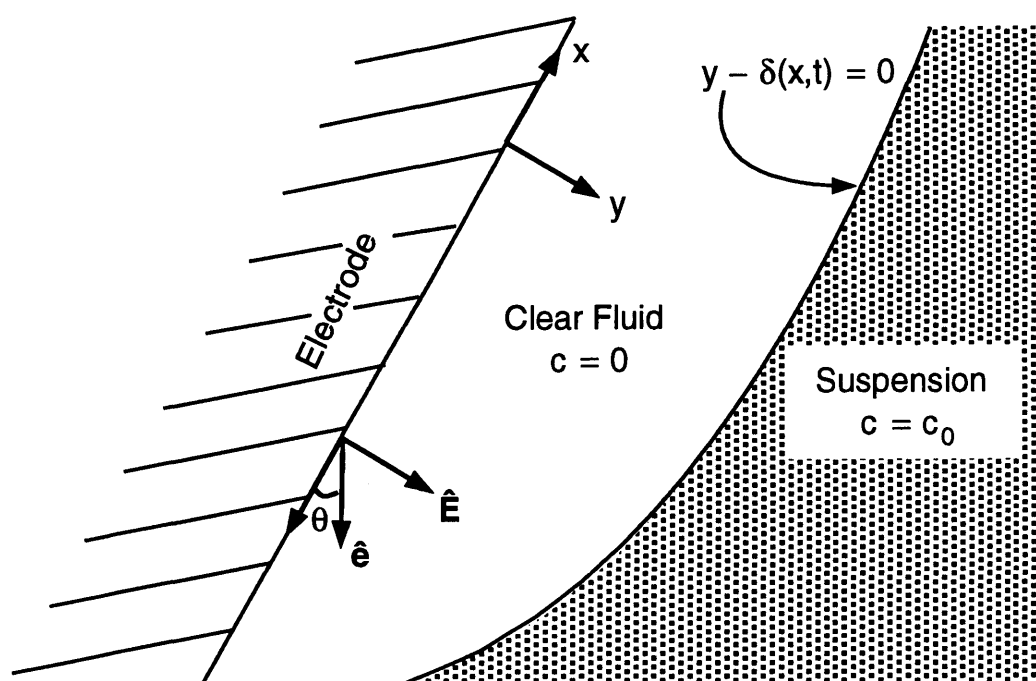
Figure 3. Definition sketch: boundary layer of particle-free (clear) fluid at an electrode.

Figure 4: The normalized height of the suspension h/l versus dimensionless time $v_0 t/b$. Data are shown on a semi-log$_{10}$ scale and the height of the suspension is reckoned from the bottom of the electrodes; l = 11.5 cm and b = 11 cm. Legend: □, SiO_2, $c_0 = 2.3 \times 10^{-3}$, $\mu_e = -2.8 \times 10^{-4}$ $cm^2/V \cdot s$, nominal $E = 7.3 \, V/s$ with polarity switched every 30 min; o, SiO_2, $c_0 = 2.3 \times 10^{-3}$, $\mu_e = -2.8 \times 10^{-4}$ $cm^2/V \cdot s$, nominal $E = 9.8 \, V/s$ with polarity switched every 15 min; ■, Al_2O_3, $c_0 = 1.3 \times 10^{-3}$, $\mu_e = 4.2 \times 10^{-4}$ $cm^2/V \cdot s$, nominal $E = 7.3 \, V/s$ with polarity switched every 4 min; ♦, Al_2O_3, $c_0 = 1.3 \times 10^{-3}$, $\mu_e = 4.2 \times 10^{-4}$ $cm^2/V \cdot s$, nominal $E = 3.9 \, V/s$ with polarity switched every 30 min; •, Al_2O_3, $c_0 = 9.7 \times 10^{-4}$, $\mu_e = 4.2 \times 10^{-4}$ $cm^2/V \cdot s$, nominal $E = 0.45 \, V/s$ with no polarity switching. The solid line is Eqn (15). The dashed line is the best-fit to the data for $v_0 t/b > 3.75$.

140
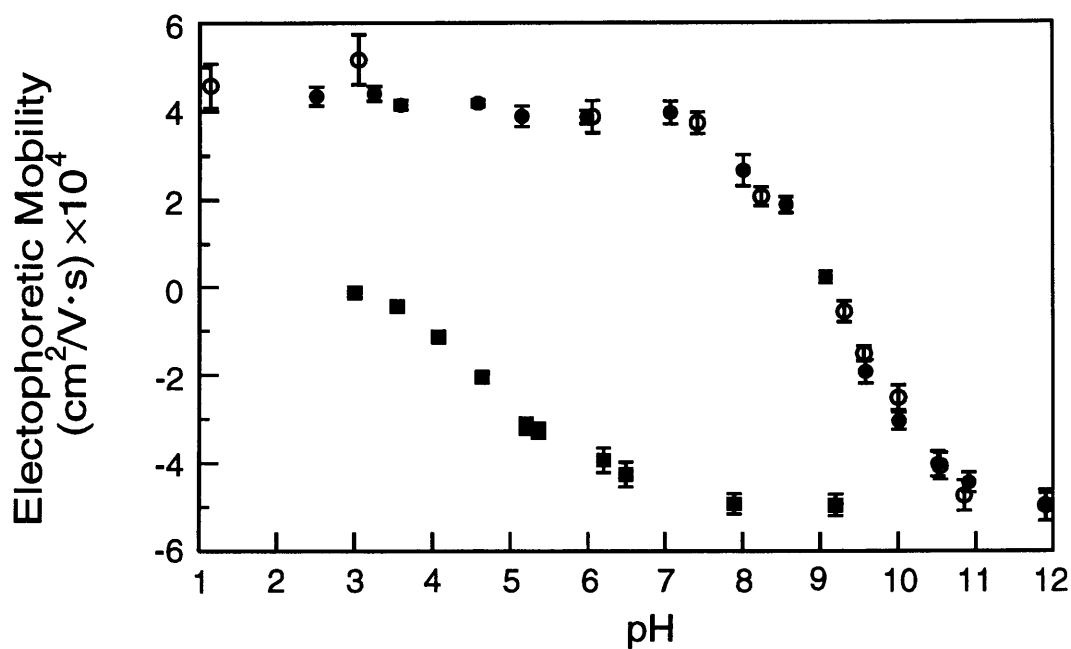
Figure 5. Electrophoretic mobilities as a function of pH. Legend: ○, 203 nm alumina particles in 5 mM KCl, pH adjusted by adding small amounts of HCl or NaOH; ●, 203 nm alumina particles in distilled water, pH adjusted by adding small amounts of KOH or HNO_3; ■, 189 nm fumed silica particles in distilled water. pH was raised by adding small amounts of KOH or HNO_3. Error bars represent one standard deviation on either side of the mean.
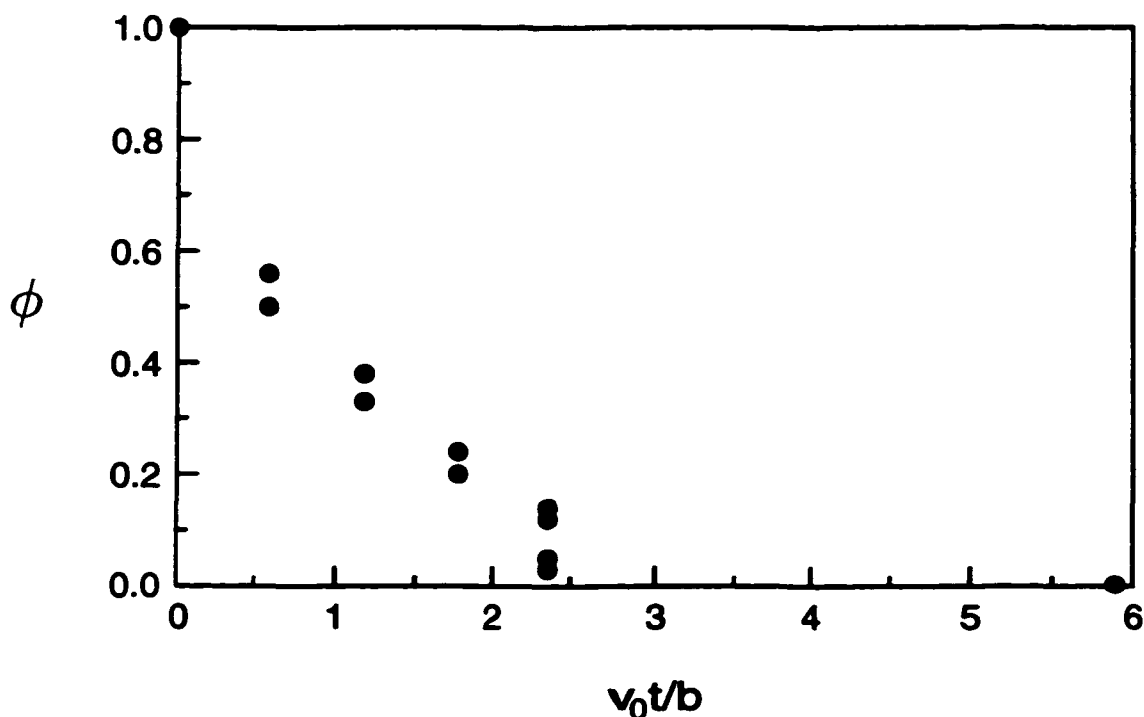
Figure 6. Scaled volume fraction ϕ as a function of dimensionless time $v_0 t/b$ for alumina dispersed in Milli-Q water. Each datum represents an individual electrodecantation experiment. The initial volume fraction c_0 ranged from 7.6×10^{-4} to 1.6×10^{-3} in the experiments. These small variations in the starting conditions had an insignificant effect on the inital pH (approx. 4.2) and electrical conductivity of the suspension (approx. 20 μS/cm). 5ml-samples were taken 2.5cm from the top of the suspension through port 6 at the time indicated. The nominal $E = 7.3$ V/cm, with the electrode polarity switched every 2 minutes, except for the data point at dimensionless time of approximately 5.8 (switched every 4 minutes).

Table 1: Representative values for parameters, scale factors, and dimensionless groups.

	Magnitude[a]
Parameter	
a_p, particle radius	1 to 2 $\times$ 10^{-7} m
ρ_p, particle density	2 to 4 $\times$ 10^3 kg/m^3
D_p, particle diffusion coefficient	2 $\times$ 10^{-12} m^2/sec
μ_e, particle electrophoretic mobility	2 to 4 $\times$ 10^{-8} m^2/V·sec
E, electric field strength	100 to 1000 V/m
σ, electrical conductivity	1 to 2 $\times$ 10^{-3} S/m
Scale factor	
c_0, concentration	initial volume fraction of particles, 10^{-3}
v_0, velocity	electrophoretic velocity $v_e(c_0)$, 10^{-5} m/sec
l, length	electrode height, 10^{-1} m
l/v_0, time	10^4 sec
$\mu_f v_0/l$, stress	10^{-8} to 10^{-7} N/m^2
Dimensionless group	
$\mathcal{R}$, Reynolds number	$\rho_f v_0 l/\mu_f$, $O(1)$
Λ, Grashof over Reynolds number	$l^2 g(\rho_p - \rho_f)c_0/\mu_f v_0$, $O(10^7)$
$\mathcal{P}$, Peclet number	$v_0 l/D_p$, $O(10^6)$
$\mathcal{R}_p$, particle Reynolds number	$\rho_f v_0 a_p/\mu_f$, $O(10^{-6})$
$\mathcal{P}_p$, particle Peclet number	$v_0 a_p/D_p$, $O(1)$

Table 2: Relative vertical position (cm) of sample ports.

	above chamber bottom	beneath air-water interface	from bottom of electrodes
port 6	12.0	2.5	9.0
port 5	9.0	5.5	6.0
port 4	6.2	8.3	3.2
port 3	4.1	10.4	1.1
port 2	3.1	11.4	0.1
port 1	1.3	13.2	-1.7

Table 3: Stratification of pH, electrical conductivity and particle concentration.

	SiO_2[a]			Al_2O_3[b]		
	c/c_0	σ/σ_0	ΔpH[c]	c/c_0	σ/σ_0	ΔpH[c]
port 6	0.00	0.40	1.45	0.00	3.35	−0.88
port 5	0.00	0.58	1.12	0.25	1.98	−0.67
port 4	0.00	0.54	1.52	0.53	1.27	−0.45
port 3	0.00	0.61	0.82	0.84	0.82	−0.11
port 2	0.03	5.96	−0.47	1.12	0.81	0.75
port 1	11.1	5.93	−0.48	5.58	1.08	1.45
bottom	12.4	6.32	−0.48	11.9	1.14	1.43

[a]Conditions at the end of 7 hrs of electrodecantation with 80 V applied across the electrodes; polarity switched every 30 min; $c_0 = 2.3 \times 10^{-3}$; $\sigma_0 = 5.7$ μS/cm; initial pH, 4.44; initial current, 5.5 mA; final current, 9.3 mA.

[b]Conditions at end of 3 hrs of electrodecantation with 80 V applied across the electrodes; polarity switched every 2 min; $c_0 = 0.9 \times 10^{-3}$; $\sigma_0 = 18.2$ μS/cm; initial pH, 4.09; initial current, 20 mA; final current, 48 mA.

[c] ΔpH $= p$H$_{final} - p$H$_{initial}$.

APPENDIX C: Measurements on the Diffusion coefficient of colloidal Particles by Taylor-Aris Dispersion

This manuscript has been published in the *Journal of Colloid and Interface Science*, (**195**, 19–31, 1997) and is reproduced here with kind permission from Academic Press.

Measurements on the Diffusion Coefficient of Colloidal Particles by Taylor–Aris Dispersion

B. M. Belongia and J. C. Baygents[1]

Department of Chemical and Environmental Engineering, The University of Arizona, Tucson, Arizona 85721

Taylor–Aris dispersion in narrow-bore capillaries is used to measure the diffusion coefficient of colloidal particles in aqueous suspension. The method is shown to yield accurate results for particles up to about 0.3 μm in diameter; the measurement time for larger particles is prohibitively long and impractical. For hydrophobic particles, interactions with the capillary walls can introduce error into the interpretation of the data. The measurements also suggest that buoyancy-driven particle motion can introduce error. Consequently, a method similar to capillary hydrodynamic fractionation was developed to establish when these factors were of negligible effect. The results constitute an order-and-a-half improvement in the sensitivity of the technique, which has been recently shown to work for nanometer-sized proteins. The data suggest that, when matched with the appropriate theory, dispersion in capillaries may be a useful probe of colloidal and gravitational interaction potentials. © 1997 Academic Press

Key Words: Brownian motion; capillary hydrodynamic fractionation; capillary electrophoresis; colloidal dispersions.

INTRODUCTION

The Brownian motion of colloidal particles is a fundamental process of considerable interest owing to, among other things. its role in the coagulation and rheology of dispersions. the attachment of particles to surfaces, and the transport and fate of particles in a variety of multiphase flows, for example. membrane and filtration processes and contaminant transport in the atmosphere and in saturated groundwater. As a result, many techniques are available to determine the diffusion coefficient of particles, including spin–echo NMR (1, 2), ultracentrifugation (3), and dynamic light scattering (4. 5). Here we describe the implementation of Taylor–Aris dispersion (6–8), a technique that has typically been used to measure the diffusivities of molecular solutes (e.g. phenols (9)), as well as mutual diffusion coefficients in binary solutions (10).

The theory of Taylor–Aris dispersion is well-developed (11. 12), and moreover, the technique is conceptually similar to that of a simple one:

ple: a bolus of sample is introduced into a cylindrical capillary and eluted past a detector. where the spatiotemporal distribution of the solute is measured and converted into a diffusivity. However, if a and D respectively denote the radius of the capillary and the diffusivity of the analyte. and if t_R is the mean time for the analyte to reach the detector. accurate interpretation of the detector signal requires that the quantity Dt_R/a^2 be, in some sense. large. Historically this requirement has meant that the method is impractical for colloidal-sized particles larger than 10 nm. since a^2/D $\geq$ 85 min for $a \geq 0.05$ mm. Fortunately. long (ca. 1 m), narrow-bore (≤ 100 μm diameter) capillaries are now routinely available at a reasonable cost. due in part to the growing utility of capillary electrophoresis (13). Using such capillaries. Bello *et al.* (14) have recently shown that the Taylor–Aris method works well for proteins. In fused-silica capillaries of diameter 75 to 100 μm. diffusion coefficients within 1% of accepted values were obtained for proteins with Stokes radii on the order of 0.35 nm. In smaller-bore capillaries (diameters ≤ 75 μm). interactions between the analytes and the capillary walls were sufficient to introduce 3.5 to 4.5% error into a classical Taylor–Aris interpretation of the data for the 0.35 nm proteins. To mitigate the effects of analyte–wall interactions. measurements were also performed in 75 μm capillaries coated with polyacrylamide–dextran. These data were accurate to within 2% for proteins with Stokes radii as large as 3.5 nm. i.e. diffusion coefficients as low as 7×10^{-7} cm^2/s.

Here we examine the extent to which the Taylor–Aris dispersion technique can be used to measure the diffusivities of larger species (i.e. colloidal particles). whose diffusivities are considerably smaller than those of proteins and for which wall interactions might be significant. We also address a related question left unanswered by Bello *et al.* That is. in the absence of tabulated values, when can one have confidence in the measurement?

We have found that, with an experimental arrangement quite similar to that used for capillary electrophoresis. classical Taylor–Aris dispersion can be used to accurately measure the diffusion coefficients of colloidal particles as large as 0.27 μm in diameter. In principle the technique will work

for larger particles, too, but the measurement times become prohibitively lengthy since larger diameter capillaries are required to suppress interactions with the walls.

The particles analyzed were tobacco mosaic virus (TMV), hydrophobic and hydrophilic polystyrene (PS) spheres, and hydrophobic polymethyl methacrylate (PMMA) spheres. The diffusivities thus obtained were found to agree well with those determined independently by photon correlation spectroscopy. In some instances, the combined effects of gravitational body forces and interactions between the particles and the capillary walls were sufficient to bias the measurement significantly (10 to 20%, or more). Consequently, we found it useful to establish guidelines indicating how one might know when the data were reliable. This was done by performing experiments similar to the Taylor–Aris measurements, except the sample was doped with a small amount of a tracer solute, mesityl oxide. By examining the difference in the mean residence times of the analyte particles and the tracer solute, we found that one could assess whether the particle distribution is reasonably uniform over the capillary cross-section, as is required by the classical Taylor–Aris theory at times much greater than a^2/D (6–8, 12). More specifically, if the difference in residence times was less than about one-third of the standard deviation in the particle residence time, then the Taylor–Aris method yielded accurate diffusivities.

The presentation that follows begins with an overview of the experimental scheme. Thereafter the details of the measurements and their results are described. The paper concludes with a discussion of the utility of the method and some comments concerning the possibility of probing colloidal and gravitational interaction potentials by measuring particle dispersion in capillaries.

MATERIALS AND METHODS

General Experimental Scheme

A Beckman capillary electrophoresis system (P/ACE 2100) was used to carry out the dispersion experiments. The features of the device that were employed are depicted schematically in Fig. 1.

Each experiment consisted of the following steps: column prerinse; sample injection; imposition of a pressure gradient to elute the sample past a UV detector; and postrinse to clean the capillary. With the exception of sample injections, flows were driven through the capillary by the imposition of a pressure drop induced with the pressure solenoid. Buffer, wash, and sample solutions were introduced into the capillaries from 5 mL vials placed in an automated sampling carousel. The prerinse consisted of two to three pore volumes of carrier buffer forced through the capillary to ensure that the capillary was equilibrated to the carrier buffer. Next, a sample plug was injected into the column by applying an electric field along the capillary for 5 to 30 s; this method of introduction is known as electrokinetic injection. After
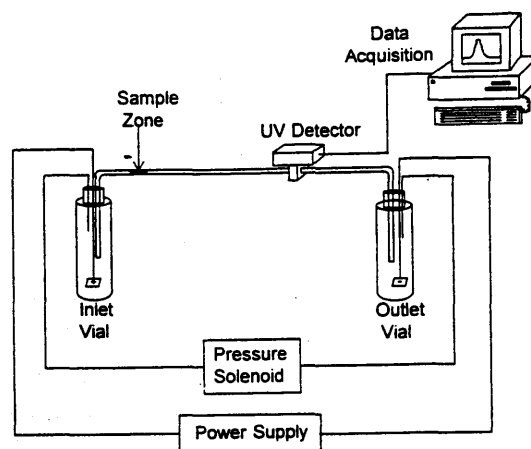

FIG. 1. Schematic of the experimental system.

the sample was introduced, carrier buffer was pushed through the capillary to drive the plug of sample past a UV lamp set at a wavelength of 214 nm. An absorbance detector with a 200 μm wide aperture was used to record the changes in absorbance as the sample zone passed a window burned in the column 7 cm from the outlet. The data recorded by the UV detector were then transferred to a personal computer and stored; a typical output recorded during the dispersion experiments is shown in Fig. 2. Finally, to eliminate the buildup of residue, the capillary was washed with a postrinse.

Two types of capillaries were used in the experiments: coated and uncoated. The postrinse for the uncoated capillaries consisted of separate washes with 0.1 N NaOH and Milli-Q water (Millipore Corp., Bedford, MA), each for two to three pore volumes; the coated capillaries were rinsed with Milli-Q water for four to six pore volumes. The Milli-Q water had a conductivity of 0.3 μS/cm. Throughout the experiments, the P/ACE 2100 circulated coolant through the cartridge containing the capillaries to maintain a constant temperature of 25°C (see Fig. 3).

The data were then fit with a Gaussian curve, and from the equation parameters, the first and second moments were determined (11, 14). After the first and second moments were corrected for the width of the initial sample zone and the detector aperture, the diffusion coefficients of the sample were calculated (11). As noted, the length of the detector aperture was 200 μm, and the width of the electrokinetically-injected sample zone was determined from the electroosmosis rate of the fluid along with the duration and strength of the applied electric field. The electroosmosis rate for each column was determined as described below.

Sample Preparation

Four kinds of particles were studied, viz. TMV, hydrophobic PMMA spheres, and hydrophobic and hydrophilic PS spheres.

Tobacco mosaic virus (TMV) was obtained from American Type Culture Collection (Rockville. MD) suspended in 10 mM sodium phosphate buffer (pH 7.2) at a concentration of approximately 1 mg/ml. To ensure that the TMV was equilibrated to the 2 mM carrier buffer. the TMV suspension was passed through a PD-10 gel filtration column containing G-25 Sephadex (Pharmacia. Piscataway. NJ). The TMV was eluted from the column with the appropriate carrier buffer (described below) and diluted with the same buffer to a final concentration of 0.1 mg/ml. The samples were then allowed to sit overnight before use.

The hydrophilic particles studied were carboxylate-modified polystyrene latex spheres. 0.19 and 0.83 μm diameter (Interfacial Dynamics Corp.. Portland. OR). obtained at concentrations of approximately 4% solids. Two types of hydrophobic particles were also studied: carboxyl charge-stabilized polystyrene latex spheres. 0.27 μm diameter (Interfacial Dynamics Corp.). supplied at a concentration of 4% solids. and 0.24 μm diameter PMMA spheres (NASA Space Science Lab. MSFC. AL) at a concentration of roughly 20% solids. The stock solutions were centrifuged down. resuspended in the appropriate carrier buffer (see below). and sonicated using a Branson 1200 sonicator (Branson Ultrasonics Corp.. Danbury, CT). This procedure was
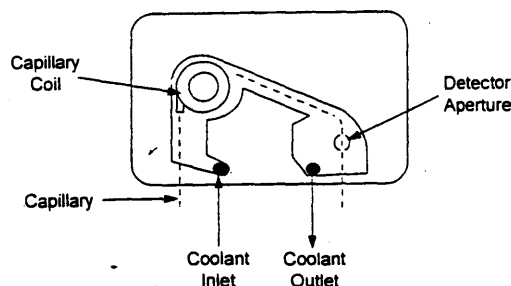

FIG. 3. Cartridge assembly.

repeated six to ten times to ensure that the spheres were equilibrated with the running buffer. The suspensions were diluted to a final volume fraction between 0.01 and 0.001 and allowed to sit overnight. The total volume of sample injected was between 1.63 and 9.02 nl. which means that the minimum number of particles ever introduced was around 10^5.

A stock solution of electrophoresis grade 100 mM borate buffer (Run buffer A. Beckman Instruments. Inc.. Fullerton. CA) was diluted with Milli-Q water to 0.2 and 2 mM. Except for the trials with the 0.83 μm PS spheres. the diluted borate buffer was used as the carrier buffer in the experiments and also to wash and resuspend the samples. The 2 mM borate buffer had a conductivity of 29 $\pm$ 1 μS/cm and a pH of 8.6 $\pm$ 0.1 at 25°C. and the 0.2 mM borate buffer had a conductivity of 9 $\pm$ 1 μS/cm and a pH of 8.6 $\pm$ 0.1 at 25°C. The experiments on the 0.83 μm PS spheres were performed in the 100 mM stock buffer.

Capillary Preparation and Characterization

Fused-silica capillaries of lengths ranging from 27 to 400 cm and diameters ranging from 20 to 75 μm were used for a suite of measurements. The capillaries were obtained from several companies: 75 μm (Polymicro. Phoenix. AZ): 50 and 20 μm (J&W Scientific. Folsom. CA): and 25 μm (Supelco Inc.. Bellefonte. PA). Other experiments. involving the hydrophobic particles. were performed in capillaries whose interior surfaces were coated with hydrophilic material. A wax coated (50 μm diameter. 312 cm length: J&W Scientific) and a polyethylene glycol coated capillary (50 μm diameter. 97 cm length: SGE. Austin. TX) were employed.

All of the capillaries were supplied without windows for the UV detector (Figs. 1 and 3). To create windows in the fused-silica capillaries. the outer polymer shell that encases the capillary was burned off with a match. 7 cm from the end of the capillary. For the coated capillaries. hot sulfuric acid ($\approx$250°C) was used to remove the polymer exterior. so as not to damage the coating on the interior. To delineate the window boundaries. two pieces of tape were wrapped
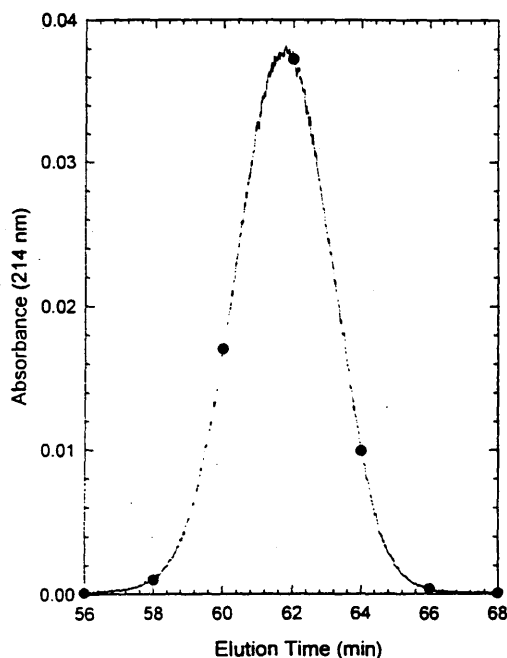

FIG. 2. A typical UV absorbance signal recorded during the Taylor–Aris dispersion experiments. This elution profile is for 0.19 μm PS spheres (2.0 mM borate buffer) in a 22.2 μm fused-silica capillary. The solid line is the experimental absorbance readings. and the solid dots represent points from the fit of a Gaussian profile.

around the capillary. The window was formed by dropping the acid on the capillary exterior exposed between the pieces of tape.

The fused-silica capillaries were initially conditioned by washing for 5 min with Milli-Q water, 10 min with 0.1 N NaOH, 5 min with Milli-Q water, and finally 10 min with carrier buffer. The coated capillaries were washed with Milli-Q water and buffer for 10 min each; to avoid damaging the coatings, no 0.1 N NaOH was used.

An important parameter to be established for interpreting the Taylor–Aris dispersion measurements is the capillary radius a. For the TMV experiments, the velocity of a tracer sample, mesityl oxide, was recorded at both high (approximately 20 psi) and low (approximately 0.5 psi) pressure drops. Using these data and the Hagen–Poiseuille equation, the radius of the capillary determined at the high and low pressures agreed to within 3%.

For the sphere experiments, an alternative method was developed. After the dispersion measurements were complete, the capillaries were cut into sections approximately 27 to 37 cm long. The capillary sections were placed in the P/ACE 2100 and filled with mercury.[2] A previously-weighed sample vial was placed in position to collect mercury as high pressure was applied to drive mercury through the capillary for a prescribed period of time (30 to 60 min). Voltage readings were recorded during the experiment from the side of the P/ACE 2100 with a portable digital multimeter. These readings were then converted into pressure readings using a linear relationship established by Beckman Instruments. After 0.5 to 1.0 ml of mercury was pushed through the capillary and the required time recorded, the mercury-filled outlet vial was weighed and the mass flow rate was determined. The Hagen–Poiseuille law was used to determine the radius of the capillary from the pressure drop and the volumetric flow rate of mercury. Using the mercury elution method, the capillary radii were measured 2 to 5 times, yielding results that varied by approximately 1.0%; the average of these measurements was taken as the capillary radius. To confirm that this method was sound, selected capillaries were examined using a scanning electron microscope (SEM). The average radius found using the mercury experiment agreed to within 2% of the SEM measured radius.

Photon Correlation Spectroscopy Measurements

A submicron particle analyzer (Coulter Electronics, Inc., Hialeah, FL) was used to independently determine the diffusion coefficients of the spheres in suspension. This instrument employs photon correlation spectroscopy to determine the average diffusion coefficient of the dispersed particles. These results were used as a benchmark for the diffusion

coefficients obtained from the Taylor–Aris dispersion measurements.

Capillary Hydrodynamic Fractionation Measurements

To gauge the extent to which the particle probability density function is uniform over the capillary cross-section, a variation of the dispersion experiments was performed. A small amount of mesityl oxide was introduced to the sample suspensions. This doped sample was electrokinetically injected into the capillary and a Taylor–Aris dispersion experiment performed as before. Any substantial difference between the average residence time of the mesityl oxide and the spheres was indicative that the radial distribution of the particles in the capillary was nonuniform (15–18).

Electroosmotic and Electrophoretic Mobility Measurements

The capillary electrophoresis system was used to measure electroosmotic and electrophoretic mobilities. The electroosmotic mobility of the capillary walls was measured by introducing a sample of buffer doped with a small amount of mesityl oxide. A known electric field was applied until the sample was driven down the capillary past the detector. The electroosmotic mobility was determined using the following equation:

$$M_{eo} = \frac{1}{E}\frac{L}{t_m},\qquad [1]$$

where E is the electric field strength, L is the distance from the point of the sample injection to the detector window, and t_m is the mean residence time of the mesityl oxide marker. To determine the electrophoretic mobility of the spheres, a sample of the spheres, doped with mesityl oxide, was injected, an electric field applied, and the electrophoretic mobility was calculated by

$$M = \frac{1}{E}\frac{L}{t_R} - M_{eo}.\qquad [2]$$

where t_R is the mean residence time of the particles. Samples containing only spheres were tested to verify that the sphere elution times and profiles were not modified by the addition of the mesityl oxide marker. The ζ-potential of the capillary walls was then determined by the use of the Smoluchowski equation, viz.

$$\zeta = \frac{\mu M}{\epsilon\epsilon_0},\qquad [3]$$

where μ is the viscosity of the sample, ϵ is the relative permittivity of water, and ϵ_0 is the permittivity of free space.

---

[2] Caution! Care should be taken to avoid coming in contact with the mercury or breathing mercury vapors.

A numerical algorithm for electrophoretic behavior in weak electrolytes was used to determine the ζ-potentials of the spheres (19).

Interpretation of Experimental Data

Certain conditions must be met to ensure that the classical Taylor–Aris theory may be applied. Two of the more significant requirements are as follows. First, the individual particles should have the opportunity to sample all of the radial positions in the capillary. Thus t_R, the mean residence time of the particles, needs to satisfy the following criteria:

$$\tau = \frac{D t_R}{a^2} > 10. \tag{4}$$

The details of this requirement are discussed elsewhere (11, 12).

Second, the sample particles should favor no radial position over any other. The Taylor–Aris theory, which treats the analyte as point particles, gives that $t_R = L/U$, where U is the mean velocity of the carrier fluid and L is the distance from the point of the sample injection to the detector window. That is, it follows from the theory that the mean axial velocity of the analyte will be that of the carrier fluid (12). This means that, in the experiments, particle–wall interactions and size-exclusion effects should be suppressed. So among other things, one requires that $a_p/a \ll 1$, where a_p is the radius of the particle. Also, buoyancy-driven motion and inertial effects should be negligible. So respectively,

$$\frac{L}{2nU} \ll \frac{a}{U_{\text{Stokes}}} \tag{5}$$

and

$$\frac{Ua}{\nu} \ll 1. \tag{6}$$

where n is the number of times the capillary is coiled in the cartridge assembly (Fig. 3) and

$$U_{\text{Stokes}} = \frac{2}{9} \frac{a_p^2}{\nu} \left(\frac{\rho_p}{\rho} - 1 \right) g \tag{7}$$

is the Stokes settling velocity of the particles. In Eq. [7], ρ_p is the density of the particle, and ρ and ν are the carrier fluid density and kinematic viscosity, respectively. Effects due to coiling of the capillary, i.e. the Dean effect, can be diminished by limiting the velocity to

$$\frac{a}{a_{\text{coil}}} \left(\frac{2Ua}{\nu} \right)^2 \left(\frac{\nu}{D} \right) \leq 20 \tag{8}$$

and $a/a_{\text{coil}} \leq 10^{-2}$. Here $(a/a_{\text{coil}})^{1/2}(2Ua/\nu)$ is the Dean number. ν/D is the Schmidt number, and a/a_{coil} is the capillary radius normalized to the radius of the coil (11). Finally, shear-induced migration is insignificant provided that (20–22)

$$\frac{\dot{\gamma} a^2 \phi^2}{2D} \ll 1. \tag{9}$$

where $\dot{\gamma}$ is the shear rate and ϕ is the volume fraction of particles.

With these stipulations in mind, one may extract the diffusion coefficient of the analyte from m_1 and m_2, the first and second moments of the UV detector signal (e.g. Fig. 2). As is well known (11),

$$D = \frac{a^2}{24 m_1} \left[\frac{(1 + 4m_2/m_1^2)^{1/2} + 3}{(1 + 4m_2/m_1^2)^{1/2} + 2m_2/m_1^2 - 1} \right]$$

$$\times \left[\frac{1}{2} + \frac{1}{2} (1 - \delta_a)^{1/2} \right]. \tag{10}$$

where

$$\delta_a = (768)^2 (2.1701 \cdots \times 10^{-5}) \chi_0 \tag{11}$$

and

$$\chi_0 = \frac{2m_2 - m_1^2 + (m_1^4 + 4m_1^2 m_2)^{1/2}}{8m_1^2 - 4m_2}. \tag{12}$$

Before the first and second moments can be used in Eqs. [10]–[12], corrections for the width of the injection sample zone and the detector aperture need to be applied; i.e.

$$m_1 = m_1^{\text{exp}} + \sum \delta_n m_1 \tag{13}$$

and

$$m_2 = m_2^{\text{exp}} + \sum \delta_n m_2. \tag{14}$$

The corrections needed for the injection zone are given by (11)

$$\delta_1 m_1 = -\frac{1}{2} \left(\frac{L}{U} \right) \left(\frac{V_{\text{inj}}}{\pi a^2 L} \right) \tag{15}$$

and

$$\delta_1 m_2 = -\frac{1}{12} \left(\frac{L}{U} \right)^2 \left(\frac{V_{\text{inj}}}{\pi a^2 L} \right)^2. \tag{16}$$

24   BELONGIA AND BAYGENTS

TABLE 1
Diffusion Coefficients and CHDF Data

Sample	D_0 (10⁻⁸ cm²/s)	Capillary Diameter (μm)	Coating	Borate buffer (mM)	D_{TA} (10⁻⁸ cm²/s)	$\delta_D{}^a$ (%)	Gaussian peaks (Y/N)	$\Delta t_R/\sigma$
TMV	4.0[b]	25.2		2.0	3.96 ± 0.26	−1.0	Y	
		27.2		2.0	3.96 ± 0.74	−1.0	Y	
0.19 μm PS latex spheres (hydrophilic)	2.61 ± 0.04	22.2		2.0	2.60 ± 0.26	−0.4	Y	
		25.3		2.0	2.56 ± 0.26	−1.9	Y	nil
		25.4		2.0	2.72 ± 0.24	4.2	Y	
		46.4		2.0	2.56 ± 0.08	−1.9	Y	
		75.7		2.0	2.74 ± 0.21	5.0	Y	
0.27 μm PS latex spheres (hydrophobic)	1.83 ± 0.04	74.3		0.2	1.91 ± 0.11	4.4	Y	0.34
		23.5		2.0	2.13 ± 0.19	16.4	Y	1.36
		22.2		2.0	2.32 ± 0.08	26.8	Y	1.77
		43.6	PEG	0.2	1.84 ± 0.13	0.6	Y	0.06
		47.1	wax	0.2	1.70 ± 0.07	−7.1	N	
0.24 μm PMMA spheres (hydrophobic)	2.06 ± 0.04	73.6		0.2	2.21 ± 0.11	7.3	Y	0.38
		23.5		2.0	0.84 ± 0.07	−59.2	N	0.80
		45.9	PEG	2.0	1.79 ± 0.08	−13.1	Y	0.85
0.83 μm PS latex spheres (hydrophilic)	0.59 ± 0.04	22.2		100.0	1.02 ± 0.05	72.9	Y	3.37

[a] $\delta_D = (D_{TA} - D_0)/D_0 \times 100$.
[b] The diffusion coefficient quoted by ATCC, the supplier of the TMV.

where V_{inj} is the volume of the sample (analyte) zone injected. The corrections for δL, the width of the detector aperture, are (11)

$$\delta_2 m_1 = -\frac{1}{2}\frac{L}{U}\left(\frac{\delta L}{L}\right)$$ [17]

and

$$\delta_2 m_2 = -\left(\frac{L}{U}\right)^2\left\{\chi_0\left(\frac{\delta L}{L}\right) + \frac{1}{12}\left(\frac{\delta L}{L}\right)^2\right\}.$$ [18]

Note the corrections for the aperture width are less significant than those for the sample zone and may be neglected for most systems.

RESULTS AND DISCUSSION

Diffusion Coefficients

The diffusion coefficients determined from the Taylor–Aris dispersion measurements (D_{TA}) are listed in Table 1. The benchmark values (D_0) for the TMV were provided by the supplier, and the benchmarks for the spheres were obtained from the photon correlation spectroscopy (PCS) measurements. The estimated error in the PCS measurements was ±(0.04 × 10⁻⁸) cm²/s. The radius of the spheres was determined using the Stokes–Einstein equation and the PCS diffusion coefficient measurements, viz.

$$a_p = \frac{kT}{6\pi D_0\mu}.$$ [19]

where k is Boltzmann's constant, T is the temperature, and μ is the viscosity of the solution. As was discussed previously, certain requirements need to be satisfied to ensure that the Taylor–Aris dispersion theory can be applied. The ranges of parameters and dimensionless groups pertinent to these requirements are listed in Table 2. For some of the experiments, $LU_{Stokes}/2n Ua$ was not small compared to unity and this will be discussed in the subsection on nonclassical effects on dispersion and the axial particle velocity.

The experimental results for the rod-shaped (300 nm × 18 nm) TMV are plotted in Figs. 4 and 5 as a function of dimensionless residence time τ. Figure 4 shows all of the experimental results, and Fig. 5 is the average of different experimental runs with similar values of τ. The TMV data show that as τ increases, the scatter in the data diminishes. Larger τ values reflect a more complete sampling by the particles of each radial position, which may increase the accuracy and reproducibility of the measured diffusion coefficients. The longer residence times may also help to attenuate any variability in the initial sample zone and in the imposition of the pressure gradient by the solenoid. The literature values available for the diffusion coefficient of the TMV varied from 2.60 × 10⁻⁸ to 5.00 × 10⁻⁸ cm²/s (23–26), with 4.40 × 10⁻⁸ cm²/s being the most recently quoted. This broad range of values can in part be explained on the basis that the data were obtained by different methods and

TABLE 2
Dimensionless Groups

Sample	$Ua/\nu \times 10^3$	$LU_{Stoke}/2nUa$	$De^2Sc \times 10^2$	$a/a_{col} \times 10^4$	$\dot{\gamma}a^2\phi^2/2D \times 10^5$
TMV[a]	4.3–8.3	6.4–7.7 × 10⁻⁵	2.5–12.5	6.1–6.6	0.51–0.98
0.19 μm PS latex spheres	2.5–17.5	0.01–0.13	1.2–150.0[c]	5.4–18.5	0.54–3.45
0.27 μm PS latex spheres	2.3–16.0	0.01–0.19	1.0–225.0	5.4–18.1	0.68–4.64
0.24 μm PMMA spheres	2.3–18.2	0.01–0.47	2.8–265.0	5.7–18.0	0.63–4.85
0.83 μm PS latex spheres	2.6–3.1	1.18–1.40	3.3–4.4	5.4	0.98–11.64

[a] The equivalent-sphere radius of TMV was estimated from the diffusion coefficient by using the Stokes–Einstein equation.

that different strains of the virus are of slightly different length and diameter. The value supplied by ATCC. 4.0 × 10^{-8} cm²/s. was used for D_0.

The experimental data for 0.19 μm diameter hydrophilic PS spheres are plotted against τ in Fig. 6. The experiments were run in five different fused-silica (uncoated) capillaries of different lengths and diameters to produce different τ. The results in all of the capillaries are in good agreement with the PCS diffusion coefficient. and the mean values for the diffusion coefficient are better at the larger τ values (Table 1).

The diffusivity of the 0.27 μm hydrophobic PS spheres was measured in both uncoated (fused-silica) and coated capillaries. These data are shown in Table 1 and Fig. 7. Clearly the results of the measurements in the 22 and 23 μm uncoated capillaries are unsatisfactory. These data are evidently biased by interactions of the particles with the capillary walls. as indicated by the capillary hydrodynamic fractionation experiments (see below). It is important to note that the UV elution profiles for these experiments were completely Gaussian. so without the benchmark provided by the PCS measurements. one would not necessarily suspect that these diffusion coefficients were in error. The results obtained in the 75 μm capillaries were more accurate. pre-
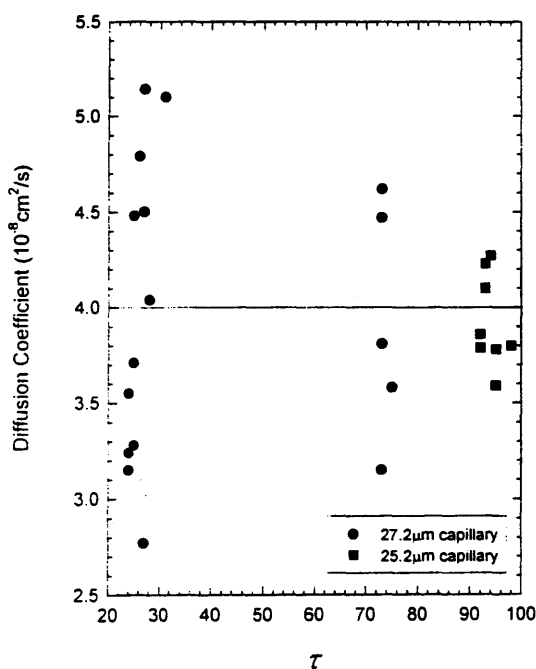

FIG. 4. Diffusion coefficient for TMV in 2 mM borate buffer measured by Taylor–Aris dispersion as a function of τ. Fused-silica capillaries with diameters of 27.2 and 25.2 μm were used to obtain these results. The solid line represents the diffusivity quoted by ATCC.

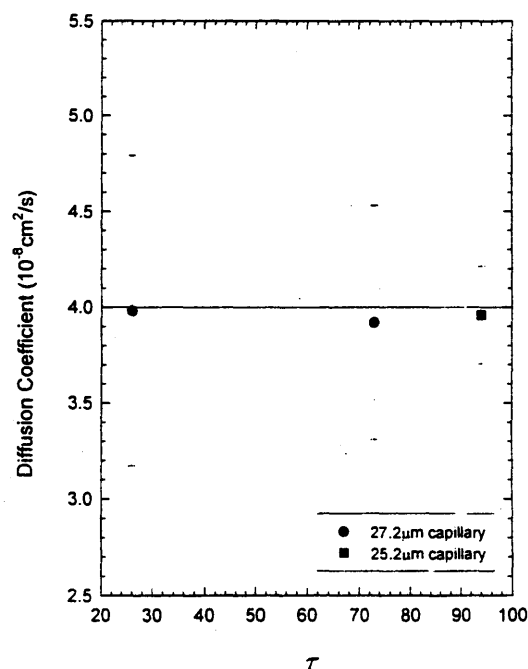FIG. 5. Diffusion coefficient of TMV obtained from Taylor–Aris experiments with similar τ. Error bars represent one standard deviation on either side of the mean (see Fig. 4 for raw data). The solid line represents the diffusivity quoted by ATCC.
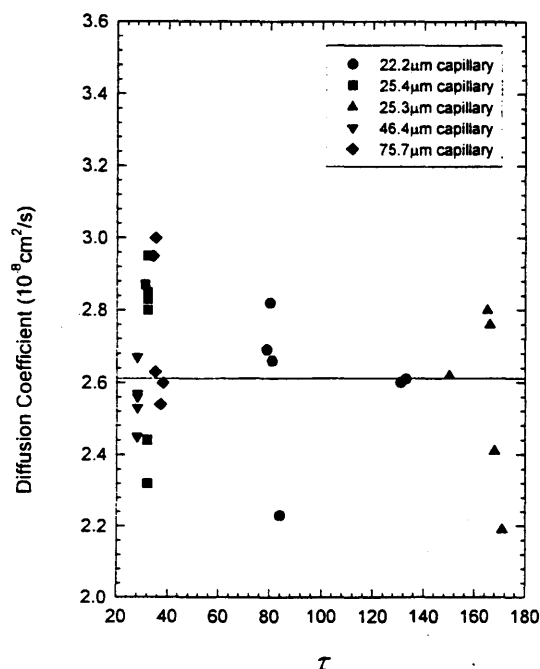
BELONGIA AND BAYGENTS

FIG. 6. Diffusion coefficient for 0.19 μm hydrophilic PS spheres in 2 mM borate buffer measured by Taylor–Aris dispersion as a function of τ. Fused-silica capillaries with diameters of 75.7, 46.4, 25.4, 25.3, and 22.2 μm were used in the experiments. The solid line is the diffusion coefficient obtained by photon correlation spectroscopy.

sumably because the cross-sectional area of the capillaries was an order of magnitude larger. Unfortunately, use of these large diameter capillaries created a need to use columns as long as 4 m to maintain $\tau > 10$, which in turn caused the time needed to perform the experiments to increase to approximately 5 h per trial. To suppress hydrophobic effects, capillaries with hydrophilic coatings were tried. The 43.6 μm PEG coated capillaries yielded excellent results despite the comparatively short residence times ($\tau = 12$, $t_R = 50$ min). The results quoted for the 47 μm wax coated capillary were obtained by fitting a Gaussian curve to the front half of the UV absorbance signal. In these capillaries, the elution profiles evinced a significant shoulder (Fig. 8) and, in the absence of any benchmark data, would presumably be discarded. It seems likely that some particle adsorption occurred on the wax coated capillary inasmuch as this capillary plugged after one (satisfactory) run with 0.24 μm PMMA spheres (see below and Fig. 9).

The data for the 0.27 μm PS spheres, especially those from the narrowest capillaries, point to the need for more substantive guidelines indicating when one might have confidence in the measurements. This point is reinforced by the results shown in Fig. 9 for the 0.24 μm PMMA spheres.

Once again the diffusion coefficients from the 23 μm uncoated capillaries were unsatisfactory. In this case the elution profiles were not Gaussian and exhibited trailing shoulders that suggest adsorptive/hydrophobic interactions with the walls. To diminish wall effects, the experiment was repeated in (nominally) 75 μm uncoated capillaries: Gaussian profiles and better results were obtained. Nevertheless, without a benchmark for comparison, one could not be confident of these data. Results of comparable accuracy were obtained in the PEG and wax coated capillaries (though the wax coated capillary subsequently plugged), and no particular advantage was gained by using them.

Though we performed no measurements of Hamaker constants, it would appear that, of the hydrophobic spheres, PMMA is more strongly attracted to the capillary walls. For example, PMMA plugged the wax coated capillary and, on the basis of non-Gaussian profiles, appeared to adsorb to the walls of the 23.5 μm fused-silica capillaries (Gaussian profiles were obtained in 73.6 μm fused-silica capillaries). The 0.27 μm PS spheres showed no evidence of adsorption to fused-silica capillaries, though some adsorption to the wax coating is believed to have occurred (the elution profiles exhibited trailing shoulders). When non-Gaussian behavior
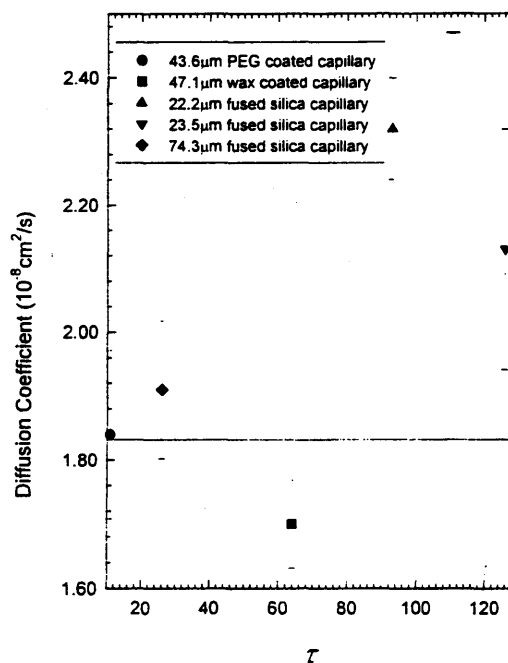
FIG. 7. Diffusion coefficient of 0.27 μm hydrophobic PS spheres obtained from Taylor–Aris experiments with similar τ. Experiments with $\tau = 93$ and 126 were done in 2.0 mM borate buffer, and the other experiments were performed in 0.2 mM borate buffer. The solid line represents the diffusion coefficient obtained by using photon correlation spectroscopy. The error bars represent one standard deviation on either side of the mean.
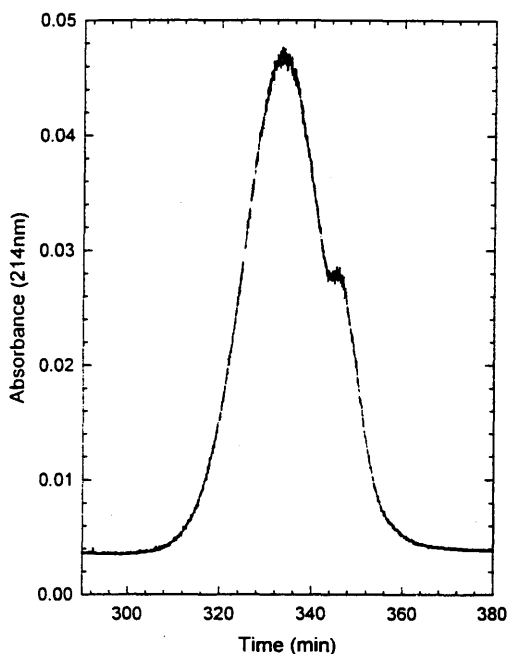
FIG. 8. Typical non-Gaussian elution profile: 0.27 μm PS spheres. 0.2 mM borate buffer. 47.1 μm wax coated capillary.

the elution profile (12). we investigated the utility of the mean particle residence time as a gauge for when the long-time dispersion data could be accurately interpreted with the classical theory. This was done by performing capillary hydrodynamic fractionation (CHDF) experiments as described in the experimental section. The dimensionless parameter of interest in the experiments is $\Delta t_R/\sigma$. where Δt_R is the difference between the mean residence times of the particles and the tracer solute. and σ is the standard deviation in the particle residence time.

The result of the study are summarized in Table 1: note that these data are for residence times well in excess of a^2/D. We have found that. when $\Delta t_R/\sigma$ approaches or exceeds unity, the particle elution profiles are not adequately interpreted with the classical theory. irrespective of how beautifully Gaussian these data may be. Figure 10 shows the result of a CHDF experiment on the 0.27 μm PS particles in 74.3 μm fused-silica capillaries. Here $\Delta t_R/\sigma$ is 0.34. and the Taylor–Aris dispersion measurements were within 4.5% of D_0 for these conditions. When fused-silica capillaries with one-third the diameter were used. $\Delta t_R/\sigma$ increased by about a factor of four. as did the error in the diffusivity measurement. Figure 11 shows a result of a CHDF experiment on the 0.83

was obtained. the leading edge of the elution profile was fit to a Gaussian distribution. and. in each case. the diffusion coefficient was underpredicted.

Finally. measurements were also attempted for hydrophilic 0.83 μm PS spheres (Table 1). The elution profiles obtained were Gaussian and reproducible ($\tau \approx 26$, $t_R \approx 90$ min). However. the diffusion coefficient derived from the profile differed from D_0 by 73%.

In their study on the use of Taylor–Aris dispersion to measure protein diffusion coefficients. Bello et al. (14) found that the shape of the elution profile (i.e. Gaussian vs non-Gaussian) was a reasonable indicator for when their dispersion data would yield accurate values for the protein diffusivities. For the colloidal systems investigated here. it seems clear that the shape of the elution profile does not suffice as the sole determinant of when the Taylor–Aris theory can be used to interpret the dispersion data.

Capillary Hydrodynamic Fractionation

As previously noted. the classical theory of Taylor–Aris dispersion gives that t_R. the mean residence time of the particles. will be the same as that of the fluid in which they are immersed for $t_R \gg D/a^2$. This result holds. provided factors that would bias the radial particle distribution in the capillary (e.g. size-exclusion effects) are negligible. Since such factors do not necessarily alter the Gaussian form of

FIG. 9. Diffusion coefficient of 0.24 μm hydrophobic PMMA spheres in 0.2 mM borate buffer obtained from Taylor–Aris experiments with similar τ. The solid line represents the diffusion coefficient obtained by photon correlation spectroscopy. The error bars represent one standard deviation on either side of the mean. Only one experiment was performed in the wax coated capillary because the capillary plugged on the second run.
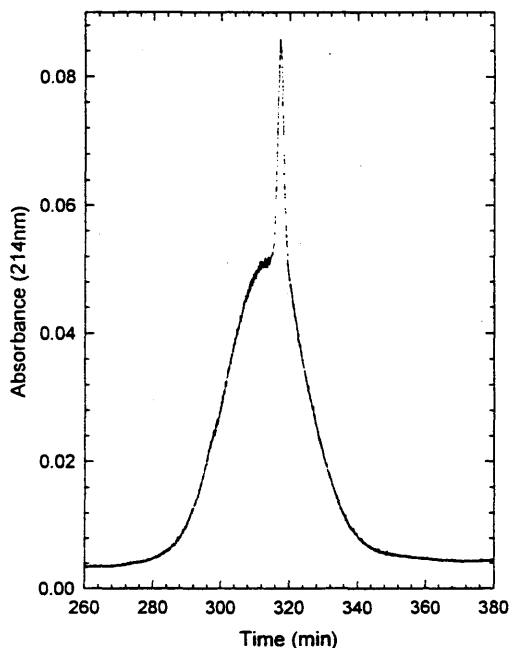
FIG. 10. Typical absorbance profile recorded during a capillary hydro-dynamic fractionation experiment when fractionation is insignificant. $\Delta t_R/\sigma \approx 0.34$. 0.27 μm PS spheres. 0.2 mM borate buffer, 74.3 μm fused-silica capillary.

μm PS particles in a 22.2 μm fused-silica capillary. For these circumstances. the Taylor–Aris profiles were quite Gaussian. but the CHDF measurements yield $\Delta t_R/\sigma = 3.4$. As a result. the diffusivity extracted from the dispersion data is in error.

As a final illustration that $\Delta t_R/\sigma$ is a useful long-time metric. consider the measurements performed in the PEG coated capillaries with the hydrophobic spheres. For the 0.27 μm PS spheres. $\Delta t_R/\sigma$ is small compared to unity, and the resulting diffusion coefficient agrees with D_0. For the 0.24 μm PMMA spheres. $\Delta t_R/\sigma$ is near unity and the error in the diffusivity is -13.1%.

Nonclassical Effects on Dispersion and Axial Particle Velocity

To determine if colloidal and hydrodynamic forces sub-stantially modify the dispersion of the sample (27–30), the dispersion data were corrected for their effects. A numerical algorithm based on the method of Silebi and DosRamos (27) was used to calculate the ratio $D*/D_{TA}^*$ where

$$D_{TA}^* = D_0 + \frac{a^2 U^2}{48 D_0} \qquad [20]$$

and where $D*$ is the dispersion corrected for equilibrium double layer. van der Waals, size-exclusion. wall resistance. and inertial effects. The algorithm was tested on cases ana-lyzed by Silebi and DosRamos (27) and was found to be in agreement with their results.

Hamaker constants as well as the zeta potentials of the capillary walls and particles were required as input for the calculation of $D*/D_{TA}^*$. A range of Hamaker constants found in the literature (31) for the interaction between quartz and PS/PMMA in water were considered for the uncoated capil-laries; the Hamaker constant for the PEG coated capillary was estimated using a range of values typical of polymers. Electrokinetic measurements were performed as described in the Materials and Methods. and their results are listed in Table 3.

The results of the calculations of $D*/D_{TA}^*$. and the cor-rected diffusion coefficients. are shown in Table 4 for those experiments in which Gaussian curves were recorded and $\Delta t_R/\sigma$ exceeded 0.1 (cf. Table 1). In uncoated. fused-silica capillaries the corrected diffusion coefficients were in better agreement with D_0 (as measured by PCS). Interpretation of the data in the PEG coated capillary was not improved. but it should be noted that interaction with the PEG coating may not be adequately represented by the simple model used
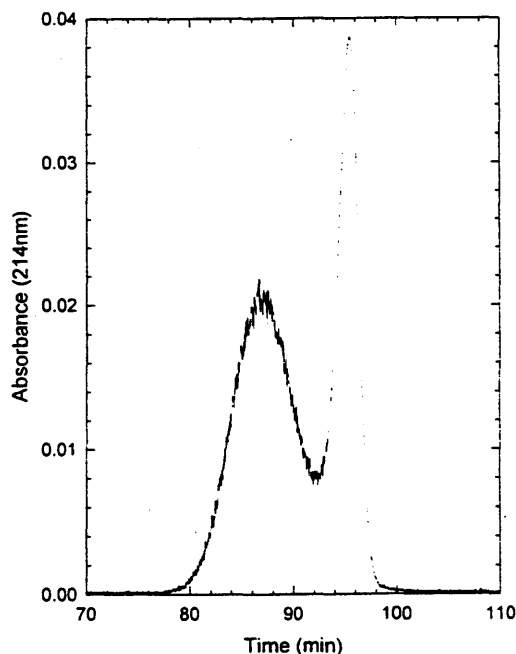

FIG. 11. Typical absorbance profile recorded during a capillary hydro-dynamic fractionation experiment when fractionation becomes important. $\Delta t_R/\sigma \approx 3.4$. 0.83 μm PS spheres. 100 mM borate buffer. 22.2 μm fused-silica capillary.

TABLE 3

Electrokinetic Data

Capillary	Borate buffer (mM)	Electroosmotic mobility (10^{-4} cm²/V s)	Zeta potential (mV)
Fused silica	100.0	0.68	-87.12
	2.0	1.11	-142.21
	0.2	1.18	-151.18
PEG coated	2.0	0.26	-33.31
	0.2	0.54	-69.18
Wax coated	0.2	1.17	-149.89

Particles	Borate buffer (mM)	Electrophoretic mobility (10^{-4} cm²/V s)	Zeta potentia (mV)
0.19 um PS	2.0	-4.11	-76.31
0.27 μm PS	2.0	-4.76	-89.83
	0.2	-4.14	-120.79
0.24 μm PMMA	2.0	-4.41	-80.15
	0.2	-3.68	-84.81
0.83 μm PS	100.0	-3.37	-43.67

here. In all cases. the adjustments were small. as one might expect from extant theory (12, 27–30) and the modest fluid velocities (ca. 100 μm/s) employed in the experiments. For the 0.27 μm PS and 0.24 μm PMMA spheres in (nominally) 75 μm capillaries. the agreement between the corrected D_{TA} and D_0 was excellent. The discrepancy between the corrected D_{TA} and D_0 remained significant for the 0.27 and 0.83 μm PS spheres in the (nominally) 20 to 25 μm capillaries.

In calculating D^*/D^*_{TA}. effects due to gravitational settling of the particles (29, 32) were neglected. Owing to the design of the capillary cartridge (Fig. 3). the particles experience a time–periodic body force transverse (and parallel) to the capillary axis as they flow around the capillary

coil. For the 20 to 25 μm capillaries in Table 4. the capillary is coiled 4 to 8 times in the cartridge assembly: for 75 μm capillaries. n = 35 to 40. The half-period of the forcing is roughly $L/2nU$. and the characteristic settling time of the particles is a/U_{Settle}. As can be seen in Table 4. agreement between the corrected D_{TA} and D_0 is poor when $LU_{Settle}/2nUa$ is greater than about 0.1. This suggests that buoyancy-driven motion of the particles may have a significant influence on their dispersion. For plane Poiseuille flow between parallel plates. Shapiro and Brenner (32) have analyzed transverse periodic forcing of Brownian particles. and Prieve (29) has analyzed steady transverse gravitational forces combined with classical DLVO wall interactions. Neither analysis applies directly to the experimental arrangement used here. However. qualitatively these analyses show that the effect of the buoyancy forces will be to diminish the convective contribution to axial dispersion relative to that for the classical case. Certainly. if buoyancy effects are significant in our system. then omitting them from the interpretation of the elution profiles will result in an overestimation of the diffusion coefficient. and this is what is seen with the uncoated capillaries in Table 4.

CONCLUSIONS

Taylor–Aris dispersion has been shown to yield accurate measures of the diffusion coefficient for colloidal particles as large as 0.27 μm in diameter. The technique worked well for both spherical and rod-shaped (TMV) particulates. for which the orientationally-averaged translational diffusion coefficient was obtained. Because the principles of the measurement are straightforward. the method will work for even larger particles. but the measurement times become quite long as the particle size moves beyond 0.1 μm. To some extent the measurement time can be controlled by using

TABLE 4

Colloidal and Hydrodynamic Corrections

Sample	Capillary diameter (μm)	$\Delta r_e/\sigma$	A_H (10^{-1*} J)	D^*/D^*_{TA}	Corrected D_{TA} (10^{-*} cm²/s)	δ_D (%)	δ_* (%)	$LU_{Settle}/2nUa$
0.27 um PS (hydrophobic)	74.3	0.34	3.67–32.2	0.961–0.962	1.84 ± 0.11	0.4	0.0	0.02
	23.5	1.36	3.67–32.2	0.950–0.964	(2.02–2.05) ≈ 0.19	10.6–12.2	1.3	0.13–0.14
	22.2	1.77	3.67–32.2	0.947–0.962	(2.20–2.23) ≈ 0.08	20.1–22.0	-0.5	0.15–0.16
0.24 μm PMMA (hydrophobic)	73.6	0.38	3.44	0.961	2.12 ± 0.11	3.1	0.1	0.05
	45.9*	0.85	3.44–7.26*	0.975–0.976	1.75 ± 0.08	-15.3	-2.7	0.08–0.09
0.83 um PS (hydrophilic)	22.2	3.37	3.67	0.973	0.99 ± 0.05	68.2	-5.9	1.18–1.40

$^-\delta_t$ = $(U_r^{**} - U_r^{**})/U_r^{**}$ × 100.

* PEG coated capillary.

· The Hamaker constant for PEG coating was estimated using a range of values reported for polymers (31).

smaller capillaries, but care must be taken to suppress interactions between the particle and the capillary walls if one wishes to interpret the dispersion data with classical Taylor–Aris theory. The classical theory has been generalized to account for many effects (12), and the data here suggest that DLVO interactions and time-periodic buoyancy forces—either acting separately or in concert—are a significant cause of the departure from the stipulations on the classical theory. Thus to use a generalized theory of the dispersion, one would have to measure the ζ-potential of the particles and the capillaries, as well as the particle densities and size—in which case, given the Stokes–Einstein relation, the rationale for doing the dispersion measurement is all but lost.

In closing we should like to make two points. First, with precise control of the pressure drop across the capillary, one can avoid doing Hg flow rate measurements to determine the capillary radius, as well as separate capillary hydrodynamic fractionation measurements to assess the uniformity of the particle distribution over the capillary cross-section. Our pressure control was sufficient to perform the dispersion measurements, but the stabilization time of the solenoid made accurate determination of the pressure drop vs flow rate tedious (hence we tried this approach but once, for the TMV). A superior method of applying the pressure difference would make it possible to determine the capillary radius by simply measuring the residence time of a conservative solute tracer. Similarly, knowing the capillary radius and the pressure drop, one also knows the mean residence time of the fluid in the capillary. The mean residence time of the particles (i.e. the first moment of the UV absorbance) could then be used to determine whether a bias existed in the radial particle distribution.

Second, the ultimate utility of dispersion measurements in capillaries may prove to be as a technique to study colloidal and gravitational interactions rather than as a tool to measure diffusion coefficients. For example, the mean residence time of particles in capillaries has been used to investigate the role of colloidal forces in hydrodynamic chromatography and to study electrokinetic lift (18, 20–22). The dispersion of the particle velocities about this mean should also be of interest from practical and fundamental perspectives. To illustrate this point, the mean axial particle velocity is plotted in Fig. 12 versus the mean velocity of the carrier buffer for the systems summarized in Table 4. Two obvious features of the figure are that the particle and fluid velocity are nearly equal, and there is remarkable agreement between the data and the calculated result based on the model of Silebi and DosRamos (27). The percent relative error in the calculation, averaged over a set of experiments, is given in Table 4 as $\delta_U \equiv (U_p^{calc} - U_p^{expt})/U_p^{expt} \times 100$, where U_p^{calc} and U_p^{expt} respectively denote the calculated and measured particle velocity. It is clear from the table and the figure that, whatever combination of colloidal and gravitational
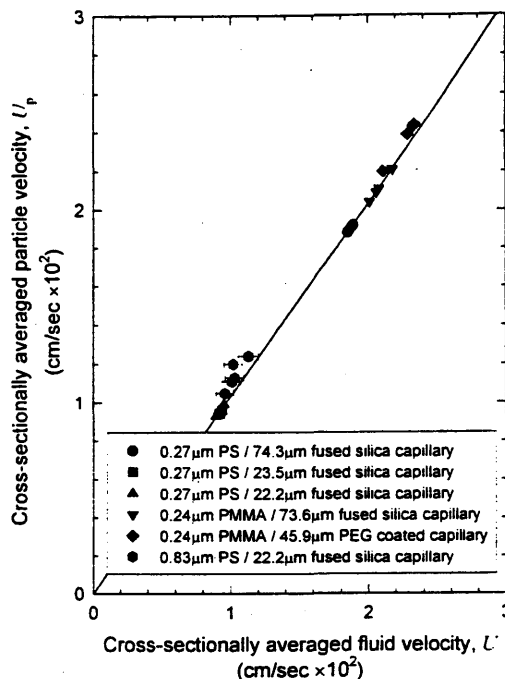

FIG. 12. Measured particle velocities vs the cross-sectionally averaged fluid velocity. The solid line represents the predicted average particle velocity for a given cross-sectionally averaged fluid velocity using the method of Silebi and DosRamos (27).

interactions is involved, their effect on U_p is quite weak compared to their influence on the particle dispersion. U_p hardly differs from U and, owing to the low fluid velocity, the line for U_p^{calc} in Fig. 12 is essentially insensitive to the buffer ionic strength and to the particle and capillary ζ-potentials (cf. Table 3 for the range of electrokinetic parameters used in the determination of U_p^{calc}). U_p would also appear to be insensitive to those factors omitted from the Silebi and DosRamos model (e.g. time-periodic transverse forcing of the particle motion). Conversely, the measured dispersivity can be substantially altered from D_{TA}^* and the influence of the colloidal and/or gravitational effects on the dispersion is readily detected.

ACKNOWLEDGMENT

REFERENCES

1. Stilbs, P., *Prog. NMR Spectrosc.* **19**, 1 (1987).
2. Dunlop, P. J., Harris, K. R., and Young, D. J., in "Determination of

Thermodynamic Properties'' (B. W. Rossiter and R. C. Baetzold, Eds.), Physical Methods of Chemistry, Vol. 6, p. 236, John Wiley & Sons, Inc., New York, 1992.

3. Comper, W. D., and Preston, B. N., in ''Analytical Ultracentrifugation in Biochemistry and Polymer Science'' (S. E. Harding, A. J. Rowe, and J. C. Horton), p. 428. The Royal Society of Chemistry, England, 1992.

4. Dunlop, P. J., Harris, K. R., and Young, D. J., in ''Determination of Thermodynamic Properties'' (B. W. Rossiter and R. C. Baetzold, Eds.), Physical Methods of Chemistry, Vol. 6, p. 228, John Wiley & Sons, Inc., New York, 1992.

5. Harding, S. E., in ''Microscopy, Optical Spectroscopy, and Macroscopic Techniques'' (C. Jones, B. Mulloy, and A. H. Thomas, Eds.), Methods in Molecular Biology, Vol. 22, p. 97, Humana Press, Clifton, NJ, 1994.

6. Taylor, G., Proc. R. Soc. A219, 186 (1953).

7. Taylor, G., Proc. R. Soc. A225, 473 (1954).

8. Aris, R., Proc. R. Soc. A235, 67 (1956).

9. Loh, W., Tonegutti, C. A., and Volpe, P. L. O., J. Chem. Soc., Faraday Trans. 89(1), 113 (1993).

10. Castillo, R. C., Dominguez, H. C., and Costas, M., J. Phys. Chem. 94, 8731 (1990).

11. Alizadeh, A., Nieto de Castro, C. A., and Wakeham, W. A., Int. J. Phys. 1, 243 (1980).

12. Brenner, H., and Edwards, D. A., ''Macrotransport Processes.'' Butterworth-Heinemann, Boston, 1993.

13. ''Handbook of Capillary Electrophoresis'' (J. P. Landers, Ed.). CRC Press, Ann Arbor, MI, 1994.

14. Bello, M. S., Rezzonico, R., and Righetti, P. G., Science 266, 773 (1994).

15. DosRamos, J. G., and Silebi, C. A., J. Colloid Interface Sci. 133(2), 302 (1989).

16. Prieve, D. C., and Hoysan, P. M., J. Colloid Interface Sci. 64(2), 201 (1978).

17. Miller, C. M., Sudol, E. D., Silebi, C. A., and El-Aasser, M. S., J. Colloid Interface Sci. 172, 249 (1995).

18. Hollingsworth, A. D., and Silebi, C. A., Langmuir 12, 613 (1996).

19. Baygents, J. C., and Saville, D. A., J. Colloid Interface Sci. 146, 9 (1991).

20. Leighton, D., and Acrivos, A., J. Fluid Mech. 177, 109 (1987).

21. Leighton, D., and Acrivos, A., J. Fluid Mech. 181, 415 (1987).

22. Acrivos, A., Batchelor, G. K., Hinch, E. J., Koch, D. L., and Mauri, R., J. Fluid Mech. 240, 651 (1992).

23. Nave, R., Weber, K., and Potschka, M., J. Chromatogr. A 654, 229 (1993).

24. Lauffer, M. A., J. Am. Chem. Soc. 66, 1188 (1944).

25. Watanabe, I., and Kawade, Y., J. Chem. Soc. Jpn. Bull. 26, 294 (1953).

26. Brune, D., and Kim, S., Proc. Natl. Acad. Sci. U.S.A. 90, 3835 (1993).

27. Silebi, C. A., and DosRamos, J., AIChE J. 35, 1351 (1989).

28. Brenner, H., and Gaydos, L. J., J. Colloid Interface Sci. 58, 312 (1977).

29. Prieve, D. C., Sep. Sci. Technol. 17, 1587 (1982).

30. DiMarzio, E. A., and Guttman, C. M., Macromolecules 3, 131 (1970).

31. Visser, J., Adv. Colloid Interface Sci. 3, 331 (1972).

32. Shapiro, M., and Brenner, H., Phys. Fluids A 2(10), 1744 (1990).

APPENDIX D: Capillary Electrophoresis Measurements of Electrophoretic Mobility for Colloidal Particles of Biological Interest

This manuscript has been published *Applied and Environmental Microbiology*, (64(7), 2572–2577, 1998) and is reproduced here with kind permission from American Society for Microbiology.

Vol. 64, No. 7

Capillary Electrophoresis Measurements of Electrophoretic Mobility for Colloidal Particles of Biological Interest

J. R. GLYNN, JR., B. M. BELONGIA, R. G. ARNOLD, K. L. OGDEN,
AND J. C. BAYGENTS*

*Department of Chemical and Environmental Engineering,
The University of Arizona, Tucson, Arizona 85721*

The electrophoretic mobilities of three bacterial strains were investigated by capillary electrophoresis (CE) and were compared with results obtained by microelectrophoresis (ME). The CE measurements yielded bimodal electropherograms for two of the strains, thus illustrating for the first time that surface charge variations within a monoclonal population can be probed by CE. Intrapopulation variations were not detected by ME. The mobilities of three chemically distinct types of latex microspheres were also measured. Differences between the mean mobilities obtained by CE and ME were not statistically significant ($P \leq 0.50$); the standard deviations of the CE measurements were typically 2 to 10 times smaller than those obtained by comparable ME measurements. The reproducibility of CE permitted batch-to-batch mobility variations to be probed for the bacteria (one of the strains exhibited such variations), and aggregation was evident in one of the latex suspensions. These effects were not measurable with ME.

Over the past decade. capillary electrophoresis (CE) has been developed into a standard technique in biotechnology. CE is used for analytical separation of charged solutes, such as carbohydrates, proteins, DNA, pharmaceuticals. herbicides. and pesticides. as well as lower-molecular-weight ions (1, 19. 27). CE is a powerful clinical diagnostic tool for profiling. screening. and detecting drugs. carbohydrates. lipids. enzymes. proteins. and nucleic acids (46). Variants of CE. known as micellar electrokinetic capillary chromatography (27) and capillary electrochromatography (36). allow solutions of nonionic analytes to be resolved.

Recently. CE has been applied to suspensions involving particles of biological interest. including viruses (19). bacteria (9. 19). silica sols (31). and polystyrene nanospheres (45). An advantage of electrophoretic separation compared with filtration or centrifugation is that electrophoresis is characteristically gentle and suitable for labile compounds and microorganisms. For example. Ebersole and McCormick (9) found that more than 90% of the bacteria that they tested remained viable after CE. and other workers (13. 35) have obtained similar viability results for cells separated dielectrophoretically in electric fields having comparable strengths (ca. 100 V/cm).

While the capabilities of CE to separate compounds and particles are well-established (for reviews see references 2. 26. and 27). the method has not been widely used to measure electrophoretic mobilities. Accurate measurements of electrophoretic mobilities are important in many biological and environmental sciences and technologies, ranging from clinical diagnostics (40. 41) to biocolloid adhesion (8. 10. 12, 17, 33, 39. 43. 44). Tobacco mosaic virus (6. 15) and polymer latex mobilities (6. 15. 23) have been characterized by CE. but Zhu and Chen (47) found that for human erythrocytes. the electrophoretic mobility measured by CE differed by 21% from previously published values. As there have been no direct comparisons between CE and other techniques. we determined

electrophoretic mobilities by CE and by microelectrophoresis (ME), and we report the results obtained here. Our objectives were essentially to examine whether CE could be used to measure the electrophoretic mobility of larger particles (diameter, ca. 1 μm) of biological interest and to assess the accuracy of the CE method compared with ME (8, 29, 42). We present results for the electrophoretic mobilities of three strains of bacteria and three chemically distinct microspheres (used in biocompatibility determinations) at two pHs and three ionic strengths. The method that we used was based on the work done with tobacco mosaic virus by Grossman and Soane (15). Differences between CE and ME mobility measurements were not statistically significant, and the CE data typically showed lower variances than the ME data. In addition, it was possible by using CE to detect electrophoretic heterogeneities in two of the bacterial species, as well as aggregation in one of the latex suspensions. To our knowledge. this was the first use of CE to resolve mobility variations within a monoclonal population.

MATERIALS AND METHODS

Bacterial strains and preparation. The bacterial strains investigated in this study were A1264, a gram-negative, motile, ellipsoidal bacterium (ratio of length to width, 2.5) that was isolated from the Savannah River deep subsurface environment, and two strains isolated from the Department of Energy site at Oyster. Va. The Oyster groundwater isolates were CD1 (a gram-negative, nonmotile, ellipsoidal bacterium with a ratio of length to width of 1.5) and PL2W31 (a gram-positive, nonmotile, ellipsoidal bacterium with a ratio of length to width of 2.5). The equivalent spherical radii of the bacteria used, based on their projected areas, were all approximately 0.5 μm. Cultures were grown to the early stationary phase (absorbance at 600 nm, approximately 1.5) in 250-ml Erlenmeyer flasks containing 100 ml of 10% PTYG (0.25 g of peptone per liter, 0.25 g of tryptone per liter, 0.50 g of yeast extract per liter, 0.6 g of MgSO₄ · 7H₂O per liter, 0.07 g of CaCl₂ · 2H₂O per liter) at room temperature (22 to 24°C) with constant agitation (150 rpm). The cells were separated by centrifugation (20 min, 10⁴ × g) and resuspended in 100 ml of filter-sterilized 3-(N-morpholino)propanesulfonic acid (MOPS) buffer containing 4.186 g of MOPS (Sigma; titrated to pH 7.02 with 1 N NaOH; conductivity, 760 μS/cm; ionic strength, 10 mM) per liter. The washing procedure was repeated to produce each final suspension (concentration, 10⁹ to 10¹⁰ cells/ml), which was then incubated at room temperature for 18 h. (The bacterial species and stage of growth were predicated on the results of a related bacterial attachment study (3); the CE technique which we describe is robust and adaptable to species at all stages of growth.) At that point, cell density was measured by acridine orange direct counting (20). Throughout the process, culture purity was repeatedly verified by direct visual observation (approximately 10⁴ cells were observed). plating, and comparisons of colony mor-

* Corresponding author. Mailing address: Department of Chemical and Environmental Engineering, The University of Arizona. Tucson, AZ 85721. Phone: (520) 621-6043. Fax: (520) 621-6048. E-mail: jcb@maxwell.che.arizona.edu.

Sample Zone

Data Acquisition

UV Detector

Capillary Inlet

Capillary Outlet

Buffer Reservoir for Anode

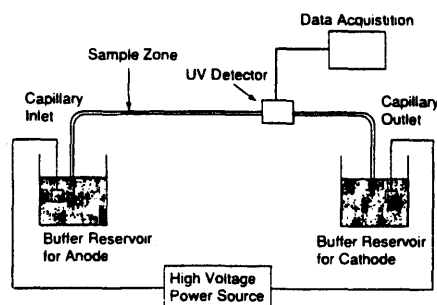Buffer Reservoir for Cathode

High Voltage Power Source

FIG. 1. Schematic diagram of the CE apparatus.

phology. Direct visual observation was also used to confirm that the cells were monodisperse at the time of the experiments.

CE measurements were performed with at least three separate batches of each microorganism. The batches were grown and prepared for measurement on different days. Typically, three to five mobility measurements were obtained for a given batch, although in some instances, as few as one or two measurements were obtained. ME measurements were obtained with cells from a single culture.

Microspheres and preparation. The following three types of microspheres were studied: 0.6-μm-diameter, surfactant-free, hydrophobic amidine polystyrene latex microspheres (Interfacial Dynamics Corp., Portland, Oreg.); 0.22-μm-diameter, surfactant-free, hydrophilic carboxylate-modified polystyrene latex (CML) microspheres (Interfacial Dynamics Corp.); and 0.2+-μm-diameter, hydrophobic polymethyl methacrylate (PMMA) microspheres (NASA Space Science Lab. Marshall Space Flight Center, Huntsville, Ala.). The hydrophobicities reported below are the hydrophobicities under the test conditions used in this study. The polystyrene and PMMA spheres were supplied at stock concentrations equivalent to roughly 4 and 20% solids, respectively. The stock solutions were centrifuged for 4 to 16 min, depending on the size of the microspheres, resuspended in the appropriate carrier buffers, and sonicated for at least 10 min to produce monodisperse suspensions. The carrier buffers used were 100 mM borate (Beckman borate buffer kit; pH 8.39; conductivity, 1.60 mS/cm) and 2 mM borate (pH 8.35; conductivity, 41.3 μS/cm). The 2 mM borate buffer was produced by diluting a 100 mM buffer solution with ultrapure water (Ultra-Pure Water Research Group, Department of Chemical and Environmental Engineering. The University of Arizona). The buffers were filter sterilized. The washing procedure was repeated three times for the CML and amidine particles and 6 to 10 times for the PMMA particles since the PMMA stock solutions contained residual impurities from the emulsion polymerization process. The suspensions were diluted to final volume fractions of 0.01 to 0.001 and stored overnight at 4°C to ensure that the spheres were in equilibrium with the carrier buffers. The amidine and CML particle measurements were made in the 2 and 100 mM borate buffers. The PMMA measurements were made in the 2 mM borate buffer. Prior to measurements, the suspensions were inspected for aggregation with a light microscope.

CE measurements. A Beckman P/ACE System 2100 capillary zone electrophoresis unit, controlled by Beckman System Gold software, was used to measure electrophoretic mobilities. A schematic diagram of the instrument is shown in Fig. 1. Application of an electric field down the axis of the capillary drove particle transport by the following two mechanisms: electrophoresis (translation due to the particles' native charge) and electroosmosis (bulk convection of the carrier electrolyte in which the particles were immersed). M. the electrophoretic mobility of a particle population (or subpopulation), follows from the translation rate compared with the translation rate of a neutral dopant, which moves from the inlet past the UV detector at the electroosmotic velocity of the buffer (21, 28): M = (L_tot L_d/V) (1/t_p · 1/t_ref). where L_d is the distance from the inlet reservoir to the detector, V is the voltage difference applied across the length of the capillary (L_tot), and t_ref and t_p are the mean migration times of the reference marker and the particle population (or subpopulation), respectively (27).

The capillaries used were obtained from Polymicro Technologies (Phoenix, Ariz.) and were flexible fused silica capillaries (inside diameter, 75 μm) that were not coated on the inside and had an exterior polyimide coating. The capillaries connected the anode (inlet) reservoirs to the cathode (outlet) reservoirs (Fig. 1) and were typically 57 cm long (distance from the cathode reservoir to the detector, 50 cm). A detector window was created by burning off the polyimide coating 7 cm from the outlet; the detector cell volume was O(10^−12 m^3). Prior to each use, the capillaries were conditioned by using the Beckman capillary replacement procedure (a 10-min high-pressure rinse with Beckman capillary regenerator solution A, 5 min of H_2O, 10 min of buffer).

The optimum detector wavelength was determined for each sample suspension by measuring the absorbance of a capillary filled with the suspension over the range of possible wavelengths after a baseline was established for the background

buffer. The optimum detector wavelength for all of the measurements was 214 nm. For the bacteria, the lower detection limit corresponded to an injected bacterial concentration of approximately 10^6 cells/ml (data not shown) or 2,500 cells (for an injected volume of 25 nl). For the microspheres, the detection limit was 10^10 particles/ml.

Actual measurements were preceded by a prerinse with buffer (5 min for bacteria and 2 min for latex microspheres). Samples were introduced into the capillary with a 2- to 10-s standard high-pressure (20-lb/in^2) injection. The injection time was a function of the sample absorbance. Typically, a 5-s injection was used, and for a 57-cm-long capillary with an inside diameter of 75 μm the sample volume injected was approximately 25 nl. CD1 was also injected electrokinetically by using a 175-V/cm applied electric field for 10 s to introduce the sample into the capillary. Heating effects were avoided by maintaining the capillary at 25°C during the measurements and by performing an Ohm's law test (32) to establish the operating conditions for which there was a linear relationship between the applied electric field and the current within the capillary. The applied electric fields used ranged from 88 to 426 V/cm.

A neutral dopant, mesityl oxide (15, 28), was added to each sample (2 μl of mesityl oxide in 400 μl of suspension) to determine the electroosmotic velocity. Measurements were determined for the sample with and without the marker to verify that addition of the marker did not affect colloid migration. Electrokinetic measurements were also determined for the background buffer and (for bacterial samples) a bacterial filtrate, which was obtained by passing the bacterial suspension through a 0.2-μm-pore-size Acrodisc sterile filter. The measurements were determined at least three times per sample.

A series of high-pressure rinses (5 min with 0.1 N HCl, 5 min with H_2O, 5 min with Beckman capillary regenerator solution A, and 5 min with H_2O for bacteria; 5 min with Beckman capillary regenerator solution A and 5 min with H_2O for latex spheres) were used between successive measurements. The contents of the cathode and anode buffer reservoirs were replaced after three measurements to minimize the effect of electrode reactions on buffer composition (4). At the end of each period of experimentation, the capillary was prepared for storage by repeating the rinse procedure twice (for a total of three rinses). This standard rinse procedure was followed by successive 10-min high-pressure rinses with methanol and air, and then the capillary was stored dry.

ME measurements. ME electrophoretic mobilities were measured with a Lazer Zee model 501 meter (PenKem, Inc., Bedford Hills, N.Y.). Measurements were made as recommended in the user's manual, at room temperature. The model 501 meter did not have a thermostat and reported the data as a ζ potential, which could be converted to electrophoretic mobility by using the Smoluchowski equation (37): M = (εε_0/μ)ζ, where μ is the buffer viscosity, ε is the relative permittivity of the buffer, and ε_0 is the permittivity of a vacuum (8.854 × 10^−12 C^2/N · m^2). The parameter values internal to the model 501 meter were reference values for water at 20°C. Measurements were repeated at least 10 times for each particle.

RESULTS

Bacteria. Capillary electropherograms for the carrier buffer and the bacterial filtrate exhibited no electrophoretic peaks. The strength of the electroosmotic flow (EOF) was 7.13 ± 0.55 μm · cm/V · s (n = 36). The marker did not affect the magnitude or distribution of the electrophoretic mobilities for the bacteria. Preliminary experiments showed that the results were also independent of the injection technique employed.

Electropherograms of A1264 and CD1 exhibited two electrophoretic peaks. as shown in Fig. 2. Neither A1264 nor CD1 exhibited significant batch-to-batch variation in their electrophoretic mobility modes, but some variation was observed in the fractions of the populations associated with these modes (Table 1). Note that the mode mobilities, M_1 and M_2, varied little from batch to batch, and there was little variation in M_{avg}, the area-weighted average of M_1 and M_2. Similar results were obtained for A1264 (data not shown).

The third bacterium tested, PL2W31, exhibited only one electrophoretic peak (Fig. 2) and batch-to-batch variation in mobility. The mobilities of the batches were −0.51 ± 0.04 μm · cm/V · s (n = 5), −0.45 ± 0.04 μm · cm/V · s (n = 2), and −0.41 ± 0.02 μm · cm/V · s (n = 3).

The CE and ME results are compared in Table 2. Differences in the mobilities obtained with the two techniques are shown in Table 2. The CE data for A1264 and CD1 are reported as the mode mobilities and relative peak areas, averaged over all of the measurements; the standard deviations shown are the mean standard deviations for the batches. No
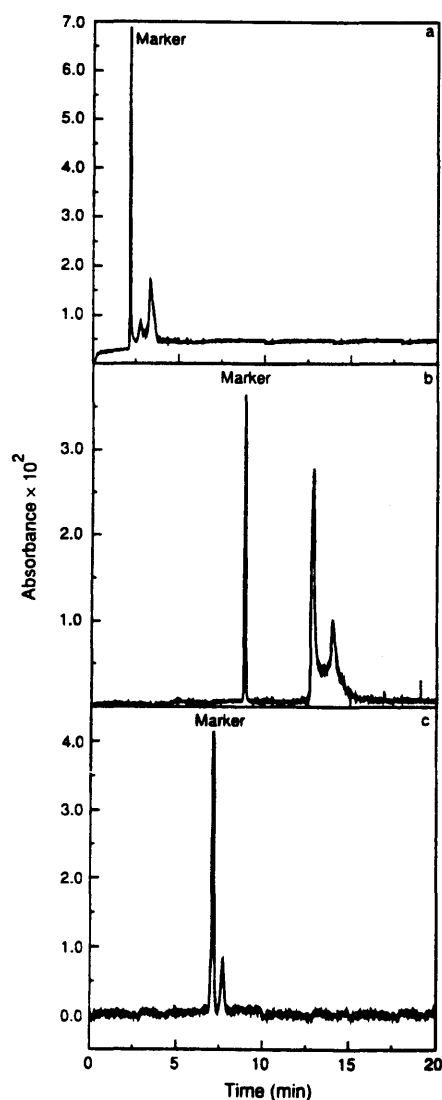
FIG. 2. Typical electropherograms for bacterial cells. Measurements were obtained in 10 mM MOPS buffer with an injection interval of 5 s. Unless indicated otherwise, an electric field of 175 V/cm was applied over a 57-cm column. (a) Neutral marker peak (2.2 min) and two bacterial peaks (2.8 and 3.3 min) for strain A1264. An electric field of 426 V/cm was applied over a 47-cm column. (b) Neutral marker peak (8.9 min) and two bacterial peaks (12.5 and 13.6 min) for CD1. The column length was 77 cm. (c) Neutral marker peak (7.1 min) and a single bacterial peak (7.7 min) for PL2W31.

bimodal distribution was detected by ME for A1264 and CD1. Since batch-to-batch variability was evident with PL2W31, comparisons between the measurement techniques were based on results from a single culture of this microorganism. CE and ME measurements were not obtained with cells from the same culture for A1264 and CD1, as these organisms showed no significant batch-to-batch variability in M_{avg} (Table 1).

Microspheres. Light microscopy of the microspheres revealed monodisperse suspensions except for the PMMA

particles, which exhibited significant aggregation. No electrophoretic peaks were observed with the baseline. The strength of the EOF was 10.77 ± 0.17 μm · cm/V · s ($n = 9$) in 2 mM borate buffer and 6.60 ± 0.18 μm · cm/V · s ($n = 8$) in 100 mM borate buffer. The marker had no effect on the magnitude or distribution of the electrophoretic mobilities for the latex spheres. Typical electropherograms for amidine and CML particles are shown in Fig. 3. The results of the CE and ME experiments are summarized in Table 2.

CE measurements obtained with the heterogeneous PMMA suspension revealed a bimodal distribution in mobility (Fig. 4; Table 2). Aggregates of microspheres were apparent when the suspension was inspected by light microscopy. After sonication for 1 h. the PMMA aggregates were disrupted (i.e., the suspension was monodisperse. as determined by light microscopy). CE measurements obtained for the monodisperse suspension yielded one electrophoretic peak (Fig. 4). Additional CE measurements were determined after time intervals ranging from 0 to 2.5 h to test for reaggregation of the microspheres. Time-dependent aggregation was apparent as determined by both visual inspection (light microscopy) and the redevelopment of a bimodal distribution in the electrophoretic mobility data (Fig. 4).

DISCUSSION

The general agreement between the data obtained with the CE and ME mobility measurement techniques is indicated in Fig. 5. Statistical differences in the mean electrophoretic mobilities determined by CE and ME were investigated by using a paired t test ($P = 0.40$) (7), a sign test ($P = 0.50$), and a Wilcoxon signed rank test ($P = 0.47$) (14); differences between the means were insignificant. Systematic differences associated with the choice of colloid, pH, or ionic strength were not observed.

The finding that CE results agree with ME results is not surprising. Electrokinetic theory shows that, as long as the particle size is no more than a few percent of the capillary diameter. the influence of hydrodynamic interactions on mobility measurements is negligible (25). Colloidal (e.g., van der Waals) and/or hydrophobic interactions between the analyte and the capillary wall can also bias mobility measurements. Such interactions are well-documented for proteins and other organic analytes (18, 24, 30), which tend to adsorb to quartz capillaries. Similar effects have been observed for 0.2-μm-diameter hydrophobic polystyrene and PMMA particles in capillaries with inside diameters of 25 μm (6). Analyte-wall interactions can be diminished by using capillaries with larger cross-sectional areas (5, 6), by modifying the carrier buffer, or by using coated capillaries (34). Coatings that reduce wall interactions. however. often reduce EOF and increase analysis time.

Based on similar numbers of replicate measurements, the standard deviations for CE results were typically much lower than the standard deviations for ME measurements (Table 2). This was probably because a single CE mobility measurement

TABLE 1. Batch-to-batch variation in CD1 electropherograms

Batch	No. of measurements	M_1 (μm · cm/V · s)[a]	M_2 (μm · cm/V · s)[a]	% of total area as peak 1	M_{avg} (μm · cm/V · s)[b]
1	5	-2.29 ± 0.11	-2.60 ± 0.12	31.8 ± 10.8	-2.51 ± 0.11
2	3	-2.27 ± 0.09	-2.52 ± 0.13	47.7 ± 10.7	-2.40 ± 0.10
3	5	-2.27 ± 0.05	-2.71 ± 0.12	61.2 ± 7.4	-2.44 ± 0.07

[a] M_1 and M_2 are the mobilities for the first and second modes in the electropherogram. respectively.

[b] M_{avg} is the area-weighted average of M_1 and M_2.

TABLE 2. Comparison of electrophoretic mobilities as determined by CE and ME

Sample	M_1 (μm · cm/V · s)[a]	M_2 (μm · cm/V · s)[a]	% of total area as peak 1	M_{CE} (μm · cm/V · s)[b]	M_{ME} (μm · cm/V · s)[c]	$M_{CE} - M_{ME}$ (μm · cm/V · s)
Bacteria						
A1264[d]	−1.48 ± 0.05 (7)[e]	−2.31 ± 0.10 (7)	28.9 ± 3.6 (7)	−2.07 ± 0.07 (7)[f,g]	−1.95 ± 0.65 (10)[h]	−0.12
CD1[d]	−2.25 ± 0.07 (18)	−2.62 ± 0.11 (18)	48.2 ± 8.6 (18)	−2.44 ± 0.08 (18)[f,g]	−2.24 ± 0.32 (10)[h]	−0.20
PL2W31[d]				−0.51 ± 0.04 (5)[h]	−0.78 ± 0.35 (10)[h]	0.27
Microspheres						
Amidine[i]				−1.79 ± 0.18 (3)	−1.98 ± 0.12 (10)	0.19
CML[i]				−3.42 ± 0.14 (3)	−2.95 ± 0.25 (10)	−0.47
PMMA[i]	−4.41 ± 0.08 (3)	−5.17 ± 0.11 (3)	78.8 ± 3.1 (3)	−4.57 ± 0.09 (3)[f]	−4.73 ± 0.39 (10)	0.16
Amidine[j]				−1.95 ± 0.17 (3)	−1.78 ± 0.21 (10)	−0.17
CML[j]				−3.69 ± 0.06 (3)	−3.82 ± 0.20 (10)	0.13

[a] M_1 and M_2 are the mobilities for the first and second modes in the electropherogram, respectively.
[b] M_{CE} is the electrophoretic mobility as determined by CE.
[c] M_{ME} is the electrophoretic mobility as determined by ME.
[d] Measurements were determined in 10 mM MOPS buffer, pH 7.02.
[e] The numbers in parentheses are the numbers of times that measurements were determined.
[f] M_{CE} is the weighted average of M_1 and M_2.
[g] Mobility was determined by measuring multiple cultures of bacteria.
[h] Mobility was determined by measuring a single culture of bacteria.
[i] Measurements were determined in 2 mM borate buffer, pH 8.35.
[j] Measurements were determined in 100 mM borate buffer, pH 8.39.

was based on (i) analysis of a relatively large number of particles (approximately 10^4 particles) and (ii) the time required for the analyte to move distances on the order of 0.1 m in an electric field stronger than 100 V/cm. By contrast, ME and related measurement techniques (22) detect particle translation over short distances (typically less than 100 μm) in weak fields (10 V/cm or less) and often rely on observation of far fewer particles.

Two of the bacteria used, A1264 and CD1, and one of the microsphere types used, PMMA, exhibited multimodal behavior during CE measurements. Similar distributions were not obtained with ME. CE is a sensitive analytical separation technique tailored to resolve mixtures of charged solutes on the basis of their electrophoretic mobilities. The sensitivity stems from the strength of the applied field and the uniformity of the particle velocities over the capillary cross section. Thus, when a large number of particles is sampled, an electrophoretic histogram and a more detailed picture are obtained.

The results of related studies on bacterial sorption (3) suggest that the bimodal electrophoretic mobilities of the CD1 and A1264 populations were due to intrapopulation heterogeneities in surface charge rather than aggregation, contamination, or artifactual peak splitting. Bimodal mobilities of cells have been observed in other contexts, and in these cases the bimodality has been attributed to variations in surface structure (the presence or absence of appendages or capsular material) (8) and surface antigens (38). Ebersole and McCormick (9) found that differences in chain morphology can cause multimodal behavior in bacterial electrophoretic mobility. Visual inspection confirmed that the cells used here were monodisperse. Spread plating revealed no major contaminant. The detection limit for bacteria was approximately 2,500 cells or roughly 1/10th the standard number of cells injected. The presence of a significant contaminant (observable with CE as a separate peak) should have been recognized by direct visual observation or by differences in colony morphology following growth on solid media. The multiple peaks were in no way due to the carrier buffer, cell exudates, or mesityl oxide. Ermakov et al. (11) concluded (based on both theory and experiments) that artifactual peak splitting is avoided by buffering solutions at least 1 pH unit from the particle isoelectric point. Since bacterial isoelectric points are generally in the range from 2 to 4, depending on species and growth stage (16), and since the

pH of the MOPS buffer was 7.02, artifactual peak splitting is an unlikely source of multimodal mobilities observed.

The PMMA microspheres also exhibited an electrophoretic mobility distribution. Direct visual observation revealed both
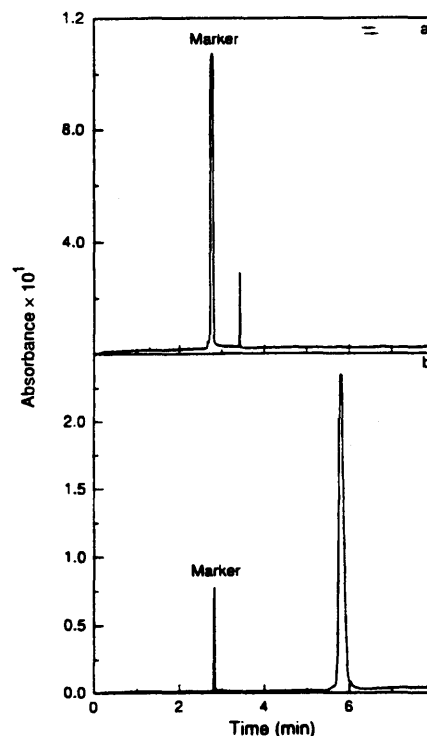

FIG. 3. Typical microsphere electropherograms. Measurements were obtained in 100 mM borate buffer with an applied electric field of 350 V/cm over a 57-cm column. (a) Neutral marker peak (2.8 min) and a microsphere peak (3.5 min) for the amidine polystyrene microspheres. The injection interval was 10 s. (b) Neutral marker peak (2.8 min) and a microsphere peak (5.8 min) for the CML microspheres. The injection interval was 1 s.
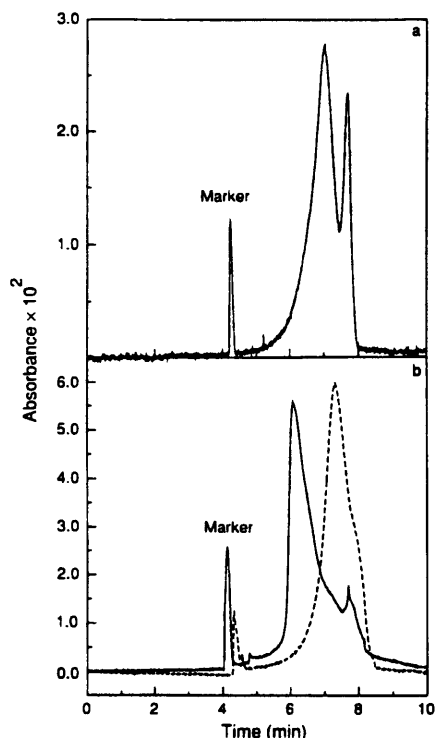
FIG. 4. Electropherograms for the PMMA suspension. Measurements were obtained in 2 mM borate buffer with an applied electric field of 175 V/cm over a 57-cm column. The injection interval was 5 s. (a) Neutral marker peak (4.2 min) and two microsphere peaks (7.0 and 7.7 min) for the polydisperse PMMA particles (prior to sonication). (b) Evolution of bimodal electrophoretic mobility in PMMA suspensions. Electropherograms based on suspensions were obtained immediately after sonication (dashed line) and 2.5 h after sonication (solid line).

individual particles and aggregated clumps in suspensions used for the original CE and ME measurements. Sonication subsequently produced a monodisperse suspension of PMMA microspheres that yielded a single peak in the corresponding electropherograms. Subsequent CE measurements obtained with the same suspension revealed the time-dependent evolution of a second peak. Within 2.5 h, the suspension was comprised of mainly aggregated particles, as indicated by visual inspection. Over the same period the area of the peak containing the monodisperse microspheres decreased, while the second peak grew. presumably due to aggregation.

Despite the noticeable difference in the areas under the peaks in their respective electropherograms, the numbers of amidine and CML (Fig. 3) particles injected were actually similar. A likely explanation for this phenomenon is the differences in the specific absorbances of the particles, as the area of an electrophoretic peak is a function of both the number of particles injected and the specific absorbance of the particles. Since both colloid volume fractions (less than 0.01 for both microorganisms and microspheres) and UV absorbance (typically less than 0.1 absorbance unit) were low, detection artifacts associated with high particle concentrations are unlikely.

In the CE measurements, electroosmotic flow was characterized by doping the samples with a neutral marker, mesityl oxide. EOF measurements were reproducible for all of the

carrier buffers tested. The standard deviation of the EOF in 10 mM MOPS buffer (pH 7.02) was roughly three times the standard deviation of the values obtained at both ionic strengths in the borate buffer (pH 8.35). This probably was due to the neutral pH of MOPS solutions, since electroosmosis in uncoated capillaries is extremely sensitive to pH changes in the range from pH 4 to 8 (27).

CD1 samples were injected both electrokinetically and by high pressure. Electrokinetic injections have been known to bias samples (27), since analytes with lower (more negative) electrophoretic mobilities tend to remain in the sample vial. No difference in either the distribution or the magnitude of the electrophoretic mobilities exhibited by CD1 was observed in response to the change in injection technique (data not shown).

CD1 exhibited multimodal behavior in electrophoretic mobility at relatively low field strengths (175 V/cm). Higher applied electric fields were required for A1264 because at low field strengths, microbial motility distorted the CE peaks. Attempts to uncover multimodal electrophoretic behavior in bacterial strain PL2W31 by increasing the applied electric field to approximately 350 V/cm were unsuccessful.

The reproducibility of the CE data allowed batch-to-batch variations to be studied in the bacteria. A1264 and CD1 showed variations in the distributions of their populations between the respective mobility modes. although this had only a minor effect on the average mobilities of the populations. PL2W31 exhibited batch-to-batch variability in its (unimodal) mean electrophoretic mobility. Investigators should be able to use CE to help assess the influence of such variability on biophysical processes (e.g., attachment to surfaces) or, alternatively, to help evaluate connections between variations in surface charge density and outer membrane structure and composition.

In summary, CE measurements of electrophoretic mobility were not distinguishable from measurements of electrophoretic mobility obtained by ME. Based on similar numbers of replicate measurements, the standard deviations for CE results were typically much lower than the standard deviations for ME measurements. Distributed mobilities, which were readily observed with CE for two bacterial species and one of the polymer latices, could not be detected with ME.
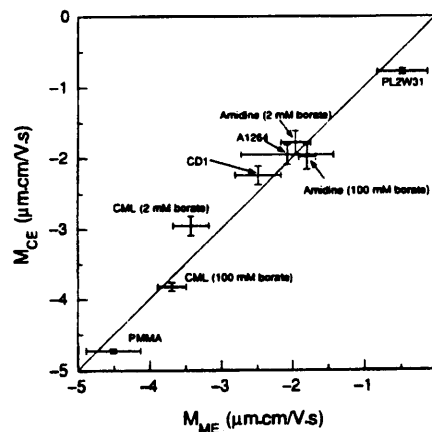

FIG. 5. Comparison of the electrophoretic mobilities determined by CE (M_{CE}) and ME (M_{ME}). The error bars are 2 standard deviations wide. The diagonal is a 1:1 line representing complete data agreement. The data are labeled according to sample type.

REFERENCES

1. **Altira, K. D.** 1996. Additional application areas of capillary electrophoresis. Methods Mol. Biol. **52:**309–344.
2. **Baker, D. R.** 1995. Capillary electrophoresis. John Wiley and Sons, New York, N.Y.
3. **Baygents, J. C., J. R. Glynn, Jr., O. Albinger, B. K. Biesemeyer, K. L. Ogden, and R. G. Arnold.** Variation of surface charge density in monoclonal bacterial populations: implications for transport through porous media. Environ. Sci. Technol., in press.
4. **Bello, M. S.** 1996. Electrolytic modification of a buffer during capillary electrophoresis. J. Chromatogr. **744:**81–91.
5. **Bello, M. S., R. Rezzonico, and P. G. Righetti.** 1994. Use of Taylor-Aris dispersion for measurement of a solute diffusion coefficient in thin capillaries. Science **266:**773–776.
6. **Belongia, B. M., and J. C. Baygents.** 1997. Measurements on the diffusion coefficient of colloidal particles by Taylor-Aris dispersion. J. Colloid Interface Sci. **195:**19–31.
7. **Box, G. E. P., W. G. Hunter, and J. S. Hunter.** 1978. Statistics for experiments. John Wiley and Sons, New York, N.Y.
8. **Cowan, M. M., H. C. van der Mei, I. Stokroos, and H. J. Busscher.** 1992. Heterogeneity of surfaces of subgingival bacteria as detected by zeta potential measurements. J. Dent. Res. **71:**1803–1806.
9. **Ebersole, R. C., and R. M. McCormick.** 1993. Separation and isolation of viable bacteria by capillary zone electrophoresis. Bio/Technology **11:**1278–1282.
10. **Eisen, A., and G. Reid.** 1989. Effect of culture media on *Lactobacillus* hydrophobicity and electrophoretic mobility. Microb. Ecol. **17:**17–25.
11. **Ermakov, S. V., M. Y. Zhukov, L. Capelli, and P. G. Righetti.** 1994. Experimental and theoretical study of artificial peak splitting in capillary electrophoresis. Anal. Chem. **66:**4034–4042.
12. **Gannon, J., Y. Tan, P. Baveye, and M. Alexander.** 1991. Effect of sodium chloride on transport of bacteria in a saturated aquifer material. Appl. Environ. Microbiol. **57:**2497–2501.
13. **Gascoyne, P. R. C., X.-B. Wang, Y. Huang, and F. F. Becker.** 1997. Dielectrophoretic separation of cancer cells from blood. IEEE (Inst. Electr. Electron. Eng.) Trans. Ind. Appl. **33:**670–678.
14. **Gibbons, J. D.** 1971. Nonparametric statistical inference. McGraw-Hill Book Company, San Francisco, Calif.
15. **Grossman, P. D., and D. S. Soane.** 1990. Orientation effects on the electrophoretic mobility of rod-shaped molecules in free solution. Anal. Chem. **62:**1592–1596.
16. **Harden, V. P., and J. O. Harris.** 1953. The isoelectric point of bacterial cells. J. Bacteriol. **65:**198–202.
17. **Heckels, J. E., B. Blackett, J. S. Everson, and W. E. Ward.** 1976. The influence of surface charge on the attachment of *Neisseria gonorrhoeae* to human cells. J. Gen. Microbiol. **96:**359–364.
18. **Hjerten, S.** 1985. High-performance electrophoresis elimination of electroendosmosis and solute adsorption. J. Chromatogr. **347:**191–198.
19. **Hjerten, S., K. Elenbring, F. Kilár, J. Liao, A. J. C. Chen, C. J. Siebert, and M. Zhu.** 1987. Carrier-free zone electrophoresis, displacement electrophoresis and isoelectric focusing in a high-performance electrophoresis apparatus. J. Chromatogr. **403:**47–61.
20. **Hobbie, J. E., R. J. Daley, and S. Jasper.** 1977. Use of Nuclepore filters for counting bacteria by fluorescence microscopy. Appl. Environ. Microbiol. **33:**1225–1228.
21. **Hunter, R. J.** 1981. Zeta potential in colloid science. Academic Press, San Francisco, Calif.
22. **Hunter, R. J.** 1993. Introduction to modern colloid science. Oxford University Press, New York, N.Y.
23. **Jones, H. K., and N. E. Ballou.** 1990. Separations of chemically different particles by capillary electrophoresis. Anal. Chem. **62:**2484–2490.
24. **Jorgenson, J. W., and K. D. Lukacs.** 1983. Capillary electrophoresis. Science **222:**266–272.
25. **Keh, H. J., and J. L. Anderson.** 1985. Boundary effects on electrophoretic motion of colloidal spheres. J. Fluid Mech. **153:**417–439.
26. **Kuhn, R., and S. Hoffstetter-Kuhn.** 1993. Capillary electrophoresis: principles and practice. Springer-Verlag, New York, N.Y.
27. **Landers, J. P. (ed.)** 1994. Handbook of capillary electrophoresis. CRC Press, Ann Arbor, Mich.
28. **Lauer, H. H., and D. McManigill.** 1986. Capillary zone electrophoresis of proteins in untreated fused silica tubing. Anal. Chem. **58:**166–170.
29. **Lemp, J. F., Jr., E. D. Asbury, and E. O. Ridenour.** 1971. Electrophoresis of colloidal biological particles. Biotechnol. Bioeng. **8:**17–47.
30. **Liu, J., V. Dolnik, Y.-Z. Hiesh, and M. Novotny.** 1992. Experimental evaluation of the separation efficiency in capillary electrophoresis using open tubular and gel-filled columns. Anal. Chem. **64:**1328–1336.
31. **McCormick, R. M.** 1991. Characterization of silica sols using capillary zone electrophoresis. J. Liq, Chromatogr. **14:**939–952.
32. **Nelson, R. J., A. Paulus, A. S. Cohen, A. Guttman, and B. L. Krager.** 1989. Use of Peltier thermoelectric devices to control column temperature in high-performance capillary electrophoresis. J. Chromatogr. **480:**111–127.
33. **Olsson, J., P. O. Glantz, and B. Krasse.** 1976. Electrophoretic mobility of oral streptococci. Arch. Oral Biol. **21:**605–609.
34. **Palmieri, R., and J. A. Nolan.** 1994. Protein capillary electrophoresis: theoretical and experimental considerations for method development. p. 325–368. *In* J. P. Landers (ed.), Handbook of capillary electrophoresis. CRC Press, Ann Arbor, Mich.
35. **Pethig, R.** 1996. Dielectrophoresis: using inhomogeneous AC electric fields to separate and manipulate cells. Crit. Rev. Biotechnol. **16:**331–348.
36. **Ross, G., M. Dittman, F. Bek, and G. Rozing.** 1996. Capillary electrochromatography: enhancement of LC separation in packed capillary columns by means of electrically driven mobile phases. Am. Lab. (Fairfield Conn.) **28:**34–38.
37. **Russel, W. B., D. A. Saville, and W. R. Schowalter.** 1989. Colloidal dispersions. Cambridge University Press, New York, N.Y.
38. **Sabolovic, D., E. Knippel, U. Thomaneck, J. Rychly, and W. Shütt.** 1985. Electrophoretic mobility and monoclonal antibody combined in the study of human peripheral blood lymphocytes. p. 333–343. *In* W. Shütt and H. Klinkmann (ed.), Cell electrophoresis. Walter de Gruyter, Inc., New York, N.Y.
39. **Scholl, M. A., and R. W. Harvey.** 1992. Laboratory investigations on the role of sediment surface and groundwater chemistry in transport of bacteria through a contaminated sandy aquifer. Environ. Sci. Technol. **26:**1410–1417.
40. **Schütt, W., N. Hashimoto, and M. Shimizu.** 1994. Application of cell electrophoresis for clinical diagnosis. p. 255–280. *In* J. Bauer (ed.), Cell electrophoresis. CRC Press, Ann Arbor, Mich.
41. **Uhlenbruck, G., A. Fröml, R. Lütticken, and K. Hannig.** 1988. Cell electrophoresis of group B streptococci: separation of types Ia, Ib/c, III and IV before and after neuraminidase treatment. Zentralbl. Bakteriol. Parasitenkd. Infektionskr. Hyg. Abt. I Reihe A **270:**28–24.
42. **van der Mei, H. C., J. de Vries, and H. J. Busscher.** 1993. Hydrophobic and electrostatic cell surface properties of thermophilic dairy streptococci. Appl. Environ. Microbiol. **59:**4305–4312.
43. **van Loosdrecht, M. C. M., J. Lyklema, W. Norde, G. Schraa, and A. J. B. Zehnder.** 1987. Electrophoretic mobility and hydrophobicity as a measure to predict the initial steps of bacterial adhesion. Appl. Environ. Microbiol. **53:**1898–1901.
44. **van Loosdrecht, M. C. M., W. Norde, J. Lyklema, and A. J. B. Zehnder.** 1990. Hydrophobic and electrostatic parameters in bacterial adhesion. Aquat. Sci. **52:**103–114.
45. **VanOrman, B. B., and G. L. McIntire.** 1989. Analytical separation of polystyrene nanospheres by capillary electrophoresis. J. Microcolumn Sep. **1:**289–293.
46. **Xu, Y.** 1995. Capillary electrophoresis. Anal. Chem. **67:**463R–473R.
47. **Zhu, A., and Y. Chen.** 1989. High-voltage capillary zone electrophoresis of red blood cells. J. Chromatogr. **470:**251–260.